

Mass Microscopy:  
Imaging Biomolecules on Surfaces

ISBN: 90-393-4121-4

Mass Microscopy: Imaging Biomolecules on Surfaces

2005 © Stefan Luxembourg (s.luxembourg@hotmail.com)

A digital version of this thesis can be downloaded from: <http://www.amolf.nl>.

# Mass Microscopy: Imaging Biomolecules on Surfaces

Massamicroscopie van Biomoleculen op Oppervlakken  
(met een samenvatting in het Nederlands)

## **Proefschrift**

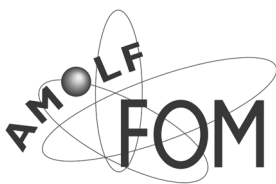
ter verkrijging van de graad van doctor  
aan de Universiteit Utrecht  
op gezag van de Rector Magnificus, Prof. dr. W. H. Gispen,  
ingevolge het besluit van het College voor Promoties  
in het openbaar te verdedigen  
op maandag 19 december 2005 des middags te 14:30 uur

door

Stefan Libertus Luxembourg

geboren op 5 maart 1976, te Leidschendam

promotor: Prof. dr. R. M. A. Heeren  
Faculty of Chemistry, Utrecht University  
FOM Institute for Atomic and Molecular Physics (AMOLF), Amsterdam



The work described in this thesis was performed at the FOM Institute for Atomic and Molecular Physics, Kruislaan 407, 1098 SJ Amsterdam, The Netherlands. This work is part of research program nr. 49 "Mass spectrometric imaging and structural analysis of biomacromolecules" of the "Stichting voor Fundamenteel Onderzoek der Materie (FOM)", which is financially supported by the "Nederlandse organisatie voor Wetenschappelijk Onderzoek" (NWO).

# Contents

---

<b>1. General Introduction</b>	<b>9</b>
1.1. Challenges for a macromolecular imaging technique	9
1.2. A brief history of imaging mass spectrometry	10
1.3. Scope of this thesis	11
<b>2. Macromolecular imaging mass spectrometry: fundamentals and techniques</b>	<b>13</b>
2.1. Ionization techniques for surface analysis	14
2.1.1. UV-MALDI	14
2.1.2. IR-MALDI	17
2.1.3. Secondary ion mass spectrometry	18
2.1.4. Strategies to improve molecular ion yields in SIMS	20
2.2. Chemical image generation in biomolecular imaging mass spectrometry	21
2.2.1. Microprobe mode imaging MS (general)	21
2.2.2. MALDI microprobe mode ion imaging	22
2.2.3. SIMS microprobe mode ion imaging	23
2.2.4. Microscope mode ion imaging	24
2.3. Experimental techniques	25
2.3.1. The TRIFT mass analyzer	25
2.3.2. MALDI microscope mode imaging	27
2.3.3. Kinetic energy distributions	29
<b>3. Rapid, high-spatial resolution mass spectrometric imaging of peptide and protein distributions on a surface</b>	<b>31</b>
3.1. Introduction	32
3.2. Experimental section	34
3.2.1. Instrument - MALDI source	34
3.2.2. Instrument – detection	35
3.2.3. Sample preparation	36
3.3. Results and discussion	37
3.4. Discussion: factors influencing microscope mode lateral resolution	44
3.5. Conclusions	47
<b>4. Infrared mass spectrometric imaging below the diffraction limit</b>	<b>49</b>
4.1. Introduction	50
4.2. Experimental section	51

## *Contents*

4.2.1. Instrumental	51
4.2.2. Sample preparation	51
4.3. Results and discussion	52
4.4. Conclusions	53
<b>5. The effect of local matrix crystal variations in matrix-assisted ionization techniques for mass spectrometry</b>	<b>55</b>
5.1. Introduction	56
5.2. Experimental section	58
5.2.1. Sample preparation	58
5.2.2. Mass spectrometry and imaging	59
5.3. Results and discussion	60
5.3.1. Phosphatidylcholine	60
5.3.2. Phosphatidylglycerol	64
5.3.3. Phosphatidylethanolamine	67
5.3.4. Phosphatidylinositol	69
5.4. Conclusions	70
<b>6. Fragmentation at and above surfaces in SIMS: effects of biomolecular yield enhancing surface modifications</b>	<b>73</b>
6.1. Introduction	74
6.2. Experimental section	76
6.2.1. Sample preparation	76
6.2.2. Mass spectrometry	77
6.2.3. Kinetic energy distributions	77
6.3. Decay rate constants: theoretical and experimental considerations	78
6.3.1. Unimolecular dissociation in the acceleration region	79
6.3.2. Unimolecular dissociation in the field free region	81
6.4. Results	82
6.4.1. Mass spectra	82
6.4.2. Ion yields	82
6.4.3. Kinetic energy distributions	83
6.4.3.1. Thin layer sample	83
6.4.3.2. ESD sample	84
6.4.3.3. Goldcoated sample	87
6.4.4. Decay rate constants, daughter ion formation and internal energies	88
6.4.4.1. Daughter ion formation in the acceleration region	88
6.4.4.2. Daughter ion formation in the field free drift region	91
6.5. Discussion and conclusions	92
<b>7. The molecular scanner in microscope mode</b>	<b>95</b>
7.1. Introduction	96
7.2. Experimental section	98

7.2.1 Sample preparation	98
7.2.2 (Imaging) Mass spectrometry	99
7.3 Results	100
7.3.1 Goldcoating prevents charge build-up in the sample	100
7.3.2. Sensitivity	101
7.3.3. Protein identification from a mixture	103
7.3.4. Microprobe and microscope mode imaging MS of molecular scanner samples	104
7.4. Discussion and conclusions	106
<b>Bibliography</b>	<b>109</b>
<b>Summary</b>	<b>117</b>
<b>Samenvatting</b>	<b>121</b>
<b>Nawoord</b>	<b>125</b>
<b>Curriculum Vitae</b>	<b>127</b>
<b>List of publications</b>	<b>128</b>





## General Introduction

### 1.1 Challenges for a macromolecular imaging technique

It is the intricate interplay between elements, individual molecules and molecular complexes that regulates life at cellular level. Functional biomolecules such as DNA, proteins, oligosaccharides, peptides, lipids, hormones and other small molecules constitute a dynamic molecular landscape, which characterizes the state of a biological system. In order to investigate the relation between this molecular organization and the functioning (or malfunctioning) of the system new, innovative approaches are required continuously. As a result, molecular biology has driven the development of modern molecular imaging techniques over the last decades. Many ill-understood health threats, like cancer and Alzheimer, alter the cellular biochemistry. For improved understanding of these and other diseases it is imperative to rapidly chart the molecular landscapes. Consequently, the biomedical sciences are investigating the differences between healthy and diseased states of organisms in a quest for biomarkers for specific diseases. In this respect especially the identity, distributions and modifications of proteins, which are involved in almost all life's processes, are of great interest. The localization of disease markers will not only lead to the fundamental understanding of a disease, but also serves diagnostic purposes and can identify potential drug target sites. Clearly, the desire to study the complexity of biological systems and their diseased states requires high lateral resolution, molecule specific imaging tools capable of charting distributions of a wide range of known and unknown molecules simultaneously.

Nowadays many imaging techniques are used to study biological systems at very high spatial resolution but they lack the chemical specificity (scanning electron microscopy, atomic force microscopy) or the chemical resolution (infrared microscopy) required to record the identity and the spatial distribution of the entities present in a sample simultaneously. Other imaging techniques can differentiate between a limited number of pre-selected analytes using fluorescent labels or antibodies (fluorescence microscopy, immunostaining), this requires detailed beforehand knowledge of the problem / system under study. Imaging mass spectrometry (MS) does encompass chemical specificity and lateral resolving power, and is capable of recording the spatial localization of many different constituents of a sample simultaneously. Its spatial resolving power is provided by spatial resolved ion generation or spatial resolved ion detection, its chemical specificity by analysis of a unique characteristic of a molecule: its mass.

## 1.2 A brief history of imaging mass spectrometry

It was only very recently that mass spectrometry was used to record distributions of large, intact biomolecules, e.g. proteins, directly from biological tissue for the first time. Ever since the first imaging mass spectrometry experiments in the 1960's using secondary ion mass spectrometry<sup>1, 2</sup> (SIMS) researchers have speculated about the possibilities of visualizing macromolecular distributions directly from organic samples with high lateral resolution. For a long time the ionization techniques available: SIMS and laser microprobe mass analysis (LAMMA) limited the information that could be obtained to distributions of elements and small organic fragments. It was only in the 1980's that the development of macromolecular ionization techniques, like matrix-assisted laser desorption/ionization (MALDI)<sup>3, 4</sup> made mass spectrometry of large biomolecules reality. With its capability to study high mass biomolecules, such as proteins and oligonucleotides, its sensitivity, chemical specificity and speed of acquisition, mass spectrometry revolutionized biochemical sciences and became the driving force behind the success of proteomics. In the mid-1990's several reports appeared on the MALDI analysis of peptides from whole cells.<sup>5, 6</sup> In continuation of this work Caprioli *et al.* performed the first MALDI imaging MS experiments in 1997.<sup>7</sup> In this study rat pituitary and pancreas tissue samples were prepared with a thin layer of matrix crystals on top, and moved through a 25  $\mu\text{m}$  UV laser spot to obtain protein signals from different positions on the tissue section. In comparison with the other imaging techniques mentioned before macromolecular imaging MS can record the distributions of many biomolecules present in the sample without having to label them in advance. Moreover the use of a molecule's mass to identify it, makes mass spectrometry also sensitive to post-translational modifications of proteins, which are important for the activation of protein functions like signal transduction and are also found to be important markers of diseases like cancer.

Although imaging mass spectrometry experiments have been performed for over 40 years biomolecular or macromolecular imaging mass spectrometry can be regarded as a relatively new field, which undergoes rapid developments. The ionization techniques, MALDI and SIMS have been most successful in biomolecular imaging MS applications. In order to develop imaging MS into a valuable tool for biological and pharmaceutical sciences it should be capable of recording distributions of a wide (mass) range of biomolecules at cellular or subcellular resolutions. There are several challenges, which have to be dealt with to come to this point, these include realization of:

- sufficient lateral resolution for imaging at cellular level
- rapid imaging methodologies
- identification of the detected species
- optimized sample preparation.

The potential of imaging MS to record the distributions of biomolecules in cells and tissue at cellular level as well as the improvements required were recognized by NWO, “Nederlandse Organisatie voor Wetenschappelijk Onderzoek”, who approved a major investment grant (NWO groot) for the development of a mass microscope in the year 2000. The mass microscope proposed would circumvent the spatial resolution limitations, reduce analysis times significantly and allow a greater versatility of ion sources for macromolecular imaging MS. In order to achieve this the mass microscope would have to utilize position correlated ion *detection* for image formation (stigmatic ion microscopy), instead of the commonly used position correlated ion *generation*, scanning microprobe methodology.

### 1.3 Scope of this thesis

In this thesis we deal with some of the challenges that were outlined in the previous section.

In **Chapter 2** a variety of aspects of imaging mass spectrometry, such as the most frequently used ionization methods, imaging strategies and its challenges are discussed. In addition details on the experimental set-ups and methodologies used are provided.

In **Chapter 3** UV-MALDI stigmatic ion microscopy is demonstrated for the first time. This true microscope mode ion imaging approach combines high lateral resolution with high speed of acquisition. The lateral resolution is determined on a test sample and the different factors affecting it are identified and discussed. The microscopic nature of this new methodology results in a gain of three orders of magnitude in speed of acquisition compared to the scanning microprobe approach.

The first ever high-resolution IR-MALDI mass spectrometric images are presented in **Chapter 4**. The results presented here, exemplify the greater versatility in choice of ion sources for macromolecular ion imaging when performed in microscope mode. The unique capabilities of microscope mode imaging are illustrated by a comparison of the achieved lateral resolution with the diffraction limited spot size of the 2.94  $\mu\text{m}$ -wavelength light in combination with the optical set up used to deliver the light to the sample in these experiments.

The work described in **Chapter 5** has served as a pilot study for later ME-SIMS studies on phospholipid distributions in biological systems. Here, we demonstrate that different classes of intact phospholipids can be detected using ME-SIMS. Mass spectrometric imaging of large matrix crystal samples reveals that segregation of analytes from these crystals complicates the interpretation of the spatial information obtained from any matrix-assisted chemical imaging technique.

In **Chapter 6** we use a set of substituted benzylpyridinium salts to study the effect of the reduction of internal energy of the ions generated in ME-SIMS as compared to SIMS. For this purpose, the fragmentation of the precursor ions is monitored at several instances in the mass spectrometer. Kinetic energy distributions are recorded and related to ion decay reactions. The results are explained within the framework of an existing model: the precursor model.

*Chapter 1*

In **Chapter 7** microscope mode MALDI imaging is combined with the molecular scanner methodology. In this approach high speed, high spatial resolution imaging MS is extended with improved sensitivity and identification possibilities for high mass proteins. Microscope and microprobe imaging modes of molecular scanner samples are demonstrated.

# Macromolecular imaging mass spectrometry: fundamentals and techniques

This chapter is divided in two parts. The first part, sections 2.1 and 2.2, introduces several important aspects of macromolecular imaging mass spectrometry. It serves to provide the reader with sufficient background knowledge of the field. Since SIMS and MALDI are used throughout this thesis as ionization techniques for imaging MS we focus on the description of some of the fundamentals of these two techniques. Other ionization techniques, which are sometimes used in imaging MS, like laser microprobe mass analysis (LAMMA), field desorption and the recently developed DESI (desorption electrospray ionization) are not discussed here. We point out the challenges in high speed, high lateral resolution macromolecular ion imaging, the concept of stigmatic ion microscopy and its benefits for imaging MS. Furthermore, we have tried to summarize the ongoing developments to improve the molecular ion yields in SIMS. The second part of the chapter includes a detailed description of the mass microscope set-up and of the experimental methodologies used, which will be useful as a reference for the later chapters.

## 2.1 Ionization techniques for surface analysis

### 2.1.1 UV-MALDI

The first MALDI analyses of macromolecules were performed in the mid-eighties of the past century. MALDI evolved from the modification of an existing technique: laser desorption ionization (LDI) or laser microprobe mass analysis (LAMMA)<sup>8</sup>. The idea for the intact desorption of macromolecules from an organic matrix was born in the lab of Prof. Franz Hillenkamp. The concept came about on the basis of an observation made during the LDI analysis of a sample containing both Alanine and Tryptophane using a 266 nm pulsed laser. While it was known that Alanine has a 10 times higher desorption threshold than Tryptophane at this wavelength, signals of both amino acids were observed at the threshold laser fluence for desorption / ionization of Tryptophane.<sup>3</sup> In this case the compound that demonstrated the strongest UV absorption acted as a matrix that promoted the desorption / ionization of the other. Around the same time a closely related technique, which uses a suspension of nanoparticles as matrix was developed by Tanaka *et al.*<sup>9</sup>

At present, MALDI is a well-established technique for the analysis of macromolecules, like proteins, oligonucleotides and carbohydrates of up to several hundreds of kilodaltons. For a successful analysis the analyte molecules have to co-crystallize with the solid matrix material, which should be present in excess. Matrix-analyte ratios most often are in the range of  $10^3$  -  $10^5$  : 1. As a rule of thumb one can say: the higher the mass of the analyte studied, the greater the surplus of matrix molecules needed for intact desorption. The role of the matrix is believed to be fourfold: first it serves to isolate analyte molecules by dilution which prevents aggregation, second it acts as a strong absorber of the laser energy through electronic (UV-MALDI) or vibrational excitation (IR-MALDI, see section 2.1.2), third it facilitates a non-destructive transition of the analyte molecules to the gas phase and last it promotes the ionization of the analyte molecules by charge transfer.<sup>10</sup> Over the years many candidate MALDI matrices have been evaluated. Most of the matrices used, nowadays, are either benzoic or cinnamic acid derivatives. The two matrix compounds that were used in the work described in this thesis belong to these classes: 2,5-dihydroxybenzoic acid (2,5-DHB) and 4-hydroxy- $\alpha$ -cyanocinnamic acid (4HCCA). Their molecular structure is detailed in Figure 2.1. Despite the broad and early acceptance of MALDI as an important macromolecular analysis tool, the understanding of the underlying mechanisms of the desorption and ionization processes



2,5-dihydroxybenzoic acid

4-hydroxy- $\alpha$ -cyanocinnamic acid

**Figure 2.1** Molecular structures of two common MALDI matrices.

involved has only recently begun to emerge.

In its most common form MALDI uses pulsed near UV-lasers with wavelengths of either 337 nm ( $N_2$  laser) or 355 nm (frequency-tripled Nd:YAG laser). The aromatic matrix compounds have a strong absorption band in this wavelength regime, in contrast to most analyte compounds. Sometimes wavelengths further into the UV, 266 and 308 nm, are used. However, these are less favorable because of the promoted formation of matrix-analyte adducts through photochemical reactions. The pulse durations typically employed in UV-MALDI are between 0.5 and 10 ns. For these pulse lengths it is believed that the MALDI desorption process takes place in the thermal confinement regime, i.e. laser pulse durations are shorter than the time needed for the heat to dissipate out of the (light-)absorbing sample volume.<sup>11</sup> In many experimental studies it has been observed that efficient MALDI occurs above a distinct threshold in the applied laser fluence. Molecular dynamics (MD) simulations have shown that this threshold behavior most likely corresponds to the transition from a desorption to an ablation regime.<sup>11</sup> The first regime involves the thermal desorption of monomeric molecules only, while the latter is characterized by a rapid phase explosion in which also liquid droplets or clusters of molecules are emitted (Figure 2.2). The phase-explosion is thought to be responsible for the rapid cooling of the desorbed molecules, and therefore might be an important factor in the survival of large macromolecules in the desorption process. Experimental evidence for the ablation of large clusters and chunks of material in MALDI has

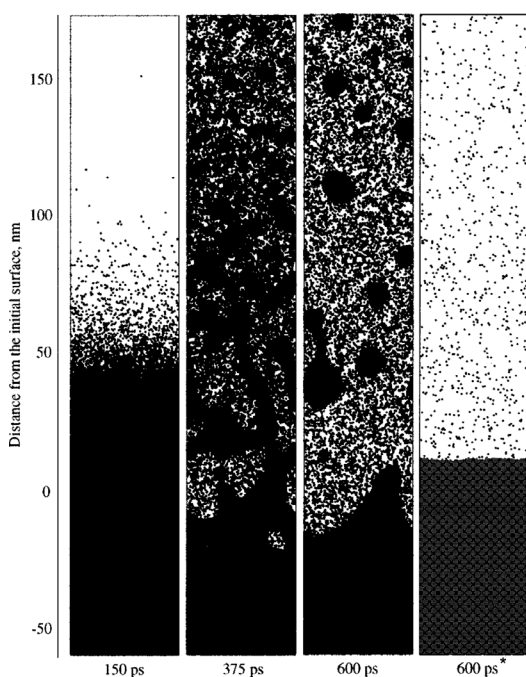


**Figure 2.2** Snapshots from MD simulations of ablation/desorption in the thermal confinement regime. The last column corresponds to lower laser fluence, which results in the desorption of individual molecules following a thermal desorption model. The first three columns display the rapid-phase change at different times after the arrival of the laser pulse with energy above the MALDI threshold fluence. (images taken from ref. 11)

been provided by trapping plate experiments, in which the desorbed material was collected and studied using Atomic Force Microscopy (AFM).<sup>12</sup> The use of longer pulse length lasers is believed to result in fragmentation of the analyte molecules by thermal excitation before the gas-phase transition takes place.<sup>13</sup> For MALDI using picosecond laser pulses the pulse duration becomes shorter than the time of mechanical equilibration of the absorbing volume. For these very short laser pulses ablation is said to take place in the stress confinement regime, which results in the ablation of large chunks of material<sup>14</sup>

Great controversy exists on the nature of the processes that result in the formation of the (analyte) ions that are detected. The main debate is on whether the detected ions are formed in secondary ion-molecule reactions in the desorption plume<sup>15, 16</sup>, making MALDI a two-step process, or as 'lucky survivors' from charged clusters<sup>17, 18</sup>. The occurrence of a laser fluence threshold as explained above and the mass independence of the initial ion velocities for peptide and protein ions have been interpreted as evidence for the formation of ions from large matrix-analyte clusters through evaporation.<sup>18</sup> In accordance with these observations a cluster ionization model for the MALDI desorption / ionization process was proposed by Karas *et al.*<sup>17</sup> In short: analytes are incorporated into matrix crystals maintaining their solution charge states<sup>19</sup>, due to the relative basicity of the analytes with respect to the matrix, their charge states will in general be protonated, the analyte species are desorbed (ablated) in (mainly singly) charged cluster ions, which are formed by charge separation of ion-pairs. The energy required to overcome the Coulombic attraction is delivered by the mechanical energy in the phase explosion process. The detected ion species are formed by evaporation of neutrals, which are formed upon interionic proton transfer in the ionic clusters.

In the two-step description of MALDI the formation of the detected species is attributed to secondary reactions taking place in the desorption plume.<sup>20, 21</sup> A strong difference with the cluster ionization model is that the necessary charge is supplied through photo-ionization instead of charge separation. In the two-step process matrix ions are formed in a primary ionization event during or right after the laser pulse. The most likely pathways for ionization are excited-state proton transfer and energy pooling (Figure 2.3).<sup>21</sup> R. Knochenmuss developed a quantitative model describing the primary ionization event using just excited state energy pooling.<sup>22</sup> In an expanded version of this model the formation of the detected analyte ions formed in secondary ion-molecule reactions is accounted for through a simple charge transfer reaction.<sup>16</sup> This model succeeds to reproduce experimental observations, like the matrix-suppression effect<sup>20</sup> and time-delayed two-pulse MALDI<sup>23</sup>. Recently, it has also been observed that the ionization potential of matrix molecules in analyte-matrix clusters is strongly reduced, making two-photon absorption a candidate pathway for primary ionization as well.<sup>24</sup> At the same time this observation indicates the importance of the occurrence of clusters in MALDI, also within the framework of the two-step description.



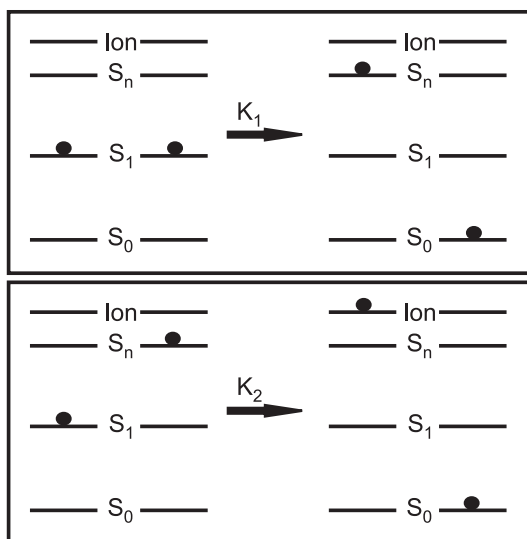


**Figure 2.3** 2,5-DHB excited state energy pooling in MALDI as proposed by R. Knochenmuss. The processes indicated are used in the model of refs. 16 and 22 to produce 2,5-DHB ions, which can take part in secondary proton transfer reactions to form the detected macromolecular ions.

### 2.1.2 IR-MALDI

Successful MALDI experiments have been performed using infrared lasers as well. In IR-MALDI the energy is directed into the matrix molecules using either the O-H or N-H stretch vibrations at  $2.94\ \mu\text{m}$  irradiation or the O-H bending and C-H stretch vibrations at  $10.6\ \mu\text{m}$ . It has been shown that, besides many of the matrices used in UV-MALDI, glycerol<sup>25</sup> and ice<sup>26</sup> can be used as matrices in IR-MALDI. Especially, from the point-of-view of biological applications water / ice would be a very convenient matrix. The amount of material removed in an IR-MALDI experiment is many times higher than in a UV-MALDI experiment. The depth of the laser induced crater in the matrix crystals in UV-MALDI is estimated to be around  $100\ \text{nm}$ <sup>27</sup>, while a single pulse in IR-MALDI removes material up to a few micrometers depth<sup>28</sup>. Therefore the mass resolution obtained is generally better in UV-MALDI, which is also the more sensitive of the two techniques. On the other hand IR-MALDI is believed to be the softer ionization method and therefore best suited for studying labile complexes.<sup>29</sup> The mechanisms underlying desorption and ionization in IR-MALDI are not as extensively studied as is the case for UV-MALDI, therefore the nature of the differences and similarities between both ionization techniques are still under debate. Most results in literature are obtained using either  $100\ \text{ns}$  pulses from an Er:YAG ( $2.94\ \mu\text{m}$ ) laser or  $6\ \text{ns}$  pulses from an OPO (optical parametric oscillator) system tuned in the  $3\ \mu\text{m}$  range. Photoacoustic measurements on a glycerol sample have revealed different desorption / ablation characteristics for the two pulse lengths, which could be linked to the occurrence of a stress confinement regime ( $6\ \text{ns}$  pulse) or thermal confinement regime ( $100\ \text{ns}$  pulse), similar to the UV-MALDI case.<sup>30</sup> Because of the increased penetration depth of the IR-laser the stress and thermal confinement conditions are

fulfilled at rather different pulse lengths than for the UV-MALDI case. From this respect the way the energy is coupled into the sample, either through electronic or vibrational excitation seems to be unimportant.

### 2.1.3 Secondary ion mass spectrometry

In SIMS a primary ion beam of several kiloelectronvolts of kinetic energy imparts on a solid or liquid surface producing secondary species, both neutral and ionic in nature, the ionic species are subsequently analyzed using mass spectrometry. Primary ions that are used include  $\text{Ga}^+$ ,  $\text{In}^+$ ,  $\text{Cs}^+$  and more recently cluster-ions like  $\text{Au}_n^+$ ,  $\text{SF}_5^+$ ,  $\text{C}_{60}^+$  and  $\text{Bi}_n^{m+}$ . Two operational regimes are distinguished: dynamic and static SIMS, respectively. The dynamic SIMS regime is characterized by high ion current densities and associated fast erosion of the sample surface. The high primary ion currents used, are very destructive, therefore dynamic SIMS can only be applied for the elemental characterization of surfaces. In addition, the fast erosion of the surface allows high-resolution depth profiling ( $\sim 1$  nm). Its main applications are in the field of material analysis, for instance the semi-quantitative analysis of pollutants in semiconductor materials for microelectronics fabrication. Much lower primary ion current densities are used in static-SIMS. This regime of operation is defined by the so-called static limit, the primary ion dose for which less than 1% of the top surface layer atoms and molecules have interacted with the primary ion beam. By this definition the surface layer is virtually undisturbed and the primary ion beam will hit a fresh spot on the sample in every cycle of the analysis. The static limit is often quoted to be  $10^{13}$  impacts per square centimeter of the sample. While this is a good estimate for elemental targets and atomic species, it is not for intact organics or characteristic fragments thereof. This becomes clear from another quantity: the damage cross-section, which is defined as the average area per incident particle from where ejection of a specific species is excluded. Values for damage cross sections for small organics have been determined yielding values around  $10^{-13}$   $\text{cm}^2$ . This number implies that true static-SIMS operation for organic sample surfaces is limited to ion doses of  $10^{11}$  to  $10^{12}$  primary ions per square centimeter. The use of low ion currents in static-SIMS facilitates the detection of informative molecular fragments, which is impossible in dynamic SIMS. Although fragmentation is still extensive static-SIMS is more suitable for the analysis of organic samples; in the remainder of this introductory chapter we will concentrate on this SIMS methodology, referring to it as SIMS.

The SIMS sputtering process can be described through a collision cascade (Figure 2.4). In the case of an atomic solid: the primary particle collides with the sample surface and penetrates into the sample where its energy is dissipated through collisions with atoms it encounters. If these collisions are energetic enough the atoms that were set in motion will collide with other atoms present in the sample keeping the cascade going. This will result in the ejection of a near-surface species when it receives sufficient outward-directed momentum to escape the sample, overcoming the surface binding energies. The analytical description of sputtering events from solid targets has been a subject of study from the end of the 19<sup>th</sup> century. Sigmund

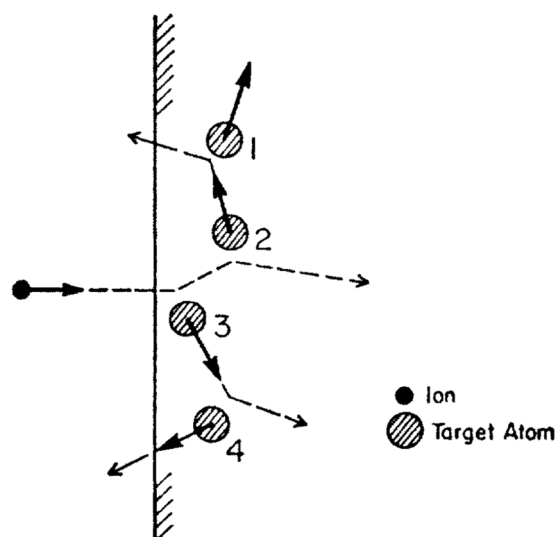


**Figure 2.4** The collision cascade introduced in sample by the impinging ion. Some of the atoms set in motion are sputtered from the sample (2 and 4) while others are displaced deeper into the sample (1 and 3). Taken from ref. 31.

combined available knowledge in a collision cascade model, which can describe sputter yields, emission depths and kinetic energies of ions produced from an atomic solid using particle beams.<sup>31</sup> In the case of sputtering from an organic sample the energetic collision cascade will induce extensive fragmentation and chemical rearrangement of the molecules present in the sample. In many cases this prevents the detection of intact molecular ions or even informative fragments.

Nowadays, MD simulation is an important tool to get insight in the fundamentals of organic sputtering.<sup>32</sup> Using many-body interaction potentials the evolution of each particle's position, velocity and energy can be monitored over time. It has been shown that MD simulations can be used to reproduce experimental data on kinetic energy distributions of sputtered ions<sup>33</sup> emission depths<sup>34, 35</sup> and surface energy profiles<sup>36</sup>. The occurrence of special events like the ejection of intact macromolecules can be traced back to specific trajectories in the simulation. In this way it has been shown that intact macromolecules (2 kDa) can be lifted from a sample within a specific regime in the collision cascade (thermal spike regime)<sup>37</sup> which is characterized by collective motion of particles in so-called high yield events.<sup>38</sup> In these events the collision cascade is concentrated near the surface, creating an excited volume in which correlated motion of substrate / sample particles induces the ejection intact macromolecules. Recently,

the similarity of the MALDI and SIMS desorption processes was pointed out, in both techniques the collective (ablative) motion of material induced either by photon absorption (MALDI) or primary ion impact (SIMS) seems to be key to the generation of intact molecular ions.<sup>35</sup>

#### 2.1.4 Strategies to improve molecular ion yields in SIMS

As was outlined above the wide scale application of SIMS for the analysis of biological samples is hampered by the extensive fragmentation of organic compounds. At present several strategies are followed to overcome this limitation. Results obtained with polyatomic primary projectiles like  $\text{SF}_5^+$ ,  $\text{C}_{60}^+$ ,  $\text{Bi}_n^{m+}$  and  $\text{Au}_n^+$  are promising.<sup>39</sup> In comparison to atomic primary ions ( $\text{Ga}^+$ ) a 300-fold increase in the secondary ion yield of molecular ions of masses up to a few thousand Daltons has been observed.<sup>40-44</sup> The increase in ionization yield is believed to result from an increased density of collision cascades in the near surface region of the sample initiated by the break-up of the primary projectile.<sup>45</sup> Especially the number of events leading to multi-(molecular) ion emission increases dramatically with respect to atomic primary ions.<sup>46, 47</sup> Besides, studies with  $\text{C}_{60}^+$  and  $\text{SF}_5^+$  have shown virtually no decrease of the secondary (molecular) ion yield with ion doses exceeding the static limit on several (bulk) samples.<sup>41, 43</sup> It is believed that this is due to the very efficient removal through ablation of all material damaged in the collision cascade.<sup>48</sup>

A different approach to increase the mass range in SIMS, which is briefly touched upon in this thesis (Chapter 6) is sample metallization. In this approach the organic sample is sputter coated with a thin layer ( $\sim 1 - 3$  nm) of a metal, usually silver or gold. The yield of informative secondary ions is increased not only through metal-cationization, the detection of informative fragments and protonated molecular species is promoted as well.<sup>49-51</sup> Metal deposition onto organic samples results in the formation of nanometer size metal-islands instead of a closed film.<sup>51</sup> The enhancement is supposed to arise from the diffusion of organic molecules onto the gold/silver islands, creating desorption conditions similar to an organic film cast on a metal substrate<sup>49, 50, 52</sup>, which has been shown to promote the detection of molecular ions. However, this latter approach is not compatible with SIMS imaging of biological systems like cells and tissue.

In another strategy to improve macromolecular ion yields organics are imbedded in solid matrices. Solid matrices were already applied in SIMS analyses of organic molecules some twenty years ago, when ammonium chloride was found to be an effective matrix.<sup>53</sup> It was observed that the presence of the matrix gave rise to reduced fragmentation, indicative of a reduction of the internal energy of the organics detected. Desolvation of desorbed clusters of molecules and collisional relaxation in the selvedge region were suggested as possible mechanisms to account for this. Recently, the success of MALDI has initiated the use of MALDI-matrices in SIMS sample preparation. Co-crystallization of analytes with MALDI matrices like 2,5-dihydroxybenzoic acid facilitates the detection of macromolecular ions of masses over 10 kDa in a methodology termed matrix-enhanced SIMS (ME-SIMS).<sup>54</sup> Thereby,

## *2.2 Chemical image generation in biomolecular imaging mass spectrometry*

it is, at present, the only SIMS based ionization methodology that is successful in the generation of intact high mass biomolecular ions. It has been suggested that the role of the matrix in ME-SIMS bears similarities to that in MALDI: providing a nestle environment for the analyte molecules and a source of protons to enhance ionization. Best results are obtained with 2,5-dihydroxybenzoic acid as matrix, as a possible explanation for this it was argued that it would promote the concentration of analyte species in the surface region of the sample.<sup>54</sup> Since in ME-SIMS (as opposed to MALDI) only the direct surface region of the sample is probed the localization of the analyte species is of crucial importance in the sample preparation, this was also recognized by other authors.<sup>55</sup> Recent MD simulation studies showed that 2kDa polystyrene molecules can be desorbed with equal yields from a silver substrate as from a low molecular weight matrix.<sup>35, 52</sup> It was argued that the matrix enhancing effect should be attributed to ionization effects (charge state in the sample or proton transfer in gas phase) and for larger molecules isolation effects (preventing the formation of aggregates).<sup>35</sup> In this same MD study association of matrix molecules with analytes during the early stages of the desorption event was observed, which shows resemblance with the MALDI desorption / ablation process.

## **2.2 Chemical image generation in biomolecular imaging mass spectrometry**

In the following the different strategies that exist to generate chemical or ion images from sample surfaces are discussed. The limitations of MALDI and SIMS microprobe macromolecular imaging MS are discussed and the beneficial characteristics of microscope mode imaging are pointed out.

### **2.2.1 Microprobe mode imaging MS (general)**

Microprobe mode imaging MS is by far the most frequently used MS imaging methodology. It is performed by scanning the ionizing probe beam across a sample (SIMS) or by moving the sample through its focus (MALDI). For every position the ionizing beam imparts on the sample the spatial coordinates are stored and a mass spectrum is obtained (position correlated ion generation). In this way a raster is built; every point in the raster has a mass spectrum associated to it. Using dedicated software mass resolved ion images can be constructed from such datasets. The maximum achievable spatial resolution in a microprobe imaging experiment is determined by the size of the microprobe. Furthermore, the experimentally achieved spatial resolution is influenced by factors related to sample preparation (application of matrix) and sensitivity (signal-to-noise ratio). The mass spectrometers employed in imaging MS are mostly

Time-of-Flight (ToF) mass analyzers. This is for various reasons: 1) their high transmission efficiency, 2) their wide mass range capabilities and 3) their speed of operation (especially important in SIMS).

## 2.2.2 MALDI microprobe mode ion imaging

The microprobe spot sizes that are used in most MALDI imaging MS experiments on commercial instruments vary between 25 and 200  $\mu\text{m}$ .<sup>7, 56, 57</sup> The laser spot sizes in the 25-200  $\mu\text{m}$  range are well suited for protein profiling analysis in which a comparison on basis of detected protein signals between different parts of a sample, for instance of brain tissue, is made. For single cell or even subcellular imaging smaller spot sizes are needed. The spot sizes used in MALDI imaging MS are not limited by the wavelength of the light used, but rather by the configuration of the source region of the mass spectrometers, which is not optimized for creating a tightly focused microprobe. This requires the last (focusing) objective to be placed inside the vacuum near the sample plate, blocking the desorbed ions or influencing the accelerating field. Recently, Spengler and Hubert circumvented this with a clever design in which the last focusing lens contains a central hole fitted with a steel tube through which ions can be extracted.<sup>58</sup> In this way a microprobe of approximately 1  $\mu\text{m}$  was achieved. Nevertheless, until now no high-mass protein signals have been reported from spot sizes of 1  $\mu\text{m}$  or smaller. In a publication by Dreisewerd *et al.* it was observed that the laser threshold fluence ( $\text{J}/\text{m}^2$ ) for the generation of protein ions from matrix crystals increases rapidly for decreasing spot sizes.<sup>59</sup> The laser fluence threshold going from a 200  $\mu\text{m}$  diameter spot to a 10  $\mu\text{m}$  diameter spot was increased from 70 to 1600  $\text{J}/\text{m}^2$ . These observations could indicate a fundamental limitation to the smallest laser spot from which protein ions can be generated. A possible explanation might be that reduction of the absorbing volume will require a higher fluence for ablation since on the timescale of the laser pulse duration a significant part of the absorbed energy will leak out of the absorbing volume as heat. The elevated laser fluences induce extensive (thermal) fragmentation and thereby reduce sensitivity. Also for larger spot sizes sensitivity can be a factor that restrains the achievable spatial resolution. The use of small microprobes is only beneficial if the sensitivity is adequate for the detection of the quantities of analyte present in sample on the scale of the microprobe footprint.

The preparation of the sample for analysis with MALDI can affect the experimentally achievable resolution. A detailed description of the different steps involved is given elsewhere,<sup>60</sup> here we focus on the application of the matrix. With respect to matrix deposition two (opposing) criteria have to be fulfilled in order to acquire high-lateral resolution peptide and protein images. First, the deposition of the matrix should not affect the spatial distribution of the peptides/proteins in the sample (tissue). Second, sufficient surface wetting of the sample is needed to form matrix crystals, which contain co-crystallized peptides/proteins. The highest ion yields are obtained by simply applying a large droplet of matrix solution covering the whole tissue. Drawbacks of this approach are the formation of large crystals, up to several hundred micrometers, which is a measure of the distance over which compounds can migrate through

dissolution. Besides, it has been shown that during drying the crystals themselves can migrate over distances up to 400  $\mu\text{m}$ .<sup>61</sup> To minimize migration of compounds matrix can be applied using an air spray or electrospray deposition (ESD) method. In this way the matrix is applied to the tissue in a spray of very small droplets, resulting in very small matrix crystals ( $\sim 1\text{-}5\ \mu\text{m}$ ). The difficulty in these approaches is to achieve sufficient surface wetting needed for the extraction of analytes from the tissue.

The acquisition time in a microprobe experiment is directly correlated with the spatial resolution / microprobe laser spot size. In general MALDI microprobe imaging experiments can be time consuming, lasting up to several hours for the analysis of a 1 mm by a 1 mm tissue section at typical 25  $\mu\text{m}$  resolution. The recent introduction of nanosecond pulse length, frequency tripled Nd:YAG lasers capable of high repetition rates (50 – 1 kHz) will certainly shorten the acquisition times. In chapter three a comparison with acquisition times that can be achieved with microscope mode imaging, introduced in Section 2.2.3, is made.

### 2.2.3 SIMS microprobe mode ion imaging

The primary ion beam used in SIMS imaging can be focused to a very small spot, ranging from 50 nm for an atomic primary ion beam to about 2  $\mu\text{m}$  for a  $\text{C}_{60}$ -polyatomic ion beam. Therefore microprobe SIMS imaging is capable of generating chemical images of very high-resolution. There are numerous examples in literature where SIMS imaging successfully has been applied to biological / pharmaceutical systems.<sup>62-65</sup> As was pointed out before its weakness is the extensive fragmentation of molecular species, which limits the sensitivity for the detection informative organics. Therefore biomolecular ion imaging using SIMS, even with polyatomic projectiles, is restricted to small biomolecules like cholesterol, small peptides and characteristic fragments like the phosphocholine headgroup ( $m/z\ 184$ ) for the phospholipid species phosphatidyl choline.

Very recently, ME-SIMS was used for the imaging of biologic systems.<sup>66-68</sup> The application of ME-SIMS for imaging purposes increases the sensitivity but introduces sample preparation that influences the spatial resolution. In high-resolution matrix-assisted imaging mass spectrometry it is very important to apply the matrix in a way that minimizes the amount of smearing of compounds through dissolving in the matrix solution. This is achieved by covering the sample with very small droplets of matrix solution through a gas-nebulizer or ESD device. This last method can produce matrix crystals of approximately 1  $\mu\text{m}$  diameter. In the ME-SIMS studies mentioned the yield of organics clearly increased upon application of matrix to the tissue while no evidence for smearing was observed, a lateral resolution of 2.6  $\mu\text{m}$  was estimated. These results prove the feasibility of ME-SIMS imaging of biological systems, though the yield enhancement is limited to those compounds that are enriched in the surface area of the sample. The application of metallization to real-world samples is currently investigated in our group. This could be another interesting application especially in combination with the use of polyatomic primary ions.

Although in SIMS the rate at which primary ion packages bombard the sample is very high (up to 10 kHz), the low ion current densities used lengthen the acquisition. An analysis of a 150 x 150  $\mu\text{m}$  area can last up to 10 minutes.

## 2.2.4 Microscope mode ion imaging

SIMS imaging mass spectrometry was originally developed as a stigmatic ion microscopy technique. This technique also known, as microscope mode ion imaging is a very elegant ion imaging technique, which differs fundamentally from the scanning microprobe technique discussed above. The differences with microprobe mode MS imaging are nicely illustrated in Figure 3.1. Conceptually it closely resembles wide field (light) optical microscopy; it uses stigmatic ion optics to project a magnified secondary ion image of the sample on to a 2D-detector. Using SIMS stigmatic ion microscopy images with 0.5 – 1  $\mu\text{m}$  resolution were obtained for atomic ions and small organics.<sup>69-71</sup> Nowadays, with the development of highly focused liquid metal ion guns capable of 50 – 200 nm resolution, the scanning microprobe methodology has become the standard in imaging SIMS.

Although stigmatic ion imaging cannot compete with the high spatial resolution that is achieved in SIMS microprobe analysis there are other aspects to it, which make it especially interesting for application with macromolecular ionization techniques like MALDI. For ionization techniques that are not compatible with small spot sizes the concept of stigmatic ion imaging is very valuable. This has not been recognized over the past years, which is clear from the little attention it has received. The principle of position correlated ion detection instead of position correlated ion generation removes the demand for a tightly focused microprobe to achieve high lateral resolution imaging MS. This offers a much greater versatility in choice of ionization sources than for microprobe mode imaging. Since no tightly focused microprobe is needed the fundamental limitation on the achievable resolution in UV-MALDI imaging, mentioned above, does not apply to microscope mode imaging. In this way also ionization techniques like massive cluster ionization<sup>72</sup> and IR-MALDI become compatible with high resolution MS imaging. The maximum ionization area that can be probed at once is limited only by the field-of-view of the mass spectrometer defined by its stigmatic ion optics. For the TRIFT system used in this in thesis the field-of-view is approximately 250  $\mu\text{m}$ . The large area illumination in a microscope mode experiment makes the methodology inherently faster than a microprobe mode experiment.



## 2.3. Experimental techniques

### 2.3.1 The TRIFT mass analyzer

The majority of experiments, described in this thesis were performed on a Physical-Electronics Triple Ion Focusing Time-of-Flight (TRIFT) mass spectrometer.<sup>70, 71</sup> All SIMS and ME-SIMS microprobe experiments were conducted with an Indium ( $\text{In}^{115+}$ ) primary ion beam from a liquid metal ion gun (LMIG). The LMIG can be operated at different beam energies, ion currents and either in bunched or un-bunched mode, depending on whether the application requires high mass resolution or high lateral resolution. The ion currents typically used in (static-)SIMS range from  $\sim 50$  pA to 2 nA. In the bunched mode the primary ion package is compressed to a 1 ns pulse for high mass resolution analysis (up to  $m/\Delta m = 15000$  for organic ions), while in the un-bunched mode the 15-20 ns primary pulse is not compressed which enables a tighter focus (down to 250 nm). Depending on the ion current used the number of ions per pulse ranges from 5 to 150. During acquisition the ion beam is scanned rapidly across the surface to analyze a new area with every pulse. The repetition rate of the pulsed primary ion beam can be as high as 8 kHz depending on the mass range of the experiment. For the MALDI microscope mode experiments a  $\text{N}_2$ -laser was coupled to the TRIFT system (section 2.3.2).

The TRIFT is a TOF mass spectrometer equipped with electrostatic analyzers (ESAs), which deflect the secondary ions over  $270^\circ$  to the detector (Figure 2.5). The flight path of the ions has a length of 2 meters. Before the secondary ions generated enter the drift region, they are accelerated in a 2.1 mm long acceleration region to a nominal energy of 3 keV. The ESAs are energy dispersive ion optical elements, which provide the time focusing needed for high mass resolution. Ions of different kinetic energy will follow different flight paths through the mass spectrometer (faster ions have longer flight paths than slower ones, Figure 2.5A). In this way the ESAs compensate for flight time dispersion introduced by differences in the secondary ions' kinetic energies from the accelerating field energy. These kinetic energy variations result from energy gain in the desorption process or energy loss in events occurring above the sample surface, like collisions and ionization and fragmentation reactions. At 3 kV sample potential the energy acceptance window of the ESAs is approximately 160 eV. For secondary ions with a wide initial kinetic energy distribution mass resolution can be improved through the use of an energy filter, which is positioned just before the second ESA where the sputtered ions are dispersed maximally according to their kinetic energy (Figure 2.5B). The energy filter consists of a plate with a wide slit and a knife-edge. The knife-edge can be used to cut out the high-energy ions while the slit is used to selectively transmit ions within a 50 eV pass band. A different factor, which influences the ion's flight time and thereby the achievable mass resolution, is the secondary ion's emission angle. A series of different sized apertures, the so-called contrast diaphragm, is located just before the first ESA, where ion trajectories are

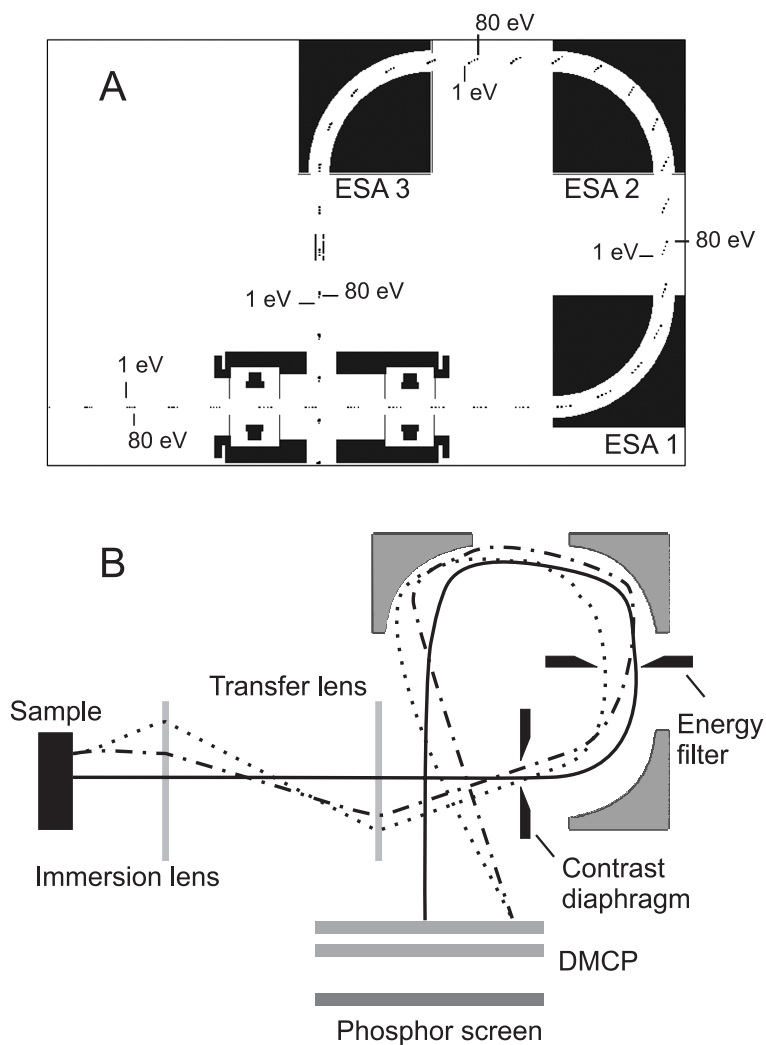


**Figure 2.5** The TRIFT ion optics. **(A)** Result of a SIMION simulation of the flight paths of ions with a 80 eV kinetic energy spread. The three electric sector analyzers facilitate time focusing to improve mass resolution. **(B)** The lines indicate trajectories of the ions that are projected on to the 2D-detector by the stigmatic ion optics. The positions of the contrast diaphragm and the energy filter, which can be used for further improvement of the mass and lateral resolution are indicated.

separated maximally according to their emission angle. The contrast diaphragm can be used to filter out secondary ions emitted at large angles with respect to the ion optical path.

The TRIFT can be operated in microprobe mode as well as microscope mode. For this latter purpose it contains stigmatic ion optics, which comprises of an extraction lens (the immersion lens), a transfer lens and the three ESAs (Figure 2.5B). The ESAs facilitate achromatic image transport with unit magnification, while the two electrostatic lenses create a magnified ion optical image. The system is equipped with two transfer lenses, which are positioned at different distances from the immersion lens. Depending on the transfer lens selected magnification factors of 80-350 times have been demonstrated. The lateral resolution that can be obtained is affected by the spread in the initial kinetic energy and the emission angles. The maximum achievable resolution is given by the diameter of the aberration spot<sup>70</sup>:

$$d_a \approx (2z\Delta E_0 / V_0) \sin \alpha (1 - \cos \alpha) \quad (2.1)$$

where  $z$  is the length of the acceleration region,  $\Delta E_0$  is the spread in initial kinetic energy,  $V_0$  is the acceleration potential and  $\alpha$  the emission angle. From this expression it becomes clear that the energy filter and contrast diaphragm can be used to increase the lateral resolution (at the cost of sensitivity). The width of the initial kinetic energy distributions of ions sputtered in SIMS depends highly on their nature. For atomic ions these can be as wide as 30 eV, while for organics the width is around a few eV. The initial kinetic energy distributions of organic ions created in MALDI are very narrow, but the direct ion extraction needed in stigmatic ion microscopy induces significant energy deficits, possibly due to collisions (see also Chapter 3).

### 2.3.2 MALDI microscope mode imaging

For the MALDI microscope experiments described in this thesis the light of a 337 nm, 3 ns pulse length  $N_2$  laser (VSL-337ND-S, Laser Science, Newton, USA) was directed to the TRIFT's sample stage. A schematic representation of the set up that was for this purpose and the electronic trigger signals needed is shown in Figure 2.6. The light is coupled into a 200  $\mu\text{m}$  diameter, 6 meter long optical fiber that is used to homogenize the intensity distribution across the laser spot, to obtain an approximate top-hat distribution. The exit of the fiber is one-to-one imaged onto the sample, through a home-built laser-inlet system with maneuverable ( $x$ - $y$ - $z$ ) last focusing lens placed inside the vacuum at a distance of 35 mm from the sample. Microscope mode ion images are recorded directly of the phosphor screen using a CCD camera (Imager 3, La Vision, Goettingen, Germany). Initially ion signals were recorded with a 4 GS/s digital oscilloscope (Waverunner LT374L, LeCroy SA, Geneva, Switzerland), which eventually was replaced by an 8-bit PCI-digitizer card (DP 240, Acqiris, Geneva, Switzerland). Triggers for the CCD camera and oscilloscope / PCI-digitizer card are provided by a photodiode, which picks up the light scattered from the beam attenuator. The duration of the analysis part of one cycle of a microscope mode experiment is dependent on the selected mass range and takes maximally 900  $\mu\text{s}$ . Within this time a series of ion images, separated in time arrives at the phosphor screen. Currently, the duty cycle of the experiment is limited by the

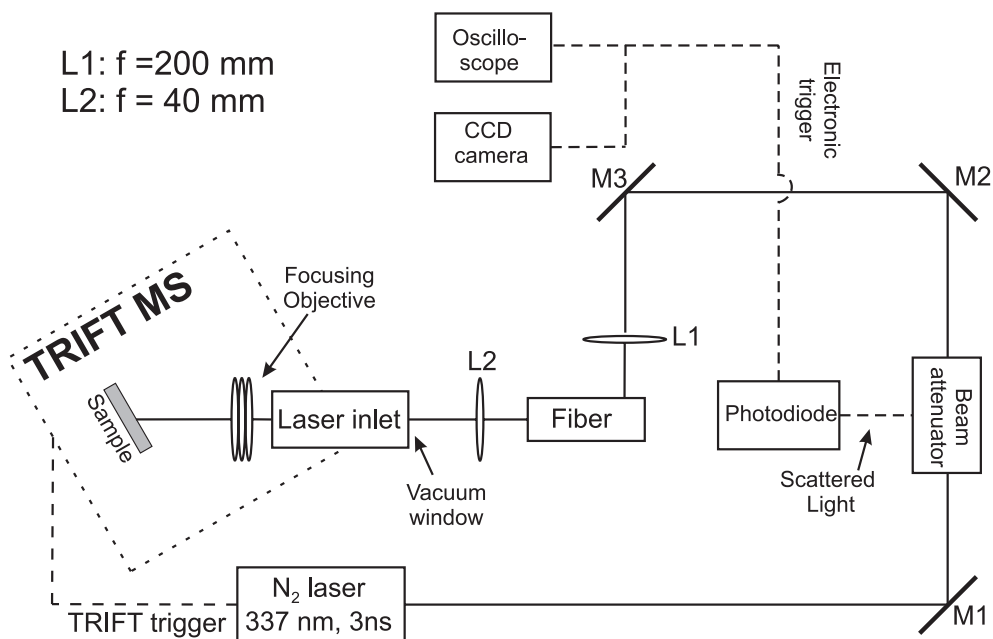


**Figure 2.6** A schematic representation of the experimental set-up that controls the illumination of the sample and the electronic triggers involved in a microscope mode MS imaging experiment.

laser system used, which has a maximum repetition rate of 30 Hz. The laser's external trigger input cannot accept the high repetition rate ( $> 1100$  Hz) at which the electronic triggers from the TRIFT are delivered. For this reason these trigger signals are fed into a frequency divider circuit first. The speed of operation of the CCD camera (exposure time  $\geq 1$  ms) currently limits microscope mode imaging to one image per laser shot, the subsequent images arriving at the detector cannot be recorded separately. So-called post-ESA blanking plates allow the selection of a particular mass window for mass resolved ion imaging. When a 200V potential is applied to these plates secondary ions are deflected from their flight paths and will not reach the detector. A selected mass window is gated by switching the potential on the blanking plates off and back on at definite times after the firing of the laser pulse. This delay is generated using a Stanford delay generator (model DG535). A time diagram for the detection of a selected peptide is included in Chapter 3, Figure 3.2. In order to record all mass resolved ion images generated separately a different type of detector is required: a delay line detector<sup>73</sup>. Implementation of this type of detector will make it possible to take full advantage of the potential of microscope mode MS imaging.

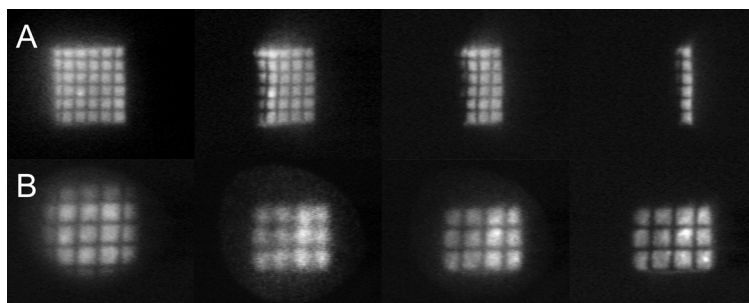


**Figure 2.7** Stigmatic images of a Cu-Al grid for comparison of different modes of operation of the TRIFT. **(A)** Normal settings; the filter acts as a spatial filter. From left to right: the knife edge of the energy filter is moved into the pathways of the secondary ions. **(B)** Energy filter settings; with the immersion and transfer lenses set correctly the filter acts as an energy filter. These images are taken through the energy slit. From left to right: the filter is moved into the direction of lower kinetic energy.

### 2.3.3 Kinetic energy distributions

The energy filter consists of a knife edge and a slit, which can be placed in the secondary ion beam. The standard version of the energy filter is a plate with a wide slit and a knife-edge. The knife-edge can be used to cut out the high-energy ions while the slit is used to selectively transmit ions within a particular energy band. The slit has a fixed width corresponding to a 50 eV pass band. We modified the energy filter such that its slit width can be varied from 50  $\mu\text{m}$  to 2 mm, corresponding to pass bands of 1 to 35 eV. In its normal mode of operation the secondary ion trajectories are maximally dispersed at the position of the contrast diaphragm according to the ions' emission angles. In order to be able to use the energy filter, the secondary ion optics have to be tuned differently. In normal operation the positions of the secondary ions in the plane of the energy filter, perpendicular to the ion-optical flight axis, are directly correlated to their origins in the sample. With different settings of the immersion and transfer lenses the secondary ion trajectories can be maximally dispersed according to the ions' kinetic energies just in front of the second ESA, at the position of the energy filter (see Figure 2.5B). In Figure 2.7 stigmatic ion images of a Cu-Al grid that were recorded for the different settings of the ion optics (2.7A: normal settings, 2.7B energy filter settings) are shown. From the leftmost images, which were recorded with the energy filter in its retracted position, it becomes clear that the different settings also result in a change in ion optical magnification factor. The subsequent images in Figure 2.7A were recorded with the energy filter knife edge moving in from the outside along the horizontal in the plane perpendicular to the ion optical axis. It is clear that for normal settings of the TRIFT the filter acts as a spatial filter instead of as an energy filter. The images in Figure 2.7B are recorded through the energy slit. As can be seen in Figure 2.5A the high kinetic energy ions are located towards the outside of the mass

## Chapter 2

spectrometer. The images in Figure 2.7B are arranged going from high energy to low kinetic energy. It is apparent that lateral resolution is increased with decreasing kinetic energy. This effect is especially noticeable for inorganic ions, which are generated in a wide range of initial energies ( $\sim 30$  eV).

The energy filter can be scanned through the secondary ion beam to record kinetic energy distributions (KEDs) of the ions sputtered of the surface. This results in a curve of the ion flux versus position of the energy filter. The kinetic energy distributions of atomic ions are well described by Thomson's formula<sup>74</sup>:

$$j(E) \propto \frac{E}{(E + U)^3} \quad (2.II)$$

with  $j(E)$  the flux of ions sputtered from the surface,  $E$  the kinetic energy and  $U$  the surface binding energy. The position of the energy filter scales linear with the kinetic energy of the ions transmitted. The zero on the energy scale can be derived from the crossing of the tangential to the decaying slope (low energy) of the ion flux with the energy filter translation axis. Thereby the energy scale is defined relative to the acceleration energy, the resolution is determined by the slit width. This makes that it can have negative values as well, therefore the x-axis is labeled apparent kinetic energy (for examples see chapter 6). Positive apparent energies indicate the energy gained in the desorption process. Negative apparent kinetic energies indicate an energy deficit with respect to the acceleration energy, which can have several causes, like: collisions and ionization above the sample surface or metastable decay. In chapter 6 we use the negative apparent KE side of the distribution to estimate the decay rate of metastable ions in the acceleration region of the TRIFT. The kinetic energy distributions of organic ions are not as wide as atomic KEDs; a large portion of the translational energy in the collision cascade is converted into internal degrees of freedom of the organic ion, causing fragmentation and depletion of the high kinetic energy side of the distribution.

# Rapid, high-spatial resolution mass spectrometric imaging of peptide and protein distributions on a surface

For the first time macromolecular ion microscope images have been recorded using matrix-assisted laser desorption/ionization mass spectrometry (MALDI-MS). Single shot, mass resolved images of the spatial distributions of intact peptide and protein ions over an area of 200  $\mu\text{m}$  in diameter were obtained in less than 1 millisecond at a repetition rate of 12 Hz. The magnifying ion optics of the ion microscope allowed ion images to be obtained with a lateral resolution of 4  $\mu\text{m}$ . These results demonstrate the concept of high resolution MALDI-MS imaging in microscope mode without the need for a tight laser focus and the accompanying sensitivity losses. The removal of the demand for a tightly focused ionization beam offers a greater flexibility in the choice of ionization source. The ion microscopy approach offers an improvement of several orders of magnitude in speed of acquisition compared to the conventional (microprobe) approach to MALDI-MS imaging. A discussion on the attainable spatial resolution is included.

### 3.1 Introduction

When Anthony van Leeuwenhoek first looked through his microscope he could not have envisaged how his eye as detector would come to be replaced by fast sensitive cameras and his illuminating candle by intense light sources and lasers. Now, micro-spectroscopic imaging tools are used to study the distribution and interactions of biomolecules within cells / tissue.<sup>75-79</sup> Through the use of well-established multiple fluorescent labeling techniques it is possible to study the spatio-temporal behavior of selected biomolecules in parallel in a single experiment.<sup>77</sup> Such microscopy studies have already been used to substantiate the intuition that a protein's function is correlated to its localization in the cell<sup>80, 81</sup> and to demonstrate that several diseases are associated with altered molecular distributions.<sup>82-84</sup> Despite the valuable insights already realized, any labeling technique suffers from several innate weaknesses. Arguably the most important is the need to identify the molecules of interest prior to the experiment in order to apply the appropriate label. In addition, the small number of molecules that can be investigated simultaneously in a single experiment, the possible interference of the label with the protein's normal function and the difficulties in distinguishing between specific post-translational modifications of proteins limit the application of labeling techniques as a discovery tool.<sup>85</sup> This last aspect is especially important considering that several diseases and immune responses have been associated with altered post-translational modifications.<sup>82</sup> Clearly, the desire to study disease and the complexity of biological mechanisms demands a molecule specific imaging technique that can be applied to tissues / cells directly.

Much of the emerging information concerning the chemical complexity of biological systems comes from the study of the genome and of its expression, the proteome. Mass spectrometry, one of the major techniques in this fast-moving field, possesses the chemical specificity and high sensitivity required for label-free biomolecular imaging experiments.<sup>86</sup> At the end of 1997 position-correlated mass spectrometry was used to record the spatial distributions of proteins in rat pituitary tissue.<sup>7</sup> More recently, this technique has been used to investigate cancer and Alzheimer's disease at the molecular level.<sup>57, 61</sup> At present the application of macromolecular imaging mass spectrometry is limited by sample preparation<sup>87-89</sup>, the achievable spatial resolution and analysis time.

The speed and spatial resolution limitations are intimately coupled to the methodology employed in current macromolecular imaging mass spectrometry. The experiments in the work mentioned above were all performed using matrix-assisted laser desorption ionization (MALDI)<sup>3, 4</sup> in microprobe mode<sup>90</sup>. In this microprobe approach a focused UV laser beam is fired at a single, defined spot on the sample. The resulting mass spectrum is stored along with the spatial coordinates of the spot. A new adjacent region is then illuminated and another mass spectrum recorded. This process is repeated until the entire sample area has been examined and mass spectra associated with each specific location have been obtained (Figure 3.1A). Mass resolved, chemical images of the distributions of molecules present in the sample are reconstructed from the individual mass spectra after completion of the experiment. In a well-optimized conventional MALDI system the laser spot is typically  $\geq 25 \mu\text{m}$ .<sup>57, 90</sup> As a result the



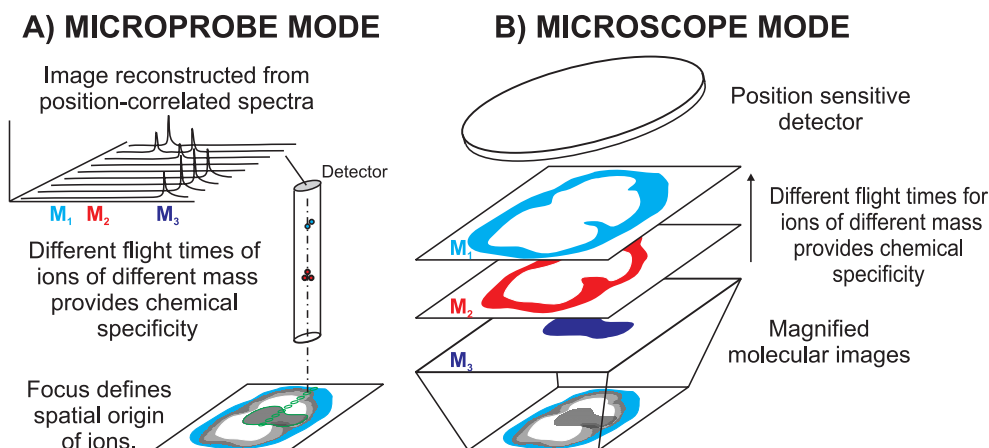


**Figure 3.1.** Schematics of the two different approaches to macromolecular imaging mass spectrometry. Microprobe mode imaging (**A**) collects mass spectra from an array of designated positions to reconstruct a molecular image after completion of the experiment (spatially resolved ion generation). In microscope mode imaging (**B**) magnified images of the ion distributions are directly acquired using a two-dimensional detector (spatially resolved ion detection).

achievable spatial resolution is insufficient for macromolecular imaging of individual cells (typical size  $\leq 20 \mu\text{m}$ ). Recently, a novel MALDI microprobe instrument has been reported that is capable of imaging mass spectrometry with a micron size laser probe.<sup>58</sup> The drawback of this approach is the high laser fluence needed to reach the ionization threshold for MALDI from such a small spot<sup>59</sup>, which leads to a high degree of fragmentation and a significant loss of sensitivity. Moreover, because each pixel is sequentially analyzed, to increase the spatial resolution by a factor  $N$  requires an increase in analysis time of  $N^2$ . This direct relation between attainable resolution and number of sequential analyses can make scanning microprobe experiments time-consuming.

Here, we present a proof-of-concept study of a novel approach to MALDI molecular imaging that combines high spatial resolution with high-speed analysis while operated at the preferable lower laser fluences. Using a mass spectrometric ion microscope<sup>70, 71</sup> the spatial resolution is independent of the spot size of the ionizing beam. This decoupling allows a much larger area to be examined without having to move the sample or the laser spot. The ions produced by a single laser shot pass through the time-of-flight mass spectrometer forming an ion-optical image on a position sensitive detector, much like in wide field optical microscopy. In this manner a mass-to-charge ratio ( $m/z$ ) separated series of molecular images is generated showing spatial detail from within the laser spot. A schematic representation of the microscope approach is shown in Figure 3.1B.

The spatial resolution that is achieved in the microscope approach depends on the quality of the ion optics and the resolution of the detector rather than on the laser spot size. Decoupling the spatial resolution from the size of the laser desorption/ionization probe has many distinct

advantages, which will be demonstrated and discussed in this chapter. These are: high spatial resolution, reduction of analysis time of several orders of magnitude and greater versatility of ionization methods applicable to imaging mass spectrometry. This work demonstrates for the first time the feasibility of macromolecular MALDI imaging of surfaces using a true ion-microscope approach.

## 3.2 Experimental section

The microscope mode imaging experiments were performed on a TRIFT II (Triple Focusing Time-of-Flight) mass spectrometer (Physical Electronics, Eden Prairie, USA). The ion optics of this mass spectrometric microscope have been designed such that a magnified ion-optical image of the surface is projected onto a two-dimensional detector<sup>70, 71</sup>. The area amenable to these microscope experiments, the field-of-vision (FOV), is typically 150 – 300  $\mu\text{m}$  in diameter depending on the ion-optical magnification.

### 3.2.1 Instrument – MALDI source

To maneuver the laser spot of the MALDI ion source within the FOV of the mass spectrometer, a custom-designed interface was constructed to control the size and position of the UV laser spot. It consists of an ultra-high vacuum (UHV) compatible microscope objective (LMU-5X-NUV, Optics For Research, Caldwell, USA) with a focal length of 40 mm and a working distance of 35 mm. This is mounted on a telescopic and maneuverable UHV flange for use with a nitrogen laser (VSL-337ND-S, Laser Science, Newton, USA), of 337 nm wavelength and 3 ns pulse duration. The pulse energy used in the experiments was measured to be between 5 and 8  $\mu\text{J}$  at the sample, for a 200  $\mu\text{m}$  diameter laser spot this results in a laser fluence of approximately 200  $\text{Jm}^{-2}$ . In the majority of the experiments described in this chapter the light of the  $\text{N}_2$  laser was coupled directly into the TRIFT using the described interface and a set of lenses and mirrors. For homogenization of the laser intensity over the sample a 6 meter long, 200  $\mu\text{m}$  diameter fiber was incorporated at a later stage. The whole grid experiments shown here were performed with the optical fiber in place. Further details on the set-up were discussed in Section 2.3.

## 3.2.2 Instrument - detection

The ions desorbed by the laser pulse are extracted from the target, and then imaged by a combination of an “immersion lens” and a “transfer lens” prior to energy compensation in three hemispherical electrostatic analyzers (see also Figure 2.5). A high-speed ion blanker is used to control the ion species that reach the detector. The ions are then post accelerated through  $-8$  kV prior to impact on a 1 inch diameter dual micro channel plate (DMCP) phosphor screen detector assembly (APD 30 25 12/10/12 PS I EDR 60:1 P-20 MgO coated, Burle Industries GmbH, Baesweiler, Germany) located in the instrument’s final image plane. The ion images formed on the phosphor screen are projected on a fast CCD camera with  $9.9$   $\mu\text{m}$  pixel size (Imager 3, La Vision, Goettingen, Germany) by a zoom lens that reduces the image size to fit the CCD chip. The total magnification obtained in the MALDI-ion microscope is determined by an ion-optical and a light-optical component. Depending on the settings of the instrument, images were recorded with  $100\times$  or  $200\times$  ion-optical magnification. The zoom lens system reduces the size of the ion image by a factor of 10.

Within one cycle of the experiment the maximum accepted flight time is  $900$   $\mu\text{s}$ , which facilitates the detection of ions of up to  $100\,000$   $m/z$ . This implies that within this  $900$   $\mu\text{s}$  interval after the arrival of the laser pulse on the sample a time-separated series of high-resolution ion images for ions of masses up to  $100\,000$   $m/z$  are projected onto the detector. However, the speed of the DMCP-phosphor screen-CCD camera combination is insufficient to record the high spatial resolution images for each analyte distribution separately, this would require repetition rate of  $50$  MHz – to  $1$  GHz. Consequently, a high-speed blanker was used to record mass-selected ion images. To insure that the switching of the blanker did not disturb the ion images an unblanked time window of approximately  $3$   $\mu\text{s}$  was used. In this manner single analyte images were obtained at a rate of  $12$  Hz, determined by the laser repetition rate. A  $4$  GS/s digital oscilloscope (Waverunner LT374L, LeCroy SA, Geneva, Switzerland) was used to record the MALDI signals of the DMCP phosphor screen assembly. The oscilloscope and CCD camera were synchronized using scattered light picked up by a photodiode, which enabled direct correlation between single shot images and spectra. The detection scheme is detailed in the timing diagram of Figure 3.2.

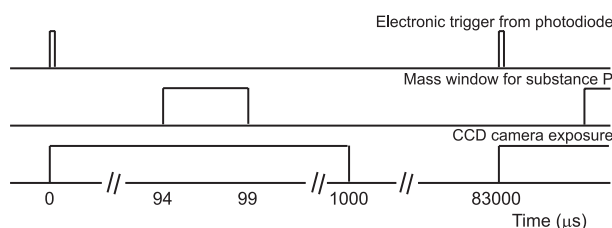


**Figure 3.2.** The timing diagram shows the sequence of events leading to the recording of single shot, mass specific ion images. In this example the blankers are tuned for the detection substance P ions.

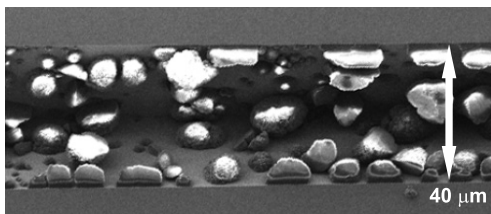


**Figure 3.3** SEM image of individual substance P doped matrix crystals in a 40  $\mu\text{m}$  wide channel etched in a silicon wafer.

### 3.2.3 Sample preparation

For the channel samples a 40  $\mu\text{m}$  wide channel was chemically etched in a boron-doped Si-wafer using KOH. The matrix-analyte solution was applied to the channel by pipeting a 1  $\mu\text{l}$  droplet at the beginning of the channel. After the channel had filled by capillary action the remainder of the droplet was removed with a pipette (Figure 3.3). The grid samples consisted of a dense mat of analyte doped matrix crystals, which were overlaid with a fine mesh grid of 2.5 mm in diameter (19  $\mu\text{m}$  squares, 6  $\mu\text{m}$  bars). The samples were prepared by deposition of 20  $\mu\text{l}$  of the premixed matrix-analyte solution on an aluminum plate. During crystallization the sample was continuously agitated, which resulted in a near homogeneous layer of small crystals. Finally, the grid was gently pressed into the crystal layer to provide a MALDI sample with recognizable microstructures. The choice for a homogeneous test sample prevented the redistribution of the analytes upon drying of the matrix crystals and the associated deterioration of the attainable lateral resolution. Experiments on a single position were performed on a sample that was made up of a 1 M solution of the matrix, 2,5-dihydroxy benzoic acid (2,5-DHB) in acetone, a 200  $\mu\text{M}$  solution of substance P (mass 1348 Da.) in 1:1 water:acetonitrile (0.05% TFA) and a solution of 300  $\mu\text{M}$  insulin (mass 5733 Da.) in 1:1 water:acetonitrile (0.05% TFA). These three solutions were subsequently mixed to obtain a matrix:substance P:insulin ratio of 10<sup>4</sup>:1:1. For the whole grid experiment a solution of 0.5 M 2,5-DHB in ethanol was mixed with 1 mM PEG-1500 in ethanol to obtain a matrix-to-analyte ratio of 10<sup>3</sup>:1. Solvents were obtained from Biosolve B.V. (Valkenswaard, The Netherlands) and other chemicals were purchased from Sigma-Aldrich Chemie B. V. (Zwijndrecht, The Netherlands); all were used without further purification. The fine mesh grids were obtained from Agar Scientific LTD. (G2780 N, Stansted, United Kingdom).

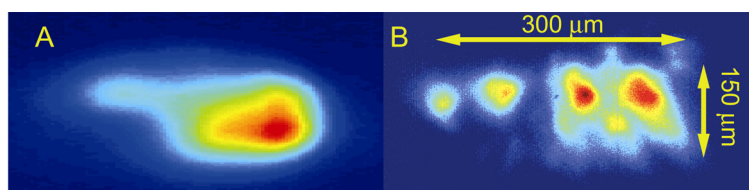


**Figure 3.4** Probing the characteristic N<sub>2</sub> laser beam profile using a 40 μm wide channel filled with matrix crystals. The channel was scanned through the laser spot at a speed of 10 μm/s. The N<sub>2</sub> laser beam profile in (A) as measured with a CCD beam profiler is reproduced by the result of the summation of the 600 individual ion images (without displacement) in (B).

### 3.3 Results and discussion

The first sample analyzed using the MALDI mass microscope consisted of a 40 μm wide channel etched in a silicon wafer filled with substance P doped 2,5-DHB matrix crystals (Figure 3.3). The sample was moved through the laser spot at 10 μm/s. For every single shot of the laser an ion image was recorded. The way this experiment was set up allowed one to probe the size and shape of the laser spot at the sample surface using the channel filled with matrix crystals as a probe. The resulting summed image is shown in Figure 3.4 together with the intensity profile of the laser measured with a CCD beam profiler. Comparison of the two images shows that the N<sub>2</sub> laser beam profile is matched by its ion optical image. From the repetition rate of the laser and the speed at which the sample was moved the dimension of the laser spot along the direction of motion of the sample (vertical in Figure 3.4) could be determined. The horizontal dimension was derived from the proportions of the spot. It is important to note that this summed image was obtained without having to shift the

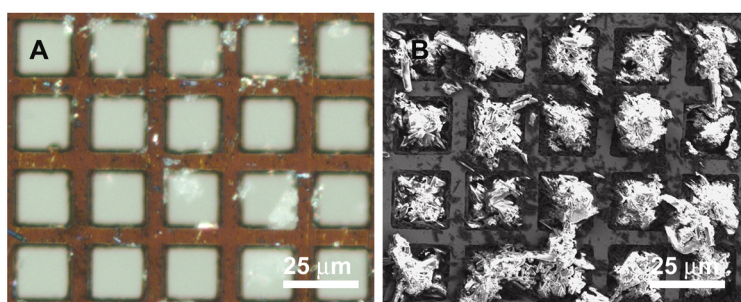


**Figure 3.5** Light microscope (A) and SEM (B) image of the fine mesh grid MALDI sample. The densely packed matrix crystals are doped with substance P and insulin.

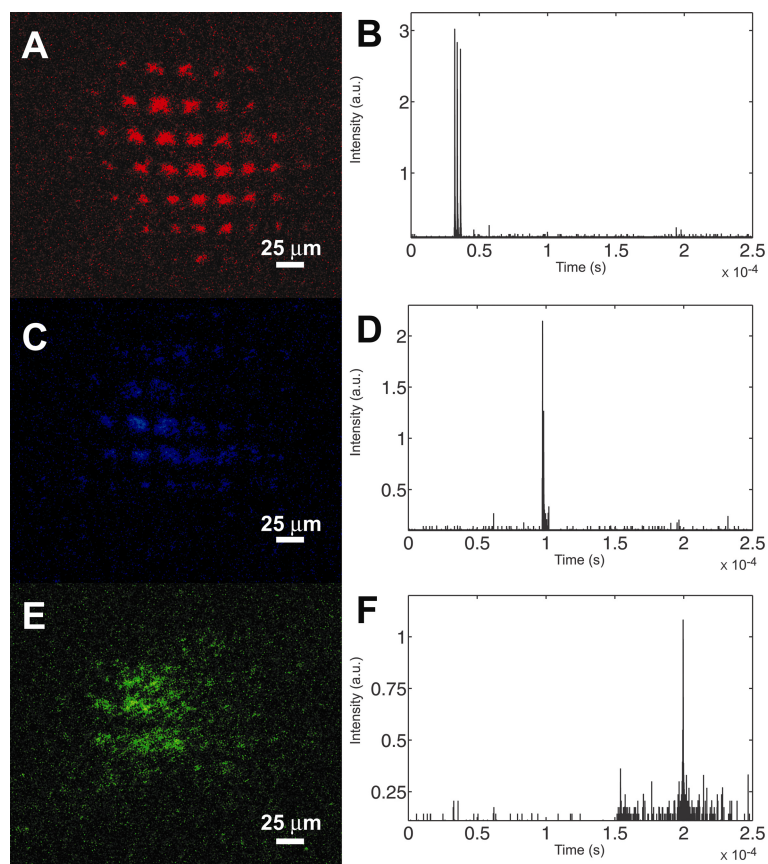


**Figure 3.6.** Typical single shot mass microscope images of the distribution of 2,5-DHB (A), substance P (C) and insulin (E) for the MALDI-grid sample. The matching single shot spectra are shown in (B), (D) and (F), respectively. In the mass window selected for the matrix ions, signals from the  $M^+$ ,  $[M + H]^+$ ,  $[M - OH]^+$  and  $[M + Na]^+$  ions were recorded. For substance P the protonated and the sodiated pseudo-molecular ions as well as a fragment,  $[M - NH_3]^+$  were detected within the gated time window and for insulin both the 1<sup>+</sup> and 2<sup>+</sup> charge states contributed to the signal.

individual images, demonstrating the microscope mode imaging capabilities. Ion images from within the etched channels (not shown) were obtained showing individual crystals but due to uncertainties about the effect of the height differences in the sample on the image quality, these samples were abandoned for further evaluation of the performance of the MALDI mass microscope.

The MALDI-grid samples, which consist of a fairly homogeneous mat of matrix crystals overlaid by a fine mesh grid, were better suited for this purpose. This kind of sample preparation results in an array of 19 μm squares that can yield MALDI signal, separated by

6  $\mu\text{m}$  bars that cannot. The light microscope and scanning electron microscope (SEM) images in Figures 3.5A and B respectively, show how the matrix crystals fill up the spaces in between the grid bars. Figures 3.6A, C and E show single shot MALDI microscope images of the distributions of matrix (2,5-DHB), substance P and insulin, respectively, obtained from within the laser probe (200  $\mu\text{m}$  in diameter). These images demonstrate that a single shot of the laser is sufficient to record the spatial distribution of the peptide and the small protein on the surface with high spatial detail. Single shot images were acquired in less than 1 ms at a laser repetition rate of 12 Hz. This results in a low duty cycle of 0.01, limited by the repetition rate of the laser. The image recording / mass analysis can accommodate laser repetition rates up to 1 kHz. The corresponding single shot mass spectra presented in Figures 3.6B, D and F show

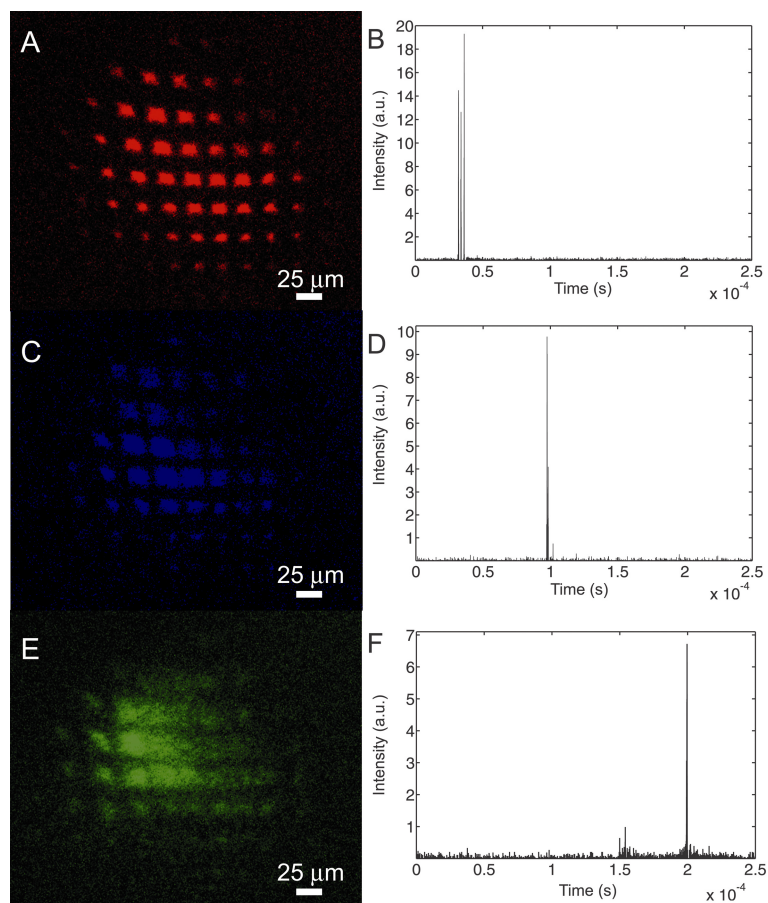


**Figure 3.7** Summed chemical images and spectra of (A) and (B) 2,5-DHB, (C) and (D) substance P and (E) and (F) insulin.

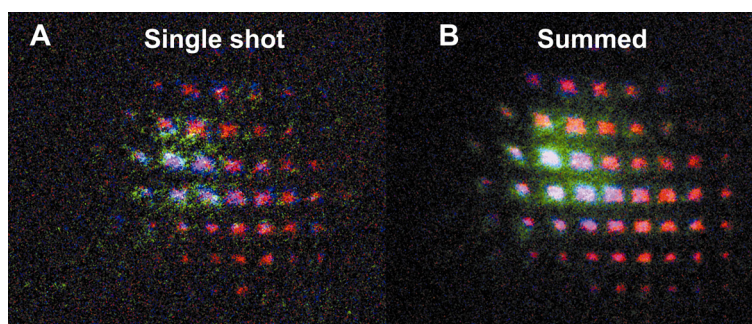
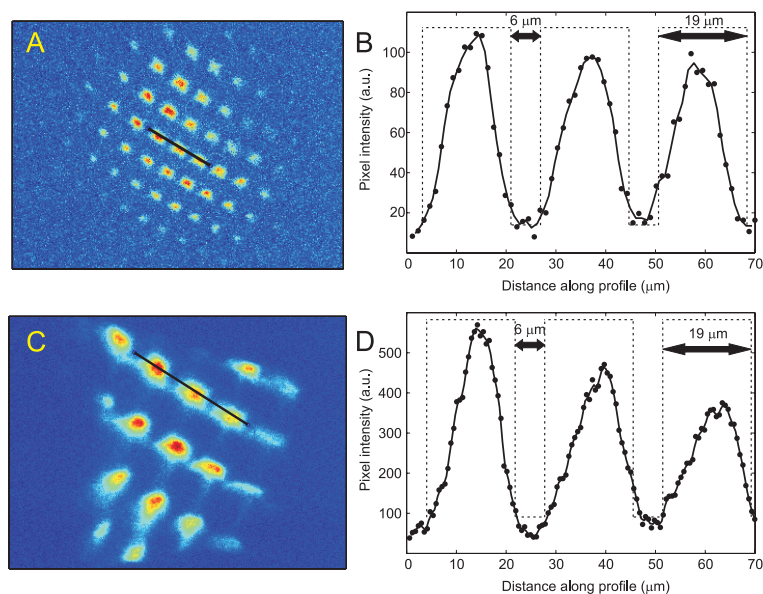


Figure 3.8 Three component ion images. From the overlay of the single shot images (A) and summed images (B) the similarity in the distributions is apparent.

that the matrix, peptide and protein images were formed by ions from the respective single compounds only. The presented single shot images are part of a series of 60 images obtained at one position, 20 images for each of the selected mass windows. The resulting summed images are shown in Figure 3.7, together with the corresponding mass spectra. The image quality improves noticeably due to the improved signal-to-noise ratio. In Figure 3.8A and B the single shot and summed images of the three constituents of the sample studied are overlaid. The three molecular distributions overlap as expected for the homogeneous sample studied. The summed images confirm that the entire laser spot was within the FOV of the mass spectrometer in these experiments. It was estimated to be approximately 200  $\mu\text{m}$  in diameter. From the known pitch of the grid and the number of CCD camera pixels across the ion image it was determined that a pixel on the CCD camera corresponded with 1  $\mu\text{m}$  on the sample. As the pixel size of the CCD camera is 9.9  $\mu\text{m}$  this result implies an overall (combined ion- and light-optical) magnification of approximately 10 $\times$ . The experimental spatial resolution of the ion-optical microscope was determined from a series of intensity profiles taken at different locations in the summed matrix image (Figure 3.9A). The intensity for each point of the profile is the result of a three-pixel average along the direction perpendicular to the profile. An example is shown in Figure 3.9B, its corresponding location in the summed matrix image is indicated in Figure 3.9A. A smooth transition from minimum to maximum intensity was observed. As a measure for the experimental resolution the distance along the profile for which the intensity had increased from 20% to 80% of the maximum value was taken.<sup>91</sup> By this definition the spatial resolution was found to be approximately 4  $\mu\text{m}$ . This is caused by the fact that the experimental resolution does not equal the pixel size but is a convolution of the detector resolution, ion-optical focusing, fundamentals of the ionization/desorption event, extraction field homogeneity<sup>92</sup> and sample morphology (see Figure 3.5). The instrument's ion optics can be tuned for a higher magnification resulting in an even smaller pixel size. For the higher magnification settings the overall magnification was 20 $\times$  and the pixel size was 500 nm (see Figure 3.9C). As the laser spot filled the entire FOV of the ion microscope in the high magnification experiments, the ion-optical magnification could be determined separately. The





**Figure 3.9.** The line in the 20 shots summed matrix image (A) corresponds to the intensity profile shown in (B). From a series of such profiles at different locations the average lateral resolution was determined to be  $4\ \mu\text{m}$ . In (C) a larger ion-optical magnification total ion image resulting from the addition of 80 single shot images is shown. An experimental resolution of  $4\ \mu\text{m}$  was found from a series of intensity profiles, of which an example is shown in (D). The lines in (B) and (D) are the result of three-point averaging of the data points in the figures.

FOV in Figure 3.9C is  $125\ \mu\text{m}$ , which implies an ion-optical magnification of  $200\times$ . Again the experimental spatial resolution was determined from multiple intensity profiles in the image (Figure 3.9D). The experimental spatial resolution for the higher magnification was found to be  $4\ \mu\text{m}$ . Although the pixel size is decreased a factor of two in the higher magnification experiment the resolving power was similar for both magnifications. In addition, a comparison of Figures 3.9B and D shows that despite a higher pixel density both magnifications resulted in similarly shaped intensity profiles. In the past, using a  $\text{Ga}^+$  liquid metal ion gun as ion source a higher resolving power of  $1\ \mu\text{m}$  has been obtained.<sup>70</sup> The factors that influence the attainable lateral resolution are discussed in Section 3.4. The experimental resolution determined here is thought to be a fair measure of the resolution obtainable in a MALDI microscope imaging experiment that is not affected by redistribution of the analytes within the matrix crystals. This redistribution of analytes is a serious issue in any MALDI-MS imaging experiment, which is briefly discussed in Section 2.2.

The small features obtained in all of the above MALDI microscope experiments would not have been discernable with the  $\geq 25\ \mu\text{m}$  spot sizes of a typical MALDI microprobe. In

<b>Microprobe mode imaging</b>		
Pixel size	No. of pixels	Resolution
100 $\mu\text{m}$	100	$\geq 100 \mu\text{m}$
25 $\mu\text{m}$	1600	$\geq 25 \mu\text{m}$
4 $\mu\text{m}$	62500	$\geq 4 \mu\text{m}$
<b>Microscope mode imaging</b>		
Field of view	No. of steps	Resolution
200 $\times$ 200 $\mu\text{m}$	25	$\approx 4 \mu\text{m}$

**Table 3.1.** A comparison of the performance of microprobe and microscope mode imaging of a  $1 \times 1$  mm sample. For ease of comparison adjacent, non-overlapping square pixels have been assumed for both methods.

contrast, multiple squares identified in the images would have been sampled by a single laser position and thus be represented as a single pixel. The spatial resolution obtained in this current work is comparable to that of the micron size microprobe study.<sup>58</sup> Moreover, these high resolution images were recorded without incurring the loss of sensitivity that is associated with the use of a highly focused laser.

We have shown that MALDI-MS imaging in microscope mode is capable of high lateral resolution. An additional strength of this approach is its speed of analysis. In comparison to the scanning microprobe approach stigmatic ion imaging offers a speed improvement of three orders of magnitude. Table 3.1 compares the number of steps necessary to analyze a  $1 \times 1$  mm sample at different resolutions using a microprobe approach. The final row of the table shows the number of steps necessary using the mass microscope. In the table the microprobe resolutions are taken as equal to or worse than the size of the microprobe, which corresponds to one pixel in the chemical image. In many imaging MS studies the distinction between pixel size and resolution is not clearly made. The resolution or resolving power in an experiment is defined as the closest proximity between two distinct features in the sample at which they can still be observed separately in an image. It is immediately clear from this definition that the probe/pixel size does not automatically equals the resolution, which can be affected by other factors like sensitivity and sample preparation as well. From Table 3.1 it is apparent that, compared to a 4  $\mu\text{m}$  microprobe, the mass microscope can analyze the same area, delivering equivalent performance, using much fewer individual positions resulting in a factor 2500 gain in acquisition time. The actual time that is gained depends on the repetition rate of the laser and the number of shots per position. A realistic 50 Hz analysis of the  $1 \times 1$  mm sample, with 25 shots per position would result in approximately 8.5 hours versus 12.5 seconds of analysis time in microprobe and microscope mode respectively.

To illustrate the concept of microscope mode large area analysis a whole grid sample, which consisted of PEG-1500 doped matrix crystals overlain with a 2.5 mm diameter hexagonal Ni-

grid structure (700 mesh), was analyzed. The entire grid was scanned through the 200  $\mu\text{m}$  laser spot in 36 linescans from left-to-right. Each linescan consisted of 800 laser shots; for every shot an image and a spectrum were obtained. In between subsequent shots the sample was moved 5.6  $\mu\text{m}$ . The shift between subsequent linescans was 100  $\mu\text{m}$  to ensure sufficient overlap with the previous scan. In this way 28800 stigmatic ion images were obtained, which were stitched together using dedicated, in-house developed software. The resulting image is shown in Figure 3.10. Since no blanking was applied the obtained image is a total ion image. The insert contains a zoom of an area of approximately 200 by 200  $\mu\text{m}$ . The individual linescans in this particular example were obtained at 9 Hz repetition rate resulting in 90 seconds of analysis time. In this time an area of 200 by 4500  $\mu\text{m}$  was analyzed. Per line scan 480 Mb image information and 80 Mb spectral information is obtained. For the whole grid analysis this adds up to 17.3 Gb versus 2.9 Gb; these numbers clearly demonstrate the need for large data storage facilities in imaging MS.

A third means by which MALDI-MS imaging can benefit from the microscope mode approach is the greater versatility in choice of ionization sources it offers. The application of position resolved ion detection instead of position resolved ion generation removes the demand for a tightly focused ionization probe for high lateral resolution MS imaging. In particular macromolecular ionization techniques like IR-MALDI and massive cluster sources become compatible with macromolecular ion imaging in this way. The feasibility of stigmatic

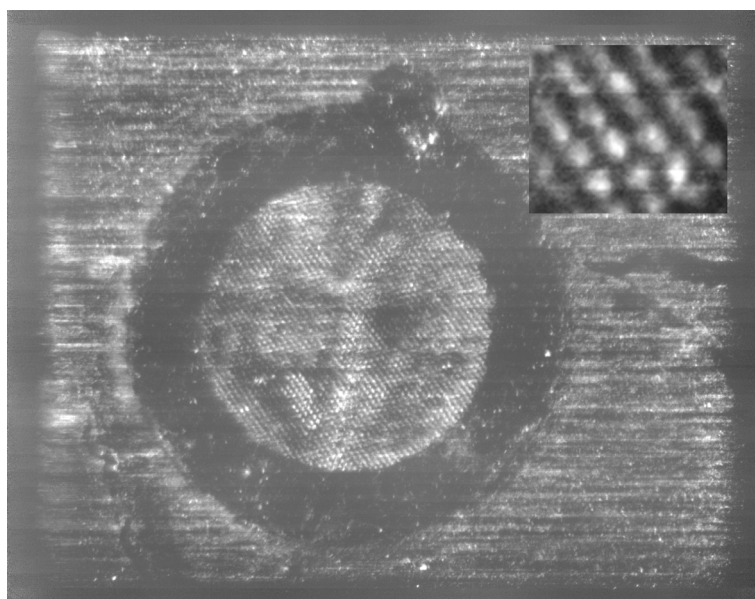


**Figure 3.10** Whole grid total ion image of PEG-1500 sample. The macroscopic image consists of 28800 individual stigmatic ion images, which have been stitched together. The inset shows an approximately 200 by 200  $\mu\text{m}$  detail.

ion imaging using IR-MALDI is demonstrated in Chapter 4.

In the discussion of the microscope mode imaging results it is important to note that in this proof-of-concept configuration the mass microscope is capable of recording one high-resolution ion image per cycle of the experiment. With the ion blankers specific mass windows can be selected. To obtain high-speed, high-resolution images for all masses with each laser shot, parallel detection of both space and (arrival-)time coordinates of the incoming ions at the detector are required. In the past a Resistive Anode Encoder (RAE) detector has been used in combination with the microscope mode imaging technique.<sup>70</sup> The severe demands on the dead-time and multi-hit capabilities make the RAE detector not suitable for MALDI microscope mode imaging. We are currently developing a delay-line detector<sup>73</sup> that satisfies our requirements with respect to parallel recording of stigmatic ion images for all  $m/z$ -values. It is always been envisaged that the MALDI mass microscope would include parallel detection of all masses. The proof of concept experiments described here were performed to test the feasibility of microscope mode imaging, prior to the development of the detector.

### 3.4 Discussion: factors influencing microscope mode lateral resolution

The ultimate spatial resolution that can be achieved on a stigmatic ion imaging system is determined by the aberration introduced in the acceleration region of the mass spectrometer / ion microscope. The aberration spot diameter can be approximated by<sup>70</sup>:

$$d_a \approx (2z\Delta E_0 / V_0) \sin \alpha (1 - \cos \alpha) \quad (2.1)$$

with  $z$  the length of the acceleration region (2.1 mm),  $\Delta E_0$  the width of the initial kinetic energy distribution of the ions generated,  $V_0$  the accelerating potential (3000 V), and  $\alpha$  the emission half-angle. In the following we will summarize what is known on the involved parameters and what their implications for the practically achievable resolution are. The velocity of the ions generated in the MALDI process is largely independent on the mass of the ions. As a result the ion's kinetic energy is mass dependent. Generally, (axial) velocities in the range of  $700 \pm 200$  m/s are quoted.<sup>93</sup> This implies energy spreads of several eV for small peptides to several tens of electronvolts for moderate size proteins. Therefore it should be expected that the attainable spatial resolution is dependent on the mass of the ions imaged. For successful stigmatic imaging the ions generated have to be extracted directly, as delayed extraction or a field-free drift region would degrade the image quality. It has been observed before that ions generated using MALDI, which are extracted directly into an accelerating field, display a kinetic energy deficit from the accelerating field energy. In addition, their kinetic energy distributions show a significant increased width.<sup>94</sup> We have measured the kinetic energy

### 3.4 Discussion: factors influencing microscope mode lateral resolution

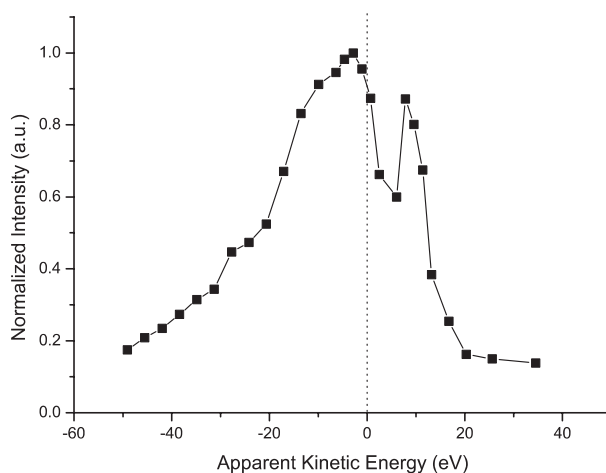


**Figure 3.11** Kinetic energy distribution of the peptide Leucine Enkephaline. The distribution is centered around an energy deficit of 5 eV with a FWHM of 35 eV.

distribution of leucine enkephalin ( $m/z$  556) on our TRIFT system for the accelerating field used in the imaging experiments; the result is shown in Figure 3.11. The average kinetic energy value is negative, around -5 eV, the FWHM of the distribution is approximately 35 eV. This is in great contrast with the values expected, based on initial velocity measurements:  $1.5 \pm 0.8$  eV. The width and energy deficit increase with mass and increasing laser fluence. Gas-phase collisions in the plume and ion formation from ionized matrix-analyte clusters were pointed out as the most likely explanations for these observations.<sup>94, 95</sup> The ions' emission angles form another factor affecting the later resolution in a microscope mode experiment. The angular distribution of the ions formed in the MALDI process has been analyzed by several authors.<sup>96-98</sup> In these studies a strong forward peaking of the analyte ions in the MALDI plume was reported. The relatively low radial velocities observed, imply emission angles as low as  $15^\circ$  half-angle. According to equation 2.1, emission angles of this order, in combination with the measured initial kinetic energy spread, would result in lateral resolutions of the order of  $0.5 \mu\text{m}$ . A hand-waving argument to explain the discrepancy from the observed lateral resolution would be that collisions in the source region cause the ion trajectories to be slightly distorted resulting in a degradation of the lateral resolution. On the other hand it has been reported before that the ions ejected in MALDI are, on average, directed back towards the direction of the laser.<sup>99</sup> In the study mentioned a  $60^\circ$  angle of incidence resulted in a  $30^\circ$  emission angle. In our set-up the laser comes in under a  $35^\circ$  angle with the spectrometer axis, an emission angle of approximately  $20^\circ$  would already result in a resolution of  $2.4 \mu\text{m}$  for an energy distribution width of 35 eV. Therefore it is very likely that the emission angle indeed has a significant effect on the maximum achievable resolution. From the above discussion it becomes clear that several instrumental settings as well as characteristics of the MALDI desorption process affect

the maximum attainable lateral resolution. Several strategies to maximize the resolution can be distinguished. Exploration of these different strategies will also result in better understanding of the different factors contributing to the experimental lateral resolution.

- **Emission angles.** An angular filter, a series of different size apertures called contrast diaphragm (Figure 2.5), can be used to limit the transmittance of ions to smaller emission angles. Since in MALDI the angular distributions of analyte ions display strong forward peaking ( $\sim \cos^{280}$ )<sup>96</sup> the contrast diaphragm can be used without incurring dramatic sensitivity losses. A reduction of the half-angle of emission from  $15^\circ$  to  $10^\circ$  for such a distribution would result in transmission of 90% of the ions while a factor 3 increase in resolution is possible.
- **Initial Kinetic Energy.** Just before the second ESA the generated ions are maximally dispersed according to their kinetic energy. At this position a filter can be placed in the ion beam to limit the transmission to ions within a specific energy window only. For this purpose we have developed an adjustable energy filter, the width of the energy window can be varied between 1 and 35 eV. Preliminary studies have shown that indeed the spatial resolution is improved using the energy filter. The spatial resolution depends linearly on the width of the initial kinetic energy distribution according to Eq. 2.I. From Figure 3.11 it is clear that the ions with large energy deficits ( $\geq 20$  eV) can be filtered out without large costs on ion transmission. An interesting experiment would be to select the positive energy part of the distribution of ions (Figure 3.11). It is believed that these ions are formed early in the MALDI process. Their kinetic energy distributions are not so much affected by collisions or charging of the sample. In addition the fewer collisions will also minimize distortion of the ion trajectories.
- **Accelerating potential.** According to equation 2.I increase of the sample potential limits the effect of the width of the angle and energy distributions. The highest possible accelerating potential in our current set-up is 5 kV, which by itself might lead to a resolution improvement in the order of 1.7 times. A drawback may be that increase of the sample potential will broaden the initial kinetic energy distributions, due to the more energetic collisions in the source region.<sup>94</sup>
- **Laser Intensity.** The width of the kinetic energy distribution increases with increasing laser intensity. This is the result of the larger amount of material that is ablated. The number of collisions will increase which also results in a higher degree of distortion of the ion trajectories, further compromising the attainable lateral resolution. Operation near MALDI threshold is beneficial for the ion image quality in microscope mode imaging.

### 3.5 Conclusions

In this study we have demonstrated the feasibility of MALDI microscope mode imaging. The test samples we have used, delivered us the recognizable structures needed to prove the concept of MALDI microscope mode imaging. In addition they served as useful targets to estimate the experimental spatial resolution, which was determined to be 4  $\mu\text{m}$ . Several ways to improve the resolution beyond this value were discussed. The high spatial resolution, the increased speed and the greater versatility of potential ion sources offered by the mass microscope approach will prove important in the further development of macromolecular mass spectrometric imaging. The quality of the results obtained justifies further studies in which microscope mode imaging will be applied to biological samples. In addition, the implementation of the (x, y, t)-delay line-detector<sup>73</sup> with high spatial and temporal resolution combined with multi-hit capabilities will enable the full potential of the microscope mode approach for mass spectrometric imaging to be exploited.





# Infrared mass spectrometric imaging below the diffraction limit

Matrix assisted laser desorption/ionization mass spectrometry (MALDI-MS)<sup>3, 4</sup> is an established technique for the analysis of biological macromolecules. Its relative insensitivity to pollutants makes MALDI-MS very suitable for the direct analysis of biological samples. As such it has facilitated great advances in the field of biomolecular imaging mass spectrometry. Traditionally, MALDI-MS imaging is performed in a scanning microprobe methodology<sup>7, 57, 88</sup>. However, in a recent study we have demonstrated an alternative methodology; the so-called microscope mode<sup>100</sup>, in which the requirement for a highly focused ionization probe beam is removed. Spatial details from within the desorption area are conserved during the flight of the ions through the mass analyzer and a magnified ion image is projected onto a 2D-detector. In this chapter we demonstrate the compatibility of high resolution microscope mode MS imaging with IR-MALDI. For the first time high-lateral resolution ion images were recorded using infrared MALDI at 2.94  $\mu\text{m}$  wavelength. The resolution achieved was well below the diffraction limited laser spot size that can be obtained with the set-up used, which is impossible to achieve in the conventional scanning microprobe approach.

## 4.1 Introduction

Nowadays, MALDI-MS is an established technique for the analysis of macromolecules. In its most familiar form, MALDI-MS is performed using pulsed ultraviolet lasers (UV-MALDI). The matrix molecules typically used in UV-MALDI experiments act as strong UV absorbers. The absorption of UV-photons by the matrix molecules initiates a very rapid solid-to-gas phase transition. In the desorption plume the macromolecular ions that are eventually detected are formed by gas-phase reactions or as lucky survivors from charged clusters.<sup>21</sup> Already a few years after the first UV-MALDI experiments it was recognized that by coupling energy into the vibrational modes of the matrix molecules instead of their electronic states, one could also benefit from the ‘matrix effect’.<sup>101</sup> This allowed the wavelength range to be extended to the infrared (IR-MALDI), in particular around the OH-stretch vibrations ( $\lambda = 2.94 \mu\text{m}$ ). A considerable advantage of using IR lasers in this wavelength range is the possibility to use matrices that do not alter the physiological conditions of the sample under investigation, in contrast to the acidic matrices that are required for UV-MALDI. Over the years several reports on IR-MALDI have appeared in which ice and glycerol were used as matrices.<sup>25, 26</sup> This is of particular interest for the analysis of biomolecules directly from biological tissue and cells. As such the use of infrared lasers would offer great benefits for MALDI-MS imaging. An important drawback in using IR-MALDI for high resolution imaging MS is the difficulty of focusing a  $2.94 \mu\text{m}$  laser to a small microprobe.

In scanning microprobe imaging mass spectrometry the analysis spots are defined by stepping the sample stage carrying the target through the focus of a laser beam; the beam diameter determines the maximum achievable lateral resolution. Unfortunately, even diffraction limited focusing of a  $2.94 \mu\text{m}$  laser beam in the non-optimized environment of a mass spectrometer cannot deliver a small enough spot required for high lateral resolution scanning microprobe imaging. To illustrate this problem we have calculated the minimum diffraction limited spot size that can be obtained with the optical system used in this study to focus the light of a  $2.94 \mu\text{m}$  Er:YAG laser onto the sample target in the mass spectrometer, a TRIFT-II (Physical Electronics Inc., Eden Prairie, MN, USA). Since the last focusing lens is positioned inside the mass spectrometer its maximum diameter and minimal focal length are limited, to 12.7 mm and 50 mm respectively. The radius of the smallest possible spot size for the lens used equals the Airy disk radius:<sup>102</sup>

$$R = \frac{1.22f\lambda}{D} \quad (4.1)$$

where  $f$  is the focal length and  $D$  the aperture of the focusing lens ( $f = 50 \text{ mm}$ ,  $D = 12.7 \text{ mm}$ ). Hence for a  $\lambda = 2.94 \mu\text{m}$  laser the Airy disk radius equals  $14 \mu\text{m}$ . According to Rayleigh’s criterion for resolution the radius of the Airy disk defines the resolving power of an optical system.<sup>102</sup> In a microprobe mass spectrometric imaging experiment, the maximum attainable lateral resolution is defined by the achievable laser spot size. According to this definition, the

diffraction limited resolving power in a scanning microprobe experiment with the set-up described would be 28  $\mu\text{m}$ .

In Chapter 3, we demonstrated a novel concept in MALDI imaging mass spectrometry using large area illumination and spatially resolved ion detection instead of spatially resolved ion generation, the so-called mass microscope approach. Since this is a true ion imaging methodology, the spatial resolution is no longer determined by the size of the desorption / ionization probe (the laser spot), but rather by the quality of the ion optics and the detector. Hence, one can expect the lateral resolution that can be obtained in IR-MALDI microscope mode imaging to be similar to that found in the UV experiments, being 4  $\mu\text{m}$ . This would imply a resolution considerably better than the theoretical limit calculated above.

## 4.2 Experimental section

### 4.2.1 Instrumental

The light of a Q-switched Er:YAG laser ( $\lambda = 2.94 \mu\text{m}$ , 100 ns pulse length, Bioptic, Berlin, Germany) is coupled into a triple focusing time-of-flight (TRIFT, Physical Electronics, Eden Prairie MN, USA) mass spectrometer using a set of silver coated mirrors and an in-house built laser introduction / focusing system. The light is transmitted through a  $\text{CaF}_2$  window (ISP Optics, Irvington, NY) and focused onto the sample using a 12.7 mm diameter, 50 mm focal length plano-convex  $\text{CaF}_2$  lens (Thorlabs Inc., North Newton, NJ) which was positioned such that the resulting spot size was approximately 200  $\mu\text{m}$  in diameter. The TRIFT uses stigmatic ion optics<sup>70, 71</sup> to project a magnified ( $\sim 100 \text{X}$ ) ion optical image of the distribution of ions generated from the sample on a dual multichannel plate – phosphor screen detector. The fluorescence of the phosphor screen is monitored by a fast CCD camera (Imager3, LaVision, Goettingen, Germany). Further details of the experimental setup are described in Chapters 2 and 3 of this thesis.

### 4.2.2 Sample preparation

A matrix solution of 0.25 M succinic acid in 1:1 ethanol:water was thoroughly mixed with an analyte solution of 1mM bradykinin in 1:1 ethanol:water. The matrix-to-analyte ratio in the resulting mixture was 5000-to-1. The final mixture was applied to a steel plate and continuously stirred to obtain a dense mat of matrix/analyte crystals. In order to provide recognizable structure to the sample, a fine mesh nickel grid (1000 mesh, 6  $\mu\text{m}$  bar) was gently pressed into the sample.

### 4.3 Results and discussion

Here, we present high-resolution ion images that were obtained using IR-MALDI imaging in microscope mode. To demonstrate the high lateral resolution this methodology is capable of, we have designed a test sample consisting of a steel sample plate covered with a fairly homogeneous layer of matrix-peptide crystals, in turn covered by a fine mesh nickel grid (25  $\mu\text{m}$  pitch, 6  $\mu\text{m}$  bars) to provide recognizable structure. The peptide used in this study was bradykinin ( $[M + H]^+ = 1060.6$  Da). The ion image in Figure 4.1A is the result of a single laser shot. The corresponding single shot mass spectrum is shown in Figure 4.1B. Although no mass selection of ions was applied, i.e. ions of all masses were allowed to reach the detector, the mass spectrum demonstrates that the main contribution to the image in Figure 4.1A comes from bradykinin.

To estimate the lateral resolution we first determined the pixel size of the images, which equals the detector-limited resolution. The area on the sample that was imaged onto one pixel of the CCD camera was estimated from the known dimensions of the fine mesh nickel grid overlaying the crystal mat by averaging various intensity profiles. An example of such a profile is shown in Figure 4.2. From a series of such intensity profiles the pixel size was estimated to be approximately 900 nm. The pixel size found here is slightly lower than in chapter 3 due to larger light optical magnification of the phosphor screen projection onto the CCD camera chip. The spatial resolution was estimated according to the following definition: the distance along the intensity profile for which the intensity has dropped from 80% to 20% of its maximum value.<sup>91</sup> In this way the spatial resolution in a single shot experiment was found to be 4  $\mu\text{m}$ . The resolution found equals that of the UV experiments reported earlier but at an 8.7 times longer wavelength.

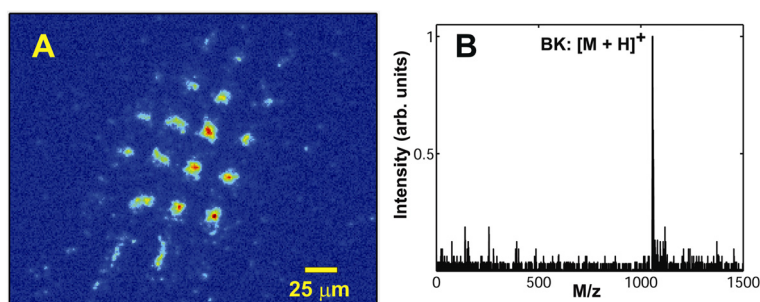


**Figure 4.1.** Single shot ion image and corresponding mass spectrum. (A) A single shot IR-MALDI ion image of the succinic acid – bradykinin sample. This image was obtained by large area illumination with a ‘defocused’ IR laser. The ions were observed over an area of approximately 150  $\mu\text{m}$  in diameter (B) The corresponding mass spectrum shows that the major contributions to the signal come from the bradykinin ions.

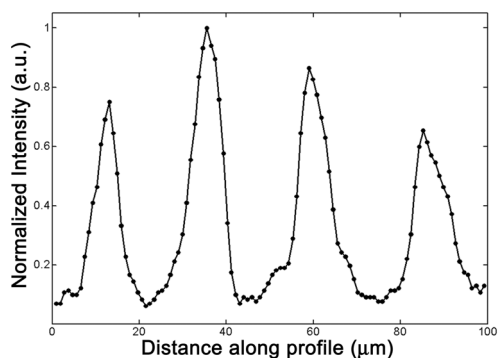


**Figure 4.2.** Intensity line profile across four squares in the image of Figure 4.1A. The pixel size and lateral resolution that were achieved in the experiment were estimated by averaging of several of these intensity profiles. The displayed pixel intensities are the result of a three-point average.

From previous studies it is known that in IR-MALDI experiments a significant amount of material is removed with each laser shot.<sup>28</sup> One might expect that an accompanying elevated density in the source region can introduce distortions to the recorded ion images, for instance due to collisions. The 4  $\mu\text{m}$  resolution found in this study equals that of a previous microscope mode study using UV-MALDI. From this we conclude that the resolution in IR-MALDI microscope mode imaging does not suffer from the amount of material removed in the desorption / ionization event. The ion image presented in this study was recorded in one cycle of the mass spectrometer, which takes 900  $\mu\text{s}$ ; in this short time detailed mass spectral and spatial information is obtained.

## 4.4 Conclusions

The present work demonstrates that IR-MALDI is compatible with high resolution imaging mass spectrometry in microscope mode. Using a pulsed 2.94  $\mu\text{m}$  laser, single shot 150  $\mu\text{m}$  diameter ion images were obtained within 1 ms. The obtained resolution equals that of a previous microscope mode study using UV-MALDI, which implies that the IR-MALDI ionization process does not degrade the quality of the ion images that were obtained. Microscope mode MS imaging is the only way to record high resolution ion images with an IR laser; these cannot be obtained using a diffraction limited scanning microprobe approach.

**Acknowledgement.** We would like to thank Andreas Haase of Bioptic for the loan of the Bioscope Q-switched Er:YAG laser and for his help with the alignment of the laser.



# The Effect of Local Matrix Crystal Variations in Matrix-Assisted Ionization Techniques for Mass Spectrometry

We obtained intense intact molecular ion signals from phosphatidylcholine, phosphatidylethanolamine, phosphatidylglycerol and phosphatidylinositol using matrix-enhanced secondary-ion mass spectrometry (ME-SIMS). It was found that the high mass regions ( $> m/z$  500) of the ME-SIMS spectra closely resembled those obtained using matrix-assisted laser desorption/ionization (MALDI). Using high spatial resolution imaging SIMS, a detailed investigation of dried-droplet samples was performed. Based on the detected  $\text{Na}^+$  and 2,5-DHB matrix signal intensities, different crystal types were distinguished, in addition to different sizes of crystals. Spatially mapping the pseudo-molecular and fragment ions of the phospholipids revealed that the nature of the pseudo-molecular ions formed, as well as the ratio of intact molecular to fragment ion, was dependent on the type and surface composition of the crystal. The observed chemical bias effects due to crystal heterogeneity and the resulting variation in desorption/ionization efficiency will complicate the interpretation of data obtained from matrix assisted mass spectrometric (imaging) techniques and is an important factor in the 'hot-spot' phenomenon frequently encountered in MALDI experiments. In this respect imaging SIMS was found to be a versatile tool to investigate the effects of the local physico-chemical conditions on the detected molecular species.

## 5.1 Introduction

Chemical imaging mass spectrometry offers unique opportunities for obtaining more insight into numerous complex biochemical processes. Recording the distribution of elements and biomolecules in cells and tissues will help to address many issues in today's cell biology and medicine; applications vary from membrane dynamics<sup>65</sup>, drug delivery systems<sup>103, 104</sup> to altered protein distributions in diseased cells<sup>57</sup>. Currently, MALDI<sup>3, 4, 57</sup> and SIMS<sup>105</sup> are most frequently used in imaging MS experiments of biological samples.

MALDI is one of the most versatile techniques for the ionization of large, non-volatile biologically relevant molecules, such as peptides, proteins and nucleotides.<sup>21</sup> In the MALDI imaging approach spatial information is obtained by scanning the sample through the (UV-) laser beam. Over the last couple of years a number of reports have appeared using scanning MALDI to image biological tissue.<sup>7, 61, 88</sup> The spatial resolution achieved in these studies is determined by the laser spot size and was optimized to be approximately 25  $\mu\text{m}$ . While this is insufficient to obtain the spatial distribution of the molecules within a cell (the diameter of an average mammalian cell is approximately 20  $\mu\text{m}$ ), it has allowed the spatial distribution of proteins in a tissue to be recorded. Recently, several efforts to improve the attainable spatial resolution in MALDI MS imaging experiments have been reported. Spengler *et al.*<sup>58</sup> developed a novel confocal microscope / laser scanning MALDI instrument that enables peptides to be imaged with micron resolution (and inks with sub-micron resolution). In chapter 3 of this thesis stigmatic ion optics were used to demonstrate the feasibility of high lateral resolution microscope mode MALDI MS imaging.

In SIMS a high energy (10 – 25 keV) primary ion beam is used to irradiate a sample surface. Upon impact of the primary ions neutrals, molecular ions and atomic ions are liberated from the sample surface. The secondary ions are subsequently mass analyzed. By scanning the primary ion beam over the sample surface information on its chemical composition is obtained. The achieved spatial resolution is determined by the primary ion beam spot size, which is typically a few hundred nanometers. Although the lateral resolution in SIMS is much better than in MALDI, the ion formation process leads to a higher degree of fragmentation of large molecules. Among other factors the degree of fragmentation roughly scales with the density of primary ions and is one of the distinctions between the two regimes of operation in SIMS: dynamic and static SIMS. Dynamic SIMS uses a relatively intense primary ion beam to sputter the sample surface. This results in the removal of material at a rate of 1-10 nm s<sup>-1</sup> and destruction of most molecular species in the sample.<sup>2</sup> Dynamic (imaging) SIMS has proven to be a powerful tool for the recording of distributions of elements (Na, Ca, K, Mg etc.) present in cells as well as for the imaging of isotopic gradients.<sup>106, 107</sup> In static SIMS a much less intense primary ion beam is used.<sup>2, 108</sup> The primary ion dose (< 10<sup>13</sup> ions cm<sup>-2</sup>) is significantly smaller than the average density of atoms in a surface monolayer (10<sup>15</sup> atoms cm<sup>-2</sup>).<sup>2, 109</sup> Consequently, within the static SIMS regime the majority of primary ions collide with (and secondary ions are obtained from) a fresh region of the sample surface. In addition: the lower primary ion density in static SIMS results in greater yield of (low weight) intact molecular ions and fragments,



allowing limited molecular information of a surface to be obtained. Owing to the low yield of intact molecular ions, static SIMS chemical images of bio-surfaces generally are fragment ion maps. Recently, Winograd and co-workers have used static SIMS to successfully probe the chemical composition of freeze-fractured cell membranes and liposomes.<sup>63, 65, 110</sup> In these studies no matrices were used to enhance intact phospholipid ion yield and to reduce fragmentation.

The energy required to liberate a molecule from a surface increases rapidly with increasing mass. For both SIMS and Laser Desorption Ionization (LDI), in which energy is passed to the analyte molecules almost directly, fragmentation is increasingly favored over desorption/ionization. As a result the signal intensity of intact molecular ions decreases rapidly with increasing mass. The strongly reduced fragmentation in matrix-assisted LDI is largely subscribed to the matrix molecules absorbing most of the UV laser pulse energy. In the rapid phase change that follows analyte ions are desorbed as part of evaporative clusters and/or undergo gasphase reactions.<sup>10, 21</sup> In much the same line of reasoning it was found that by diluting the analyte molecules in a matrix (thereby reducing the direct interaction with the primary ion beam) the desorption/ionization yield of intact proteins, peptides and oligonucleotides in SIMS was enhanced significantly. This methodology has been termed Matrix-Enhanced SIMS (ME-SIMS).<sup>54</sup> The similarity of the more recently proposed mechanisms for macromolecular ionization by MALDI and SIMS, a localized phase change<sup>111</sup> and collective motion<sup>35</sup>, respectively, help rationalize the matrix enhancement for both techniques, despite their widely differing natures. Although this finding increased the potential of SIMS for the analysis of large biomolecules, only few publications on ME-SIMS have appeared since.<sup>112-115</sup>

For any matrix-assisted ionization technique it holds that the application of matrix to the system of interest will introduce local physico-chemical changes, which can affect the spatial and chemical information obtained. Non-uniformities in the matrix layer (crystals) can cause ionization yields to vary across the sample. As a result 'hot' (or 'sweet') spots will exist within a sample. These will hinder the interpretation of spatial information obtained in matrix assisted imaging studies. The dissolution of analytes into the bulk of the matrix droplet will further limit the achievable lateral resolution to the size of the matrix crystals. While the spot size of the laser in MALDI imaging is such that multiple crystals are sampled in each shot and effective averaging of all but the larger scale bias effects will occur, any attempt towards obtaining higher spatial resolution will have to include circumventing these distortions. In ME-SIMS imaging the resolution is potentially only limited by the size of the matrix crystals. Therefore understanding the effect of locally varying sample conditions on the species detected from the sample will be crucial in high resolution matrix-assisted mass spectrometric imaging. Assuming that the results from a surface sensitive technique (SIMS) compare to a bulk analysis technique (MALDI), imaging SIMS analysis of matrix-analyte crystals will also give insight in the occurrence of specific pseudo-molecular ions (protonated or alkali adducts) and fragments in MALDI, since high spatial resolution SIMS relates their occurrence directly to the local physico-chemical conditions.

With a view towards recording the spatial distribution of phospholipids in a cell membrane using ME-SIMS, a study on the effects of the local sample heterogeneity using purified phospholipids was undertaken. The high spatial resolution capabilities of the SIMS methodology allowed an in-depth investigation of the chemical heterogeneity of the crystals. The high intensity of the molecular ions obtained using ME-SIMS and the mapping capabilities of a high resolution SIMS imaging approach demonstrated that different molecular ions were obtained from the different types of crystals produced by dried-droplet deposition. ME-SIMS results from this study and MALDI results from both literature<sup>116</sup> and this present study show great similarity. This suggests that the local variations in detected species encountered here would also be present in a MALDI study of the same surfaces. However, these variations can only be visualized with a spatial resolution equal to or better than that obtained with ME-SIMS.

## 5.2 Experimental section

### 5.2.1 Sample preparation

The phospholipids used in this study were phosphatidylcholine (PC) and phosphatidylethanolamine (PE), two of the main constituents of mammalian cell membranes, phosphatidylglycerol (PG), which (besides PE) forms a large fraction of the *E. Coli* cell membrane and phosphatidylinositol (PI), which is a precursor of important cellular signaling molecules.<sup>117, 118</sup>

The phospholipids and the matrices: 2,5-dihydroxybenzoic acid (2,5-DHB) and ferulic acid were purchased from Sigma-Aldrich Chemie GmbH (Germany) and used without further purification. All phospholipids except PI, were obtained in a purified form: 1-oleoyl-2-palmitoyl-sn-glycero-3-phosphocholine, 1-palmitoyl-2-oleoyl-sn-glycero-3-phospho-rac-(1-glycerol) and 1-palmitoyl-2-oleoyl-sn-glycero-3-phosphoethanolamine. The PI sample was prepared from soybean and contained mainly linoleic and palmitic fatty acid chains according to the manufacturer. The phospholipid molecular structures are included in Figures 5.1 and 5.7. The stock solutions used in these experiments, consisted of 1.8 mM PC in methanol, 1 mM PE in dichloromethane (DCM) : methanol (1:1), 2.5 mM PG in DCM and 1.8 mM PI in DCM, 0.5 M 2,5-DHB in methanol and a saturated solution of ferulic acid in 1:1 water : acetonitrile. The matrix and analyte solutions were premixed to a specific matrix : analyte ratio (see Table 5.1). In the ME-SIMS dried droplet experiments 1-2  $\mu$ l of the final solution was applied to a Si wafer and allowed to dry. Typically, the process of drying took a few seconds when methanol was used as solvent and approximately one minute when the water-acetonitrile mixture was used. For the SIMS control experiments (without matrix) the stock solutions were

	Pulse (ns)	Bunching	Mass res. (m/ $\Delta$ m)	Spatial res. ( $\mu$ m)	Ion dose ( $\text{cm}^{-2}$ )	Matrix: analyte
PC (+)	10	Yes	7500	3	$9 \times 10^{11}$	1100 : 1
PG (+)	20	No	1400	1	$10^{12}$	2500 : 1
PE (+)	10	No	2350	1	$7 \times 10^{11}$	5000 : 1
PC (-)	10	Yes	a)	b)	$6 \times 10^{11}$	5000 : 1
PG (-)	10	No	4100	b)	$3 \times 10^{11}$	2500 : 1
PE (-)	10	Yes	a)	b)	$6 \times 10^{11}$	5000 : 1
PI (-)	10	Yes	4200	b)	$9 \times 10^{11}$	c)

**Table 5.1** An overview of the experimental parameters used in the ME-SIMS analysis of the different phospholipids. a) Signal intensity was insufficient to determine the mass resolution. b) No spatially resolved data is presented. c) Concentration of PI in the sample was 40  $\mu$ M in a saturated solution of ferulic acid in 1:1 water: acetonitrile.

diluted such that the same amount of phospholipid molecules as in the ME-SIMS experiments was deposited on the silicon substrate in a 1-2  $\mu$ l droplet.

## 5.2.2 Mass spectrometry and imaging

All static SIMS experiments were performed on a Physical Electronics (Eden Prairie, MN) TRIFT-II Time-of-Flight SIMS (TOF-SIMS) equipped with an  $^{115}\text{In}^+$  liquid metal ion gun.<sup>70, 71</sup> The TRIFT is a stigmatic imaging time-of-flight analyzer incorporating a 2 m flight path and three quasi-hemispherical electrostatic sector analyzers (ESAs) as an integral part of the TOF analyzer. These ESAs compensate the differences in ion flight times due to variations in the secondary ion's initial kinetic energies and ion emission angles. The secondary ions were extracted through a 3.2 kV electric field into the TOF analyzer and post-accelerated by an additional 5 kV prior to detection on a dual multichannel plate phosphor screen detector. A multistop time-to-digital converter with 138 ps time resolution was used to acquire the detector signals. For each chemical image, the primary beam was scanned over a  $100 \times 100 \mu\text{m}$  sample area, divided into  $256 \times 256$  pixels. For each ion detected, the mass (time-of-flight) and primary beam position were recorded (RAW-file format); this allowed post-processing of the data. For example, the region-of-interest (ROI) analysis frequently used in this study, allows mass spectra to be obtained from a user-defined part of the original sampled area only.

All experiments were performed with a primary ion beam current of 450 pA. The other experimental parameters, the resulting mass and spatial resolutions are detailed in Table 5.1. The mass resolution is to a large extent determined by the primary ion beam pulse length at the sample. By compressing the primary ion pulse (bunching) ion packages of approximately 1 ns

at the sample were obtained. An unbunched beam is typically used to record with high spatial detail. The spatial resolution at the specified primary beam settings was determined from a 25  $\mu\text{m}$  copper grid on an aluminum substrate. The experimental conditions were chosen such that for all experiments the ion dose was between  $10^{11}$  and  $10^{12}$  ions per  $\text{cm}^2$  (see Table 5.1), ensuring analyses in the static SIMS regime. The longer primary ion pulse length, in the positive mode analysis of PG, only served to shorten the analysis time at similar ion dosage.

The positive ion mode mass spectra and chemical images were recorded on the same  $100\ \mu\text{m} \times 100\ \mu\text{m}$  areas within the sample. The chemical images were compared to optical images of the corresponding sample areas. These optical images were recorded either before analysis using a Leica DMRX light microscope in reflection mode combined with a Donpisha XC-003P CCD camera or during analysis using the TRIFT's light microscope.

Fragmentation of PG and PE was studied in electrospray ionisation<sup>119</sup> Fourier transform ion cyclotron resonance (ESI-FTICR) tandem mass spectrometry<sup>120</sup> experiments performed on a modified Bruker-Spectrospin (Fällanden, Swiss) APEX 7.0e FTICR equipped with a 7 Tesla superconducting magnet. The complete system has been described in detail before.<sup>121, 122</sup> MALDI experiments were performed on a Bruker Biflex MALDI-TOF equipped with a nitrogen laser.

## 5.3 Results and discussion

### 5.3.1 Phosphatidylcholine

In Figure 5.1A a positive ion mode ME-SIMS spectrum of 2,5-DHB matrix crystals containing PC is shown. In positive mode the predominant high mass ion was the  $[\text{M} + \text{H}]^+$  ion at  $m/z$  760.6, where M refers to the neutral, zwitterionic form of PC. Intense signals due to the pseudo-molecular ions of  $[\text{M} + \text{Na}]^+$  ( $m/z$  782.5) and  $[\text{M} + \text{K}]^+$  ( $m/z$  798.5) were detected, as well as clear signals from the PC dimers at  $m/z$  1520 ( $[2\text{M} + \text{H}]^+$ ) and 1542 ( $[2\text{M} + \text{Na}]^+$ ) (see inset Figure 5.1A). The  $[\text{M} + \text{H}]^+$  and  $[\text{M} + \text{Na}]^+$  pseudo-molecular ions were also observed without the addition of matrix to the sample. In either method of sample preparation, one of the most intense PC peaks was that of the phosphocholine headgroup at  $m/z$  184.1 (inset Figure 5.1A). However, the intensity of the  $[\text{M} + \text{H}]^+$  ion relative to that of the phosphocholine headgroup fragment ion evidently favored ME-SIMS, 0.16 as opposed to 0.03 for SIMS without matrix. Clearly, the addition of matrix softened the ionization conditions for the analyte molecules. The spectral features obtained in ME-SIMS of PC show great similarity to those observed in a positive ion mode MALDI study on phospholipids by Harvey.<sup>116</sup> There it was reported that the main fragmentation involved cleavage in the direct vicinity of the phosphate oxygen atoms. Its main products were observed here as well: the  $m/z$  184.1 phosphocholine headgroup, choline ( $[\text{C}_5\text{H}_{12}\text{N}]^+$ ) at  $m/z$  86.1 (not shown) and a

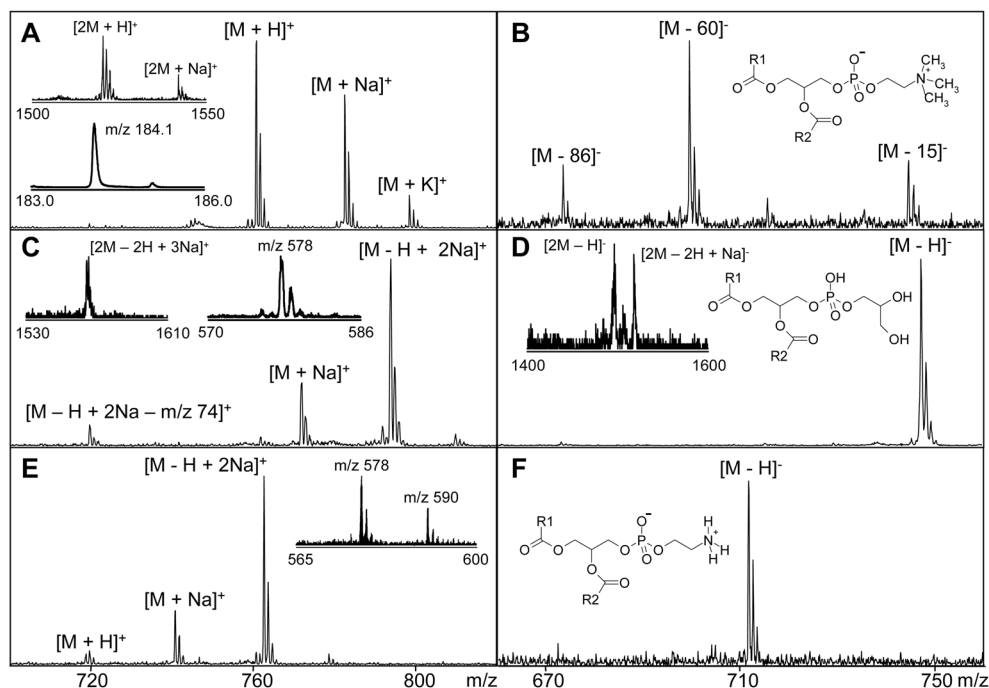


**Figure 5.1.** Molecular mass region of ME-SIMS spectra, in positive and negative ion mode, of (A) PC (pos.), (B) PC (neg.), (C) PG (pos.), (D) PG (neg.), (E) PE (pos.), (F) PE (neg.). Intense fragments and dimers are included in the insets. The molecular structures show the neutral form of the phospholipids. The R1 and R2 groups resemble the hydrocarbon tail of the palmitate and oleate acyl groups.

diacylglycerol acylium (DAG) ion, resulting from the loss of the phosphocholine headgroup, at  $m/z$  578 (not shown).

In negative ion mode the only high mass species detected corresponded to the PC fragments:  $[M - 15]^-$ ,  $[M - 60]^-$  and  $[M - 86]^-$  (see Figure 5.1B). Similar results have been reported using fast-atom-bombardment (FAB) ionization.<sup>123</sup> In the lower mass region of the spectrum carboxylate anions corresponding to the substituents at the sn-1 and sn-2 positions in PC(16:0, 18:1) were detected at  $m/z$  255 (palmitate) and 281 (oleate), respectively (not shown).

The positive ion mode PC spectrum in Figure 5.1A was obtained from the  $100 \mu\text{m} \times 100 \mu\text{m}$  sample area displayed in the optical image of Figure 5.2A. It is evident that the prepared sample was highly heterogeneous. Three distinct regions were present: a large translucent crystal situated in the upper left part of the image, several dark crystals at the bottom and right-hand-side and finally regions where no crystal was deposited, here the silicon substrate is visible. The positive ion mode PC mass spectrum of Figure 5.1A includes all counts from the

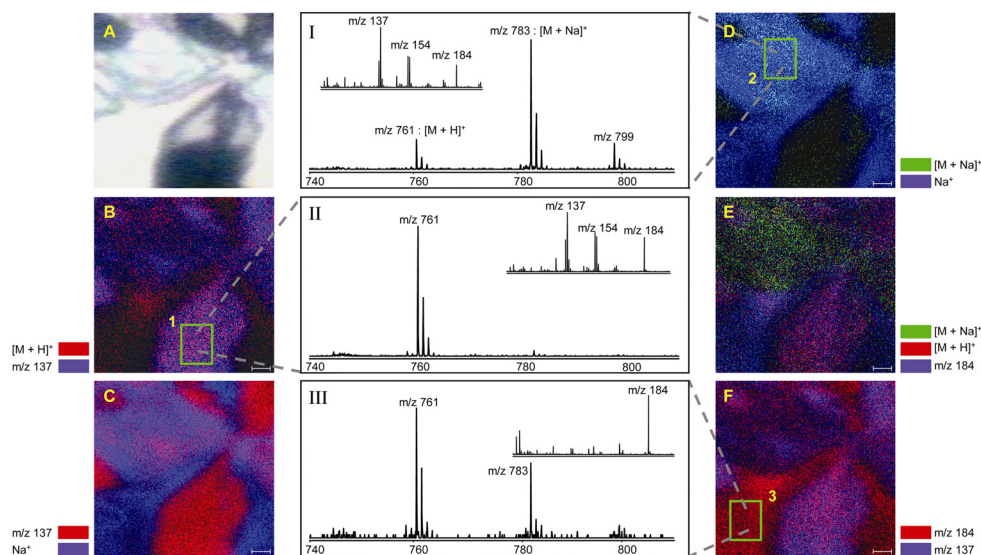


**Figure 5.2** (A) Optical image of the 100 μm × 100 μm PC-2,5-DHB sample area, used to obtain the chemical images: (B) – (F). The chemical images show the distributions of sodium, matrix, the phosphocholine headgroup, [M + H]<sup>+</sup> and [M + Na]<sup>+</sup> peaks across the sample area. The mass spectra I – III result from ROI analyses of the regions highlighted in (B), (D) and (F).

three different areas. The high-resolution chemical imaging approach allowed the non-uniformities and corresponding variations in signal intensities over the sample to be studied. The ion specific chemical images of Figures 5.2.B – F show that different molecular and fragment ions were obtained from the three distinct regions visible in Figure 5.2A.

From the first chemical image (5.2B) the dark crystals were identified as matrix crystals (the blue region is a map of the 2,5-DHB m/z 137 fragment). In the same image, the matrix signal is overlaid with the image corresponding to the distribution of the protonated pseudo-molecular ions at m/z 761 (red). It is clear that the counts due to [M + H]<sup>+</sup> coincide with the region of high matrix counts. Hanton *et al.*<sup>55</sup> described the segregation of sodium from 2,5-DHB crystals. This effect is clearly demonstrated in image 5.2C (sodium ions in blue, matrix counts in red). The translucent features show a more mixed character. From these regions both sodium and matrix counts were detected; these conditions favor the formation of the PC sodium adduct, [M + Na]<sup>+</sup> (image 5.2D). Spectra 2.I-III resulted from region-of-interest (ROI) analyses; the spectra were constructed from regions with equal areas (15 μm × 18 μm) indicated in the images 5.2B, 5.2D and 5.2F, respectively. As expected from the chemical images there is a substantial difference between the spectra 5.2I and 5.2II, corresponding to a region of high matrix content and a region showing both sodium and matrix counts, respectively. They support the earlier observation that protonated pseudo-molecular ions were generated from the matrix-dominated region, while the sodiated ones

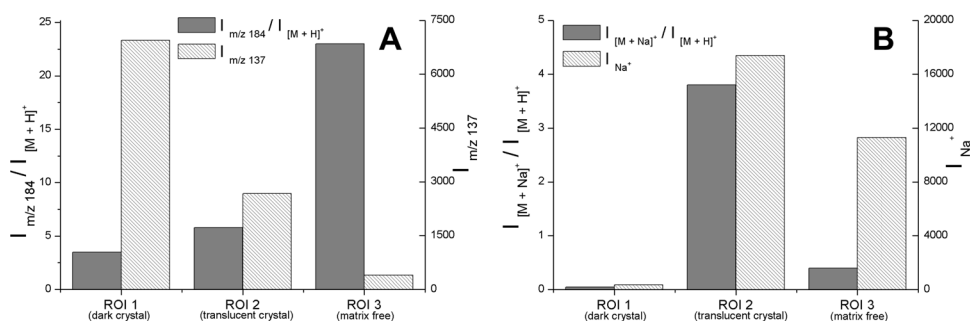


**Figure 5.3** Histograms of the ROI's indicated in Figure 5.2 showing (A) the intensity ratios of the  $m/z$  184 fragment to protonated pseudo-molecular ions of PC, in combination with the matrix signal intensity, (B) intensity ratios of the sodiated over the protonated pseudo-molecular species of PC, together with the sodium signal.

stem from those areas that show both sodium and matrix counts. The intensity of the sodiated matrix ion signal ( $m/z$  177) was also enhanced in the translucent crystal area. The  $[2M + H]^+$  ( $m/z$  1520) ion was only observed from the dark crystal areas. Image 5.2F shows the distribution of the phosphocholine headgroup fragment ions ( $m/z$  184) in red and the matrix in blue, it is readily observable that from the region where no matrix crystals were formed a large number of fragment counts were detected. This implies that during the process of drying not all of the PC was incorporated in the matrix crystals. From ROI mass spectrum 5.2III it is evident that  $[M + H]^+$  ions ( $m/z$  761) were also produced from the matrix free region. However, the portion of fragment ions was much greater. The ratios of intensities of the phosphocholine headgroup ion to its precursor, the  $[M + H]^+$  ion (see below), for the three ROIs indicated in Figure 5.2 are shown in Figure 5.3A together with the corresponding  $m/z$  137 (2,5-DHB) intensities. It is clear that the presence of the matrix reduced fragmentation and therefore enhanced the yield of molecular ions of PC. This effect is most pronounced for the dark crystal region (ROI 1) indicating that also the amount of matrix material is important. The ratio of phosphocholine headgroup to  $[M + H]^+$  was studied in a MALDI analysis of PC as well. It was found to vary largely with laser power, but in general the degree of fragmentation was significantly lower (data not shown). In Figure 5.3B the  $[M + Na]^+$  to  $[M + H]^+$  ratio is shown together with the  $Na^+$  signal. It is clear that the presence of both sodium and matrix in the translucent crystal area is required for the formation of sodiated pseudo-molecular ions.

Collisional activation studies on the PC  $[M + H]^+$  ion yielded only one significant product ion, namely the phosphocholine headgroup ion at  $m/z$  184.<sup>124</sup> Similar studies on the  $[M + Na]^+$  precursor have revealed a more complicated fragmentation scheme.<sup>125, 126</sup> Although the phosphocholine headgroup ion has never been observed as a fragment from the  $[M + Na]^+$  precursor, Domingues *et al.*<sup>126</sup> have shown that collisional activation of the  $[M + Na]^+$  ion can result in a different fragment ion at  $m/z$  184. However, no clear evidence for the presence of

$[M + Na]^+$  decomposition products in the ME-SIMS spectra were found. Therefore it is believed that the  $m/z$  184 signal observed here is solely due to the phosphocholine headgroup. This is in accordance with the observation from image 5.2E, from which it is clear that the  $m/z$  184 signal showed least intensity in those regions that produced abundant sodiated molecular ions.

### 5.3.2 Phosphatidylglycerol

In contrast to the ME-SIMS results of PC, sodiated species dominated the molecular ion mass region of the PG positive ion mode spectrum. The  $[M + H]^+$  ion of PG was not observed. In the molecular mass region of Figure 5.1C, signals due to the sodium and potassium containing salts of PG,  $[M - H + 2Na]^+$  at  $m/z$  794 and  $[M - H + Na + K]^+$  at  $m/z$  810 respectively, were identified. Opposed to the results obtained for PC, the molecular structure of PG allows the binding of two sodium ions. The number of sodium ions found to bind to PC, PG and PE (see next section), respectively, in this ME-SIMS study agrees with results from MALDI studies by Harvey<sup>116</sup>. There it was shown that methylation of the phosphate group in PC prevents the formation of a PC  $[M - H + 2Na]^+$  species. Presumably, the binding of the second  $Na^+$  to PG involves the glycerol part of the headgroup, since this is the only part where it differs from PC. The mass peak at  $m/z$  772 was identified as  $[M + Na]^+$ . The only dimer observed was the  $[2(M - H + Na) + Na]^+$  ion. The peak at  $m/z$  720 corresponds to the loss of  $C_3H_6O_2$  from the sodiated sodium salt. This neutral loss, part of the glycerol headgroup, has been reported for CAD of the PG  $[M - H]^-$  ion<sup>127</sup>, the anionic part of the sodium salt detected here. Constant Neutral Loss (CNL) scans of  $m/z$  172, corresponding to the loss of the total glycerophosphate headgroup, are often used to identify PG in lipid mixtures.<sup>128, 129</sup> In this respect the signal detected at  $m/z$  578 could be due to the diglyceride ion formed from the  $[M + H]^+$  ion upon neutral loss of the glycerophosphate headgroup, although the precursor was not detected. This is in agreement with the observation made before that the  $m/z$  172 CNL scans are only successful when the precursor ion is the  $[M + H]^+$  ion, since sodium adducts do not easily fragment by losing the neutral headgroup.<sup>129</sup> Below, it is shown how the additional spatial information acquired in imaging ME-SIMS helped to determine the origin of the  $m/z$  578 fragment.

The molecular region of the negative ion mode spectrum was dominated by the  $[M - H]^-$  peak at  $m/z$  748. Additionally, two types of dimeric species could be detected at  $m/z$  1496 and 1518, which correspond to the molecular dimer,  $[2M - H]^-$ , and the sodiated dimer  $[2M - 2H + Na]^-$  respectively (Figure 5.1D).

ME-SIMS of PG greatly resembled MALDI results obtained by Harvey<sup>116</sup> as well as in our lab. SIMS analysis of the PG sample without matrix did not result in significant intact pseudo-molecular ion signal in either positive or negative ion mode. The negative ion mode spectra were fully dominated by the carboxylate anions corresponding to the palmitic and oleic fatty acid residues.



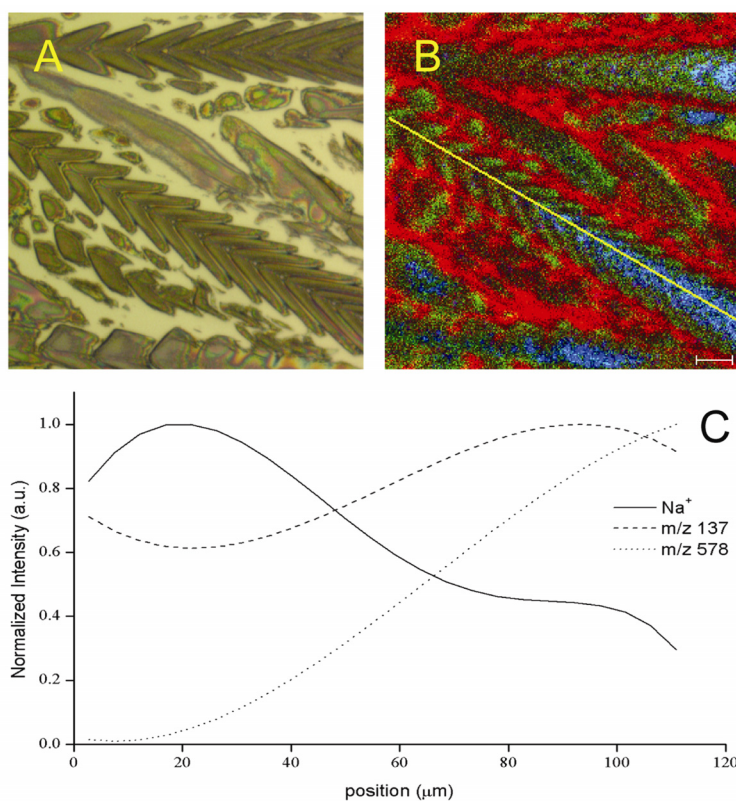


**Figure 5.4** (A) An optical image (500 times magnification) of the studied  $100\ \mu\text{m} \times 100\ \mu\text{m}$  PG-2,5-DHB sample area. (B) Chemical image showing the distributions of sodium (red), matrix (green) and the m/z 578 fragment (blue) across the sample. (C) Their pixel intensities along the line indicated in (B) fitted to a polynomial function to visualize their trends.

In Figure 5.4A an optical image is shown of the sample area from which the positive ion mode mass spectrum of Figure 5.1C was obtained. The crystals formed are visibly different from those observed with PC. In image 5.4B the distribution of sodium (red), matrix (green) and DAG fragment ions (blue) are shown. Segregation of sodium from the matrix crystals was apparent. Nevertheless, sodium was present throughout all crystal features in the sample area studied in detail here, but the intensity of the signal varied considerably (image 5.4B). These conditions allowed the sodium adducts / salts of PG to be generated from all crystal sites. In general the more bulky crystals on the sample showed greater degree of segregation. In Figure 5.4C the intensity gradients of Na<sup>+</sup>, m/z 137 and m/z 578 along the line indicated in Figure 5.4B are displayed. The lines in the figure result from a best fit of a polynomial function of to the pixel intensity data to clarify the trend present in the data. It becomes clear from this graph

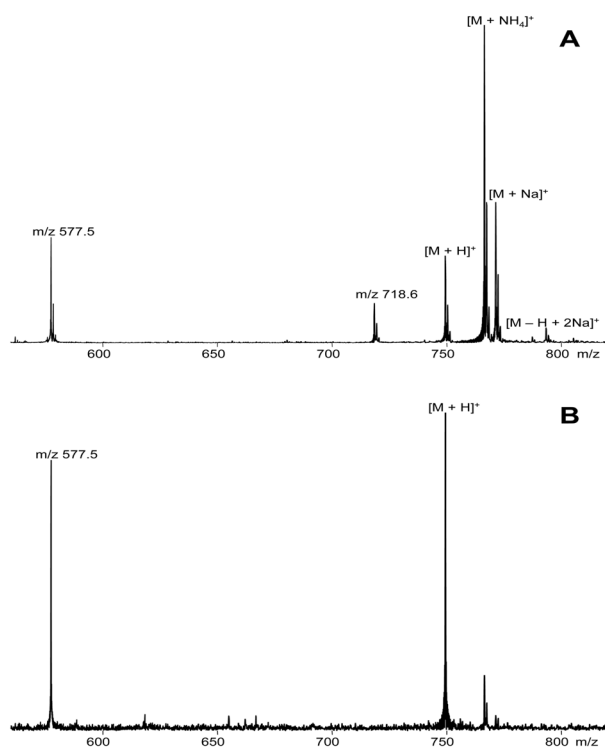


Figure 5.5 (A) ESI-FTICR mass spectra of PG. (B) Result of on-resonance CAD of the isolated  $[M + H]^+$  ion.

that the amount of sodium present in the crystal structure decreases when going from upper left to bottom right of the chain of crystals, as the crystals become larger. At the same time the  $m/z$  578 and the  $m/z$  137 matrix signals follow an opposite trend. These observations suggest that in the lower right part of this crystal structure the local physico-chemical conditions approach those of the dark crystals in the case of PC (Figure 5.2A) which allowed the formation of  $[M + H]^+$  ions. The exclusion of the  $m/z$  578 fragment ion from the areas of high sodium signal in combination with the established understanding that the 2,5-DHB MALDI matrix acts as a proton donor strongly suggests that it is formed from the unimolecular decay of protonated PG.

An ESI-FTICR tandem mass spectrometry study was performed to further investigate the fragmentation behavior of PG's pseudo-molecular ions. All positive mode pseudo-molecular ions observed in ME-SIMS were seen in ESI as well (Figure 5.5A). Although, PG was obtained as an ammonium salt, no ammoniated pseudo-molecular ions were observed in either ME-SIMS (see Figure 5.1C) or MALDI (results not shown) of the PG sample. In contrast ESI did yield the  $[M + NH_4]^+$  ion. The pseudo-molecular mono-isotopic species were isolated in the

ICR cell using a SWIFT pulse.<sup>130</sup> Subsequently, the isolated ions were fragmented using either on-resonance excitation or sustained off-resonance irradiation (SORI) collision activated dissociation (CAD). It was found that both the  $[M + H]^+$  (Figure 5.5B) and the  $[M + NH_4]^+$  ions of PG gave significant yields of the DAG fragment. The fragmentation of these ions was relatively facile. Already after exciting the trapped ions to a few eV kinetic energy significant fragmentation, resulting in the DAG ion, was observed. Low energy CAD of the sodium adducts did NOT result in the formation of this fragment. These findings further support the hypothesis stated before; the DAG fragment is very efficiently formed by unimolecular decay of the protonated PG. The observed segregation of salts from the crystals make it very unlikely that the  $m/z$  578 ion observed in ME-SIMS is formed from unimolecular decay of the ammoniated precursor.

In general  $[M - H]^-$  ions were only observed from matrix crystal areas low in sodium counts.

### 5.3.3 Phosphatidylethanolamine

In positive ion mode several different pseudo-molecular ions of PE were detected. The  $[M + H]^+$  ion was seen at  $m/z$  719 (Figure 5.1E). The peaks at  $m/z$  763 and 779 were assigned to the sodiated and potassiated sodium salts of PE,  $[M - H + 2Na]^+$  and  $[M - H + Na + K]^+$ , respectively. The ion detected at  $m/z$  741 corresponds to the  $[M + Na]^+$  ion. As expected the ratio of protonated to the sodiated species varied with the local amount of sodium present in the sample, relatively more intense protonated peaks were observed as well. A dimer of PE,  $[2(M - H + Na) + Na]^+$ , was detected at  $m/z$  1503 (not shown). The intense peak at  $m/z$  578 is the result from the DAG ion that is formed upon loss of the polar headgroup. As was the case for PG the ion specific images of the PE sample helped to identify its precursor ion (see below). The identity of the ion detected at  $m/z$  590 is still unknown. In ME-SIMS measurements of PE with ferulic acid as matrix the  $m/z$  590 ion was not observed, nor was it observed in ESI-FTICR analysis of the PE sample used in the ME-SIMS experiments.

The negative ion mode ME-SIMS of PE showed pronounced signal due to  $[M - H]^-$  at  $m/z$  717, no dimers were detected. Although static SIMS analysis of the PE sample did yield significant molecular ion signal in both positive and negative mode ion mode, the fact that dimers were detected only using ME-SIMS points to the softer desorption/ionization conditions in ME-SIMS.

The features present in the light microscope image (Figure 5.6A) of the  $100\ \mu\text{m} \times 100\ \mu\text{m}$  area of the PE-2,5-DHB sample studied here, closely resemble the ones observed for PC (see Figure 5.2A). The sample region contained dark crystals, translucent crystals as well as regions free of crystals. In Figure 5.6B the distributions of sodium (blue) and matrix (red) are compared. In agreement with the results for the PC sample, segregation of sodium from the more bulky 2,5-DHB crystals was manifest, the translucent crystals produced significant sodium and matrix counts, and the crystal free regions showed intense sodium signals.

In the chemical image of Figure 5.6C the distribution of the sodiated species,  $[M + Na]^+$  and  $[M - H + 2Na]^+$ , and the diglyceride fragment ion at  $m/z$  578 are shown in green, red and blue,

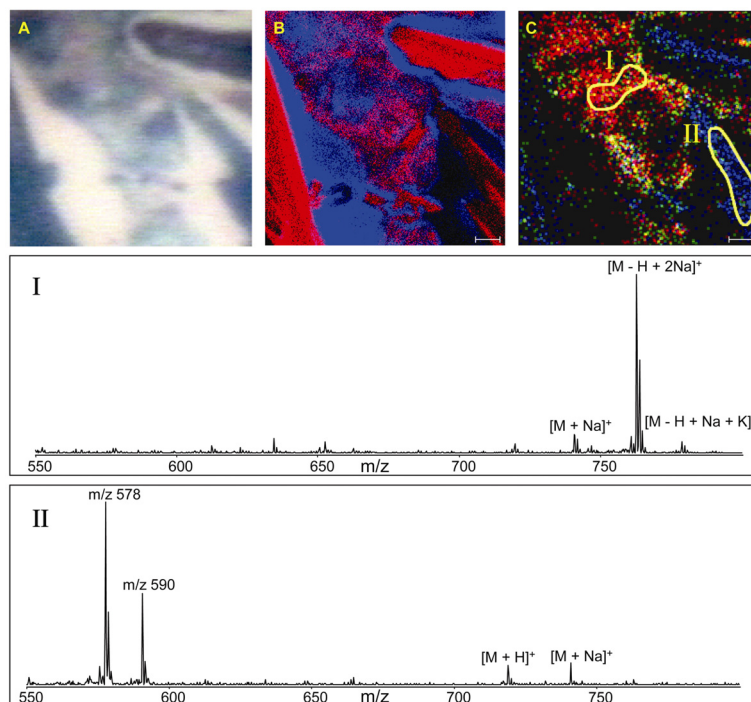


**Figure 5.6** (A) Optical image of a  $100\ \mu\text{m} \times 100\ \mu\text{m}$  area of the PE-2,5-DHB sample. The chemical images show the distributions of sodium (blue) and matrix (red) (B),  $[M + \text{Na}]^+$ ,  $[M - \text{H} + 2\text{Na}]^+$  (red) and  $m/z\ 578$  (blue) (C) over the sample area. The mass spectra I and II, result from ROI analyses on the regions highlighted in (C).

respectively. To improve the clarity of the image, a three-by-three pixel summation function of the raw data was performed, which increased the pixel size to approximately  $1.5\ \mu\text{m}$ . As can be seen these high mass PE ions were generated from distinctively different regions within the sample area. While the  $m/z\ 578$  diglyceride ion completely originated from the bulky matrix crystals (compare Figure 5.6B and C, respectively), both sodium adducts were generated from the translucent features. The differences in the signals obtained from these areas are emphasized by the ROI spectra shown in 6.I and 6.II, which were generated from the highlighted areas in Figure 5.6C. The  $m/z\ 578$  ion can be formed upon loss of the ethanolamine headgroup ( $m/z\ 141$ ) from  $[M + \text{H}]^+$  or from  $[M + \text{Na}]^+$  upon loss of the ethanolamine headgroup sodium salt ( $m/z\ 163$ ).<sup>125</sup> The clear spatial separation of the  $m/z\ 578$  fragment from the sodium containing pseudo-molecular ions indicates that the former is the case here. Furthermore, ESI-FTICR tandem mass spectrometry demonstrated that the formation of the diglyceride ion from the PE  $[M + \text{H}]^+$  precursor is a facile process. This was also apparent from MALDI-FTICR results by Marto *et al.*<sup>131</sup> Closer inspection of Figures 5.6B

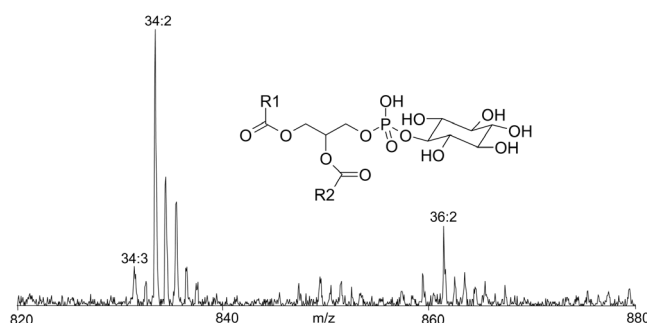


**Figure 5.7** The molecular mass region of the negative ion mode ME-SIMS spectrum of PI with ferulic acid. The structure represents the neutral species of PI.

and C even shows that the  $[M + Na]^+$  ion is most abundant from the regions within the translucent crystal which show relatively intense  $m/z$  137 signal while the  $[M - H + 2Na]^+$  originates from the regions where the sodium counts clearly dominate. In contrast to the data shown for PC no high mass PE related ions were detected from the matrix free region, which points to improved incorporation into the matrix crystals.

The predominant molecular ion found in the negative mode,  $[M - H]^-$  was found to originate from the matrix crystals, which had undergone complete segregation of sodium.

### 5.3.4 Phosphatidylinositol

Although both the  $[M - H]^-$  and the  $[M + Na]^+$  ions could be detected with 2,5-DHB as matrix, the use of ferulic acid as a matrix yielded superior spectra in the negative ion mode. Figure 5.7 shows the negative ion mode high  $m/z$  part of the ME-SIMS spectrum of PI with ferulic acid. The PI sample contained a distribution of different fatty acid chain lengths and degrees of saturation. The main contribution to the spectrum comes from the species characterized by 34:2 (number of C atom:number of unsaturations) at  $m/z$  833 ( $[M - H]^-$ ). Also contributions from 34:3, 34:1 and 34:0 as well as 36:3, 36:2, 36:1 and 36:0 could be clearly distinguished. The inositol phosphate group at  $m/z$  259 (not shown) and fragments resulting from fatty acid losses were observed as well. The largest detected PI species was the adduct:  $[M + \text{ferulic acid} - H]^-$  at  $m/z$  1028 (not shown). The yield of molecular species of PI was significantly lower compared to the other three phospholipids studied.

## 5.4 Conclusions

In agreement with other studies<sup>54, 113</sup>, the results presented here demonstrate that the incorporation of an analyte in a matrix crystal softens the SIMS ionization process and thereby enhances the yield for larger pseudo-molecular ions. Intense signals of intact molecular ions of PC, PG, PE and PI were obtained in this study with ME-SIMS. The observation of dimers further demonstrated the softness of the ionization technique. The observed pseudo-molecular species resemble those obtained with MALDI in an other study<sup>116</sup> as well as in our lab. This finding indicates that although SIMS is a more surface sensitive technique, the results obtained here apply to MALDI as well.

It has been recognized before that the MALDI dried droplet sample preparation method produces highly non-uniform matrix crystals.<sup>87</sup> Owing to the size of the laser focus in MALDI multiple crystals are sampled in each laser shot. The obtained signal is the summed total of all the signals from the different crystals and the contributions from different crystal sites cannot be separated. The high spatial resolution of SIMS facilitated a detailed investigation of the samples formed by dried-droplet deposition, beyond the resolution limits of imaging MALDI. The chemically different domains within the sample were captured in  $100\ \mu\text{m} \times 100\ \mu\text{m}$  images. Based on the detected intensities of  $\text{Na}^+$  and matrix signals, three distinct features were identified: matrix crystals free of sodium, crystal types demonstrating a mixed sodium-matrix character and regions free of matrix (and high in sodium). Varying desorption/ionization efficiency introduced by chemically different domains is thought to be an important factor in the frequently observed MALDI 'hot' or 'sweet' spot phenomenon.

The microscopically different regions identified in the sample yielded different molecular ions and different degrees of fragmentation. Sodium adducts of the phospholipids were only detected from regions on the sample where both sodium and matrix were present in significant amounts. Pseudo-molecular ions of PG and PE were obtained with up to two sodium ions attached, while PC can accommodate only one. Presumably, the stable charge on the quaternary nitrogen atom prevents further sodium association. PC  $[\text{M} + \text{H}]^+$  signals were obtained from DHB crystals from which sodium was efficiently segregated. Equivalent PE and PG containing crystals resulted in little or no  $[\text{M} + \text{H}]^+$  ions, instead abundant signal due to the  $m/z$  578 DAG fragment ion was recorded. The chemical images corresponding to these crystals, supported by ESI-FTICR tandem mass spectrometry results showed that this fragment must result from the efficient unimolecular decay of the PE and PG protonated pseudo-molecular species. The different degrees of fragmentation of the protonated pseudo-molecular ions of PC, PG and PE ( $\text{PC} \ll \text{PE} < \text{PG}$ ) reflect their different dissociation threshold energies. In this respect a thermometer molecule investigation<sup>132</sup> of ME-SIMS could be used to further characterize internal energy deposition and the effect of the matrix in ME-SIMS (see Chapter 6 of this thesis).

The variation in the molecular ion yield observed here will complicate the interpretation of spatial information obtained using any matrix-based chemical imaging technique. These chemical biases have to be understood and overcome (or bypassed) in order to obtain high

spatial resolution chemical images that reflect the distribution of the analyte in biological samples. Clearly, the information obtained from high spatial resolution SIMS analysis of matrix crystals will contribute herein and will provide additional insight into matrix assisted desorption/ionization processes.

#### Additional note:

The effects of locally varying sample conditions on microscopic scale are largely circumvented when ESD of the matrix-analyte sample is used. In this type of sample preparation the sample is covered with a spray of tiny matrix droplets. The resulting sample preparations are homogeneous on microscopic scale. Moreover, the mass resolution is significantly improved because height differences in the sample preparation, which affect the ions' flight times and introduce distortion of the extraction field, are prevented.<sup>92</sup> Recently, distributions of intact phospholipids were recorded in a follow up ME-SIMS study of the surface of neuroblastoma cells covered by matrix crystals through ESD. The downside of the ESD sample preparation method is the reduced wetting of the sample, which reduces the extraction of analytes and thereby sensitivity.





# Fragmentation at and above surfaces in SIMS: effects of biomolecular yield enhancing surface modifications

Matrix-enhanced SIMS and metal-assisted SIMS are successfully employed to increase the organic ion yield in SIMS. In this study we compare kinetic energy distributions obtained for SIMS, ME-SIMS and MetA-SIMS sputtering of molecular ions. In comparison to the SIMS kinetic energy distributions, those obtained for ME-SIMS display larger energy deficits, indicative of entrainment of analyte ions by matrix molecules or collisions taking place above the sample surface. In the case of MetA-SIMS high energy broadening of the distributions is observed, resulting from the high stopping power of the gold used. A selection of substituted benzyropyridinium salts is used to investigate the effect of internal energy reduction in ME-SIMS. Kinetic energy distributions were used to separate the daughter ions formed in the sample region from those resulting from unimolecular decay on nanosecond timescales, in the first tens of micrometers above the sample surface. The longer-timescale decay was monitored by changing the energy acceptance window of the mass spectrometer used. From the decay rate constants internal energies of the precursor ions decaying on nanosecond timescales were determined using RRKM theory. Within the framework of the precursor model the results indicate an extension of the collision cascade over a wider area than in SIMS.

## 6.1 Introduction

The analysis of the biochemical content of cells is an exciting and challenging application for secondary ion mass spectrometry (SIMS). The chemical specificity combined with the high lateral resolution (typically a few hundred nanometers) imaging SIMS is capable of, make it a very valuable addition to the palette of experimental tools available in life sciences.

Over the past years many reports have appeared on the elemental analysis of biological samples using dynamic SIMS.<sup>106, 107, 133</sup> The high ion doses used induce extensive fragmentation of all organic molecules present in the sample. Therefore the insights obtained are limited to the (distributions of) elements and small organic fragments only, all molecular information is lost. In static SIMS much lower ion doses are used, therefore it is better suited for the analysis of organic samples. Although fragmentation is still extensive, small intact molecules like cholesterol and informative fragments like the phosphocholine-headgroup can readily be detected.<sup>63, 65, 134</sup> Despite, the successes in the mapping of elements and small organics, one of the key factors that is limiting the wide scale application of SIMS to biological systems is the low ionization yield for biomolecules.<sup>135</sup>

Currently, several strategies to improve the ionization yields of molecular species are explored. It has been shown that the use of polyatomic primary ion beams like  $\text{SF}_5^+$ ,  $\text{C}_{60}^+$ ,  $\text{Au}_n^+$  and  $\text{Bi}_n^{m+}$  greatly enhances the ionization yields of small organic species compared to mono-atomic primary ions like  $\text{Ga}^+$  and  $\text{In}^+$ .<sup>40, 41, 136</sup> However, reports on the analysis of real world samples using polyatomic primary ion beams are still limited, yielding mainly cholesterol and phospholipid (-fragment) signals.<sup>137</sup> A recent publication has shown that the application of polyatomic primary ions is promising for the analysis of small peptides from combinatorial libraries.<sup>62</sup> Besides innovations on the nature of the primary ion projectile, sensitivity enhancing effects of sample preparation are investigated as well. Sample metallization (or metal assisted-SIMS (MetA-SIMS)) and matrix-enhanced SIMS (ME-SIMS) belong to this latter category. Sample metallization as a means to improve organic molecular ion yields was introduced by Linton *et al.*<sup>138</sup> Recently, it was shown that by evaporating a minute layer of gold or silver onto organic samples among which polyalanine and polystyrene the ionization yields and efficiencies of the molecular ions were significantly improved, by at least an order of magnitude.<sup>50</sup> The enhancing effects in MetA-SIMS are not limited to the formation of metal-cationized pseudo-molecular ions; the yield of protonated ions is improved as well. Migration of organic species on to formed gold islands in combination with the increased stopping power of gold are likely explanations for the sensitivity enhancement.<sup>49, 50</sup> In this way the application of an overlayer of gold or silver is comparable to the use of a gold or silver substrate, with the sample applied in a thin layer.<sup>52</sup> MetA-SIMS studies of tissue demonstrate that distributions of small biomolecules such as cholesterol ( $m/z$  385) can be imaged effectively in this way.<sup>67, 139</sup> Higher mass signals (800 – 1300  $m/z$ ) have been used to image different regions of single neuroblastoma cells.<sup>67</sup> The sensitivity enhancing effect of the presence of a matrix in which labile analyte ions are embedded has been known for a longer period. Reduction of fragmentation in the presence of a solid matrix was recognized already in the 80's of the past century.<sup>140</sup> Recently, following the

success of MALDI<sup>3, 4</sup>, the dissolution of the analyte compounds in a matrix has received renewed attention. Wu *et al.*<sup>54</sup> adopted the MALDI sample preparation protocol to record mass spectra of proteins with masses larger than 10 kDa. In these ME-SIMS experiments a dried-droplet sample preparation protocol was followed. As was shown in a recent publication<sup>89</sup>, this results in an inhomogeneous sample, with locally varying ionization conditions. This kind of sample preparation is not favorable in an imaging experiment. For ME-SIMS imaging experiments on biological systems electrospray deposition (ESD) of the matrix is better suited. The first ME-SIMS imaging results using ESD have been published recently. In this study biomolecules from the nervous tissue of the pond snail *Lymnaea stagnalis* were mapped with 2.6  $\mu\text{m}$  lateral resolution.<sup>66</sup> The molecular ion yield enhancement that is provided by the matrix in ME-SIMS has been attributed to several factors, which resemble the function of the matrix in MALDI. The presence of the matrix promotes molecular ion yields through ionization enhancement and fragmentation reduction. The acidic nature of the MALDI matrix promotes the formation of  $[\text{M} + \text{H}]^+$  ions through proton donation.<sup>54</sup> The isolation of the analyte molecules by the matrix promotes desorption of large molecules through disentanglement of long molecular chains.<sup>35</sup> The lower degree of fragmentation in ME-SIMS has been observed on several occasions.<sup>54, 89, 112</sup> It has been attributed to a nestle environment for the analyte molecules provided by the solid matrix<sup>54</sup> and internal energy reduction through the desolvation of collectively desorbed matrix-analyte clusters. In MetA-SIMS reduced fragmentation has been observed as well.<sup>112</sup>

In this study we have used a group of substituted benzylpyridinium (BPY) salts to investigate the reduction of fragmentation in ME-SIMS. The benzylpyridinium salts are so-called thermometer molecules; upon activation they undergo a simple C – N cleavage (Figure 6.1), the activation energies of the different BPY precursor ions are known from quantum – chemical calculations and vary with the identity of the substituted side-group (second column Table 6.1).<sup>141</sup> Moreover they are preformed ions in solution; if we assume that the BPYs retain this charge state in solid crystal state charge transfer can be excluded to play a role in any observed molecular ionization yield enhancement. In addition, since the size of the BPY precursor ions is comparable to the organic matrix molecules used in this study (2,5-dihydroxy benzoic acid) the mentioned isolation effect is eliminated as well. We have determined precursor ion yields and kinetic energy distributions (KEDs) for the BPY daughter and precursor ions. In this study a time-of-flight mass spectrometer equipped with electrostatic

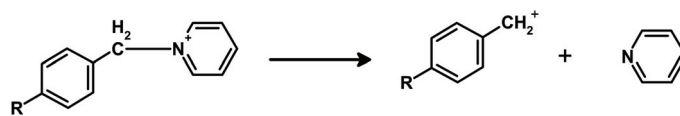


**Figure 6.1** Unimolecular decay of a *para*-substituted benzyl pyridinium precursor ion by cleavage of the C – N bond. The activation energy for the reaction is dependent on the identity of the R-group.

R	$E_a$ (eV)	Precursor ion mass (Da)	Extraction Potential (V)	$t_{ESA1}$ ( $\mu$ s)
<i>p</i> -OCH <sub>3</sub>	1.55	200	4600	11.4
<i>p</i> -Cl	2.04	204	4550	11.6
<i>p</i> -F	2.05	188	4675	10.9
<i>p</i> -CN	2.38	195	4675	11.1

**Table 6.1** Activation energies of the different BPY variants. The ions' masses and the extraction potentials were used in the SIMION simulations (see text). The daughter ions' masses are 79 Da lower.  $t_{ESA1}$  is the precursor ion flight time until the entrance of the first ESA. The flight times were determined using SIMION.

analyzers was used. The formation of BPY daughter ions was recorded at different instances along the ions' flight paths. In the acceleration region, in-sample formation of daughter ions was separated from nanosecond-timescale decay reactions taking place just above the sample surface. From the daughter ions' KEDs the associated decay rate constants were determined. The ions that decay at these early times make up the high internal energy tail of the sputtered precursor ion distributions. Rice-Ramsperger-Kassel-Marcus (RRKM) theory was used to estimate average internal energies of these rapidly decaying ions. Under normal operation conditions the BPY precursor ions decaying on  $\mu$ s-timescales are not observed. This is due to the limited energy acceptance window of the mass spectrometer used. A method is presented to analyze these metastable ions. KEDs of peptide ions formed through the addition of H<sup>+</sup> or Na<sup>+</sup> and of the BPY preformed ions are compared. Furthermore, we have started a study on MetA-SIMS; first KED results are included as well. We have related our findings from the SIMS, ME- and MetA-SIMS KEDs to results from molecular dynamics simulations of the SIMS sputtering process of organic samples.<sup>35, 36</sup> The observed decay of the precursor ions is discussed within the framework of Benninghoven's precursor model<sup>142</sup>, which describes the dissipation of energy in the collision cascade around the point of impact of the primary ion.

## 6.2 Experimental section

### 6.2.1 Sample preparation

In this study we used a variety of samples and sample preparation methodologies. The thin layer samples were prepared by deposition of a 10  $\mu$ l droplet of the solution containing the analyte onto a Si-wafer, which was then spin-coated for 1 minute at 4000 rpm. The goldcoated

samples were prepared by depositing a 10  $\mu\text{l}$  droplet on a Si wafer, which was allowed to dry. Subsequently, a 1 nm gold layer was applied using a Quorum Technologies (Newhaven, East Sussex, U.K.) SC7640 Sputter Coater. The ESD samples were obtained by premixing the analyte and matrix solutions to a 1:2000 molar ratio. The matrix used in this study was 2,5-dihydroxy benzoic acid (2,5-DHB). The matrix-analyte mixture was then applied to a Si-wafer by ESD, using a home-built electrospray device<sup>66</sup>. The spray needle was kept at 4 kV, while the sample plate was grounded. The flow rate of the sprayed solution was set at 6  $\mu\text{l}$  per hour, the spray was allowed to continue for approximately 40 minutes. A series of substituted benzylpyridinium and a small peptide (Leucine Enkephalin) were used as analytes in this study. The 2,5-DHB and the peptides were all purchased from Sigma-Aldrich (Germany). The benzylpyridinium salts used in this study are all *para*-substituted forms: *para*-chloro (*p*-Cl), *para*-fluoro (*p*-F), *para*-methoxy (*p*-OCH<sub>3</sub>) and *para*-cyano (*p*-CN). The activation energies of the BPY precursor ions used are included in Table 6.1. The benzylpyridinium salts solutions (10<sup>-4</sup> M, acetonitrile:water 1:1 v/v) were prepared at Liège University.

### 6.2.2. Mass spectrometry

All experiments described in this work were performed on a Physical Electronics (Eden Prairie, MN) TRIFT-II Time-of-Flight SIMS (TOF-SIMS)<sup>70, 71</sup> equipped with an <sup>115</sup>In<sup>+</sup> liquid metal ion gun. The spectra and KEDs were obtained using 15 keV primary ions (impact energy  $\sim$  12 keV) in 12 ns long ion bunches of 1.5 nA dc ion current, which were compressed to 1 ns ion packages at the sample. Secondary ions were extracted through a 3 kV electric field into the TOF analyzer and post-accelerated by an additional 6 kV prior to detection on a dual multichannel plate phosphor screen detector. A multistop time-to-digital converter with 138 ps time resolution was used to acquire the detector signals. Mass resolution is optimized through time-focusing of the secondary ions using three hemispherical electrostatic sector analyzers (ESAs). For analysis of the fragmentation products formed in the field free region of the mass spectrometer different source conditions were used (Section 6.3).

### 6.2.3 Kinetic energy distributions

Kinetic Energy Distributions (KEDs) are a valuable tool to experimentally study the fundamentals of the sputtering process. The KEDs give insight in the kinetic energy of the sputtered species, besides, characteristics of the formation and decay processes of the generated ions can be derived from observed energy deficits from the accelerating field energy (see below). The KEDs shown in this work were obtained in a way very similar as described before by Delcorte *et al.*<sup>143</sup> In short: the TRIFT ToF-mass spectrometer ion optics were tuned such that the secondary ions were maximally dispersed according to their kinetic energy just in front of the second ESA (Section 2.4.3). By moving a slit into the flight paths of the secondary

ions, only the ions of a well-defined kinetic energy were allowed to pass. The width of the slit determines the energy resolution of the experiment. For this purpose we designed an adjustable slit, capable of slit widths between 50  $\mu\text{m}$  and 2 mm, which can be moved in and out of the secondary ion pathways. All experiments described here were performed with the slit width set at 100  $\mu\text{m}$ , corresponding to a 1.7 eV energy passband. The energy filter was stepped through the secondary ion pathways to record ion intensities at different kinetic energies resulting in KEDs. The translational step size of the filter was varied for different parts of the KED; the smallest step size was 20  $\mu\text{m}$  resulting in oversampling of the distribution to obtain high quality data. In order to prevent sample degradation a fresh sample area was targeted for every position of the energy slit. Multiple KED curves were averaged to minimize the effects of sample variation. The zero-kinetic energy point was determined from the KEDs recorded for atomic ions. It was taken as the crossing of the tangent of the decaying slope on the low energy side of the KED with the translation axis.

### 6.3 Decay rate constants: theoretical and experimental considerations

On an instrument that is equipped with ESAs, like the TRIFT, precursor ions that fragment during their flight are largely not detected. This due to the limited kinetic energy acceptance window of the ESAs. The energy acceptance window under normal operation conditions was experimentally determined at 160 eV and the largest energy deficit that is still accepted at 80 eV. Upon decay of a precursor ion its kinetic energy is partitioned over the ionic fragment and neutral loss according to their respective masses. The kinetic energy of the daughter ions formed in the field free region, having acquired the full acceleration energy, follows from:

$$\frac{\Delta M}{M} \cdot \frac{E_k}{\Delta E_k} = 1 \quad (6.1)$$

where  $M$  and  $\Delta M$  are the masses of the precursor ion and the neutral loss respectively and  $E_k$  and  $\Delta E_k$  their kinetic energies. For a precursor ion of mass 200 Da (*p*-OCH<sub>3</sub>), a neutral loss of 79 Da (Pyridine) and an extraction potential of 3 kV, the daughter ions would have an energy deficit of 119 eV and would not be detected. If the decay takes place in the acceleration region the precursor ions have not received their full acceleration yet. The location above the sample surface where the decay takes place determines the energy deficit from the accelerating field energy. Using equations 6.II and 6.III (Section 6.3.1) it can be shown that for the BPY precursor-daughter ion pairs only the daughter ions formed within the first 160  $\mu\text{m}$  or 20 ns of their flight are detected. Figure 6.2 illustrates the areas of the TRIFT mass spectrometer where daughter ion formation can be monitored.

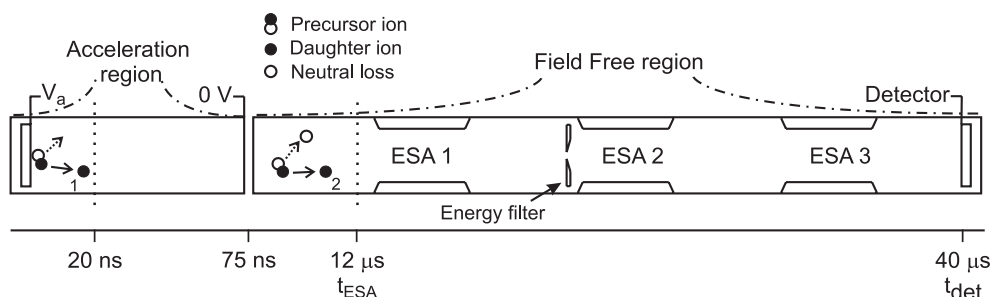


**Figure 6.2** A schematic representation of the TRIFT ToF mass spectrometer. The acceleration region and the field free drift region are indicated, immersion and transfer lenses are not included. The energy filter is located just in front of the second ESA. The axis below the schematics indicates the precursor ion flight time (or reaction time) at different stages. The daughter ion (1) that is formed from unimolecular decay in the acceleration region, taking place within the first 20 ns of its flight, is detected under normal operation conditions. Its rate of formation is estimated from the energy deficit part of its KED. The daughter ion (2), which is formed between the immersion lens and the entrance of the first ESA, is detected under elevated  $V_a$  conditions.

### 6.3.1 Unimolecular dissociation in the acceleration region

The daughter ions observed in the SIMS mass spectrum arise from decay reactions taking place above the sample surface and from in-sample fragmentation. Ions formed above the sample surface will experience an energy deficit from the full acceleration energy; they will appear at negative apparent kinetic energy (KE) in the KED. The ratio between the areas under the negative and positive apparent kinetic energy parts of the KED curve can be used to separate these two contributions to the total daughter ion intensity.

The rate constant for the nanosecond timescale decay of BPY precursor ions can be obtained from the energy deficit part of daughter ion KED. The energy deficit ( $E_d$ ) is related to the position of fragmentation ( $x_d$ ) by:

$$E_d = \frac{e \cdot V_a \cdot \Delta M}{d \cdot M} \cdot x_d \quad (6.II)$$

where  $d$  is the length of the acceleration region ( $d = 2.1 \text{ mm}$ ),  $V_a$  is the acceleration potential,  $e$  the elemental charge,  $M$  and  $\Delta M$  are the mass of the precursor and the neutral loss, respectively. The time and position of fragmentation are related through the equations of motion of the precursor ions in the acceleration region. Therefore, the time of fragmentation can be expressed in terms of the energy deficit:

$$\tau_f = C \cdot \sqrt{E_d} \quad (6.III)$$

Chapter 6

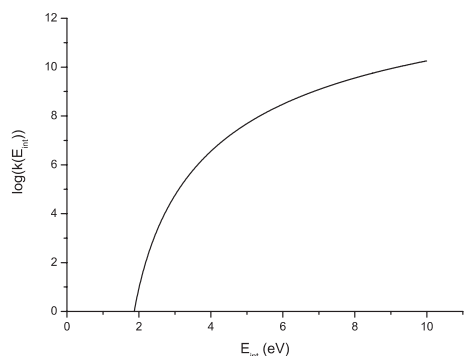


**Figure 6.3** An example of a decay rate versus internal energy curve calculated according to RRKM theory. This particular curve was calculated for the *p*-OCH<sub>3</sub> substituted BPY.

$$\text{with } C = \frac{M \cdot d}{e \cdot V_a} \cdot \sqrt{\frac{2}{\Delta M}} \quad (6.IV)$$

A daughter ion KED is constructed of the daughter ion intensity ( $I_f$ ) within an energy window around a given apparent KE, plotted against the apparent KE. In other words it corresponds to  $\Delta I_f / \Delta E_k$ , where  $E_k$  denotes the apparent kinetic energy (KE). From the theory on unimolecular decay the time derivative of the daughter ion intensity is known to be:

$$\frac{dI_f}{dt} = k \cdot I_0 e^{-kt} \quad (6.V)$$

which is related to the experimentally obtained quantity through:

$$\frac{\Delta I_f}{\Delta E_d} \approx \frac{dI_f}{dE_d} = \frac{dI_f}{dt} \cdot \frac{dt}{dE_d} \quad (6.VI)$$

Combination of 6.III – 6.V gives:

$$\frac{dI_f}{dE_d} = \frac{k_a \cdot I_0 \cdot C}{2 \cdot \sqrt{E_d}} \cdot e^{-k_a \cdot C \cdot \sqrt{E_d}} \quad (6.VII)$$

After integration over  $dE_d$ :

$$I_f(E_d) = I_0 \cdot (1 - e^{-k_a \cdot C \cdot \sqrt{E_d}}) \quad (6.VIII)$$

from which the decay rate constant ( $k_a$ ) is obtained from a fit to a mono-exponential function. The decay rate constant that is obtained in this way is used to estimate the average internal



energy of the ions in the high internal energy tail of the sputtered precursor ion distribution. For this purpose the theoretical dependence of the rate constants on the internal energy was calculated according to RRKM theory using MassKinetics Scientific Demo software.<sup>141, 144</sup> Figure 6.3 contains an example of a rate constant versus internal energy curve.

### 6.3.2 Unimolecular dissociation in the field free region

The metastable BPY precursor ions that decay on microsecond timescales are not observed in the mass spectrum under standard experimental conditions. In order to study the slow metastable decay of the BPY ions the kinetic energy of their fragment ions has to be moved into the energy acceptance window of the mass spectrometer. Increasing the accelerating field and leaving the ESAs set for the acceptance of 3 keV ions achieves this. The extraction potentials used to accomplish this for the different BPYs are listed in Table 6.1. The ions that have not decayed when they reach the first ESA will collide with the electrodes because of their high kinetic energy. SIMION simulations of the whole TRIFT mass spectrometer for metastable ions that decay in the field free region between the extraction plate and the first ESA spectrometer were performed at ULVAC-PHI. These simulations demonstrate that our approach to study metastable decay in the TRIFT is feasible. Figure 6.4 contains the simulated ion trajectory for an  $m/z$  188 ion ( $p$ -F), which decays 5  $\mu$ s after it had been sputtered of the surface. The  $m/z$  109 daughter ion reaches the detector, the settings used in the simulation are indicated on the right in the figure. The immersion lens is tuned for operation at high extraction potential while the transfer lens and ESAs are set for the normal extraction voltage. From the simulations it was found that ions that fragment inside the transfer lens are not detected (Figure 6.5). In Table 6.1 the time interval during which metastable daughter ions become traceable using the described method is included.

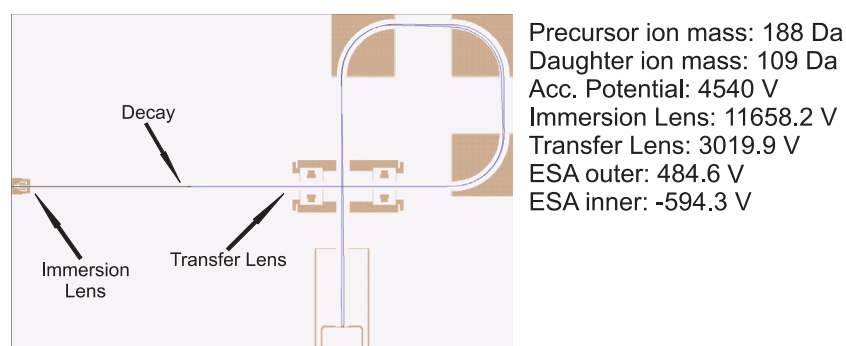


**Figure 6.4** The decay of  $p$ -F ( $m/z$  188) precursor ions 5  $\mu$ s after sputtering, the settings on the right guarantee transmission of the  $m/z$  109 daughter ion.

## Chapter 6

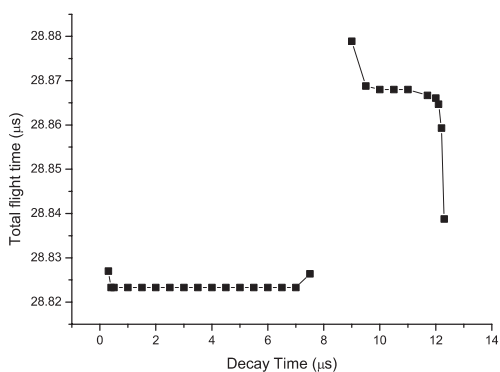


**Figure 6.5** Relation between the full daughter ion flight time and the instant of fragmentation. The gap in the curve corresponds to decay taking place inside the transfer lens (Figure 2.5), which results in a blind spot in the analysis of daughter ion formation.

## 6.4 Results

### 6.4.1. Mass spectra

The mass spectra obtained for the BPY salt samples were dominated in the ‘high mass’ region by the precursor ( $\text{Py}^+\text{F}$ ) and daughter ( $\text{F}^+$ ) ions produced through C - N bond scission, accompanied by 2,5-DHB related peaks for the ESD samples. As pointed out in the previous sections the daughter ions observed in the mass spectrum of a standard SIMS, ME-SIMS or Meta-SIMS experiment are produced in the sample region or just above it. Besides the precursor-daughter ion pair also mass peaks that are indicative of hydrogen or  $\text{H}_2$  loss were observed. These ions were formed in the sample region / source region and partly from metastable decay in the field free drift region. As the mass difference from the precursor ion is very small, ions produced from hydrogen loss in the field free spectrometer region can be detected (Eq. 6.I). Small, non-specific organic fragments from the matrix and BPY species dominate the low mass region of the spectrum. These fragments are produced through energetic collisions taking place in the dense region of the collision cascade surrounding the position of impact of the primary ion.

### 6.4.2 Ion yields

The ion yield ( $Y$ ) for a specific ion is defined as the number of detected secondary ions per primary ion. In Table 6.2 the ion yields that were determined for the BPY samples prepared according to the ESD and thin layer protocol are shown. Especially, for the thin layer samples the spread in ion yields is very limited. It is apparent that the presence of the DHB matrix

R	$Y_{\text{SIMS}}$ ( $10^{-9}$ )	$Y_{\text{ME-SIMS}}$ ( $10^{-9}$ )	$Y_{\text{ME-SIMS}}/Y_{\text{SIMS}}$
<i>p</i> -OCH <sub>3</sub>	3.5	4.2	1.2
<i>p</i> -Cl	6	86.1	14.4
<i>p</i> -F	13.2	95.7	7.3
<i>p</i> -CN	6.7	17.6	2.6

**Table 6.2** Ion yields in SIMS and ME-SIMS for the different BPY precursor ions. The last column shows the yield enhancement.

results in higher ion yields for all the BPY species studied. The yield enhancement factor, included in the last column, varies between 1.2 and 14.4. This variation in yield enhancement, depending on the analyte of interest has been observed before in ME-SIMS.<sup>26</sup>

### 6.4.3 Kinetic energy distributions

#### 6.4.3.1 Thin layer sample

The KEDs obtained from the thin layer sample for the different benzylpyridinium salts studied are very similar. All distributions have their maximum around 1.2 eV and have a FWHM of approximately 2 eV. The fragment and precursor distributions are very similar. As an example in Figure 6.6A distributions of the precursor and fragment ions of the *p*-F substituted BPY salt are shown. For a good comparison of the distributions they are normalized on their maximum intensities. In Figure 6.6B the normalized distributions are plotted on a logarithmic scale. From this latter representation it becomes clear that the greatest differences between the distributions are in the region of negative apparent kinetic energies. While in this region the precursor distribution quickly falls off the fragment distribution follows a much slower decay. An apparent negative kinetic energy is indicative of an energy deficit from the accelerating field energy, which can find its origin in several processes. First of all the ions might have been formed above the sample surface, through gas-phase reactions in a desorption plume or through evaporation from a micro-droplet or cluster, both of these processes are often used to describe ion formation in matrix-assisted laser desorption / ionization (MALDI)<sup>3, 4</sup>. Secondly, collisions in the desorption plume above the sample surface can result in a reduction of the ion's kinetic energy. Since for the very low ion doses used in SIMS only very little material is sputtered in each cycle of the experiment it is very unlikely that gas-phase collisions and therefore also gas-phase reactions will induce any observable effects. Finally, the ion can be formed upon fragmentation from its precursor, the precursor's translational energy will then be distributed proportionally over the resulting ionic and neutral fragment species. Since the

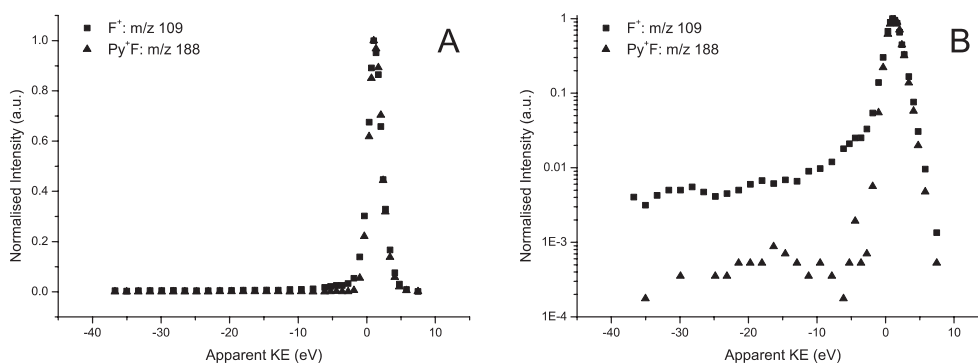


**Figure 6.6** Normalized KEDs of the precursor and daughter ions of the *p*-F BPY for a thin layer sample (**A**) shown for linear scales and (**B**) for logarithmic intensity scale to stress the observed differences. The daughter ion distribution is extended to negative apparent energies. The ions observed at negative apparent energies result from metastable decay in acceleration region above the sample surface.

benzylpyridinium ions are preformed and only the fragment ions display the energy deficit it is obvious that the observed effect is predominantly a consequence of decay in the source region.

#### 6.4.3.2 ESD sample

The energy slit is used to detect differences in the kinetic energy of ions with respect to the full acceleration field energy. Therefore it is crucial that the ions experience a constant accelerating field during the experiments; any effects of charging of the sample should be avoided. Sample charging is not expected to be a problem for the thin layer sample preparations, though when non-conductive samples like matrix crystal layers are studied it can be of significance. The ESD method was chosen to deposit the matrix-analyte mixture because it produces very homogeneous, thin layers of crystals. However, taking into account the non-conductive character of the matrix crystal layer, distortions of the accelerating field are still likely to occur. To investigate the distorting effect on the KEDs, we monitored their evolution in time, during the course of an experiment. A change in the accelerating potential due to charging of the sample will shift the KED peak position with time. Time-resolved KED (3D-KED) plots were calculated from RAW-files. In this file format intensity data, and flight times are stored in equal size data blocks, each block was provided with an acquisition time stamp. In this way the time resolution obtained in the 3D-KED is dependent on the signal intensity: high signal intensity fills up the data blocks relatively fast, resulting in relatively short time interval between subsequent time stamps. In this way the highest time resolution was obtained for the high intensity part of the KED. This made that for an interval of 4 eV around the peak position a time resolution of 250 ms was obtained. The 3D-KED plot for the

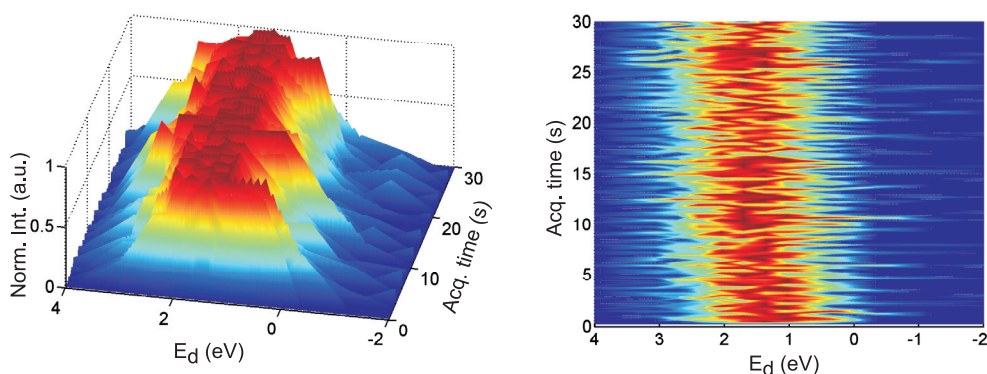


**Figure 6.7** Time resolved kinetic energy distributions for an ESD sample of the *p*-OCH<sub>3</sub> BPY precursor ion. In the first ten seconds only a slight shift in the location of the maximum intensity is observed. Therefore it is concluded that charging of the sample does not interfere with recording of KEDs on ESD samples.

*p*-OCH<sub>3</sub> BPY precursor is shown in Figure 6.7. Only a slight charging effect is observed during the first ten seconds of the experiment. The total effect is below 0.5 eV, which falls within our energy slit resolution. Therefore it is concluded that this phenomenon will only have a marginal effect on the KEDs of ions created from an ESD matrix-analyte sample.

As for the case of the matrix-free samples the KEDs recorded for the different BPY salts demonstrated similar features. The distributions peak between 1.8 and 3 eV with an FWHM of approximately 3 eV. Figure 6.8 contains the precursor and daughter ions KEDs obtained in a ME-SIMS experiment for the *p*-CN benzylpyridinium salt. Close examination of the curves

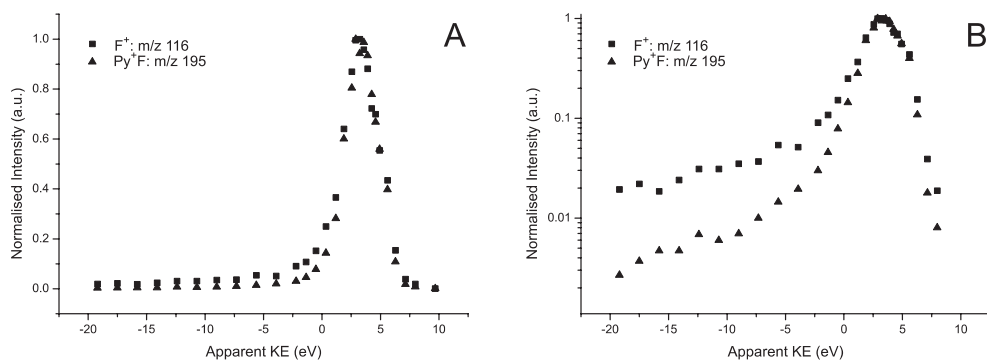


**Figure 6.8** Normalized KEDs of precursor and daughter ion pair of the *p*-CN substituted BPY obtained for an ESD sample (A) on linear scales, (B) on logarithmic intensity scale. For the ESD sample the precursor ion KED shows significant intensity at negative apparent KE, most likely this is caused by clustering with matrix molecules.

tells us that the KED of the fragment ion is broadened towards the positive kinetic energy side with respect to that of the precursor. The positive KE part of the distribution comprises of ions that have gained KE in the collision cascade. Broadening of fragment distributions has been observed before.<sup>143</sup> Since, the precursor ions that are most likely to undergo fragmentation are the ones with the highest internal energy, the depletion of the high kinetic energy side of the precursor KED indicates that the ions that gain the most kinetic energy ( $\sim 4 - 5$  eV) during the desorption process also receive a large amount of internal energy. In comparison to the matrix-free case the fall off of the fragment ion distribution with increasing energy deficit is less rapid, which is indicative of a slower decay rate. The precursor ion KED also displays some intensity at low energy deficits. To illustrate the heterogeneous nature of the broadening of the precursor distribution (only to the negative apparent KE side) in comparison to the matrix free situation we shifted the precursor KEDs, obtained for the *p*-F substituted BP in SIMS and ME-SIMS respectively, to make the peak positions overlap (see Figure 6.9). It is apparent that in the presence of 2,5-DHB the precursor distribution is broadened to the low (negative) apparent KE side only. Height differences in the sample can also be a source of broadening, though these would result in broadening on the positive as well as on the negative apparent KE sides of the distribution. Since the BPYs are preformed ions the energy deficit can be explained by a MALDI-like entrainment of the precursor ions by the dominating matrix molecules. However, since the amount of material removed in an ME-SIMS experiment is greater than in a SIMS experiment collisions in the region just above the sample surface could also be a source of energy deficit. Comparison with the KED obtained for Leucine Enkephalin ions generated with MALDI (Figure 3.11) shows that far less collisions are involved or that association extends over a much smaller area. We can estimate the distance and timescale over which the association takes place from Eq. 6.II. The rapid fall off ( $\sim 2$ eV) of the precursor ion distribution with increasing energy deficit points to a very narrow ( $\leq 3 \mu\text{m}$ ) region above the sample surface, in which the BPY ions and organic matrix are associated. A

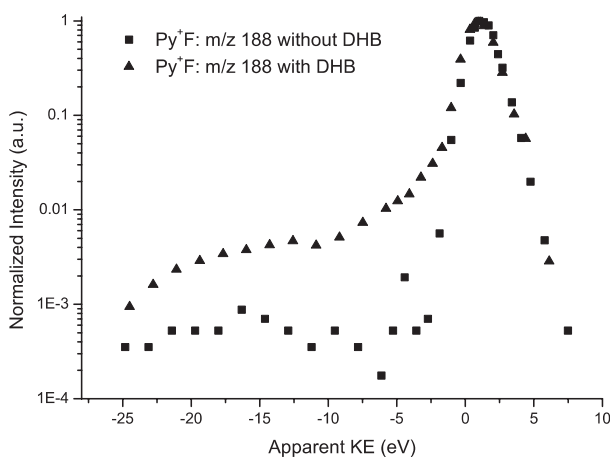
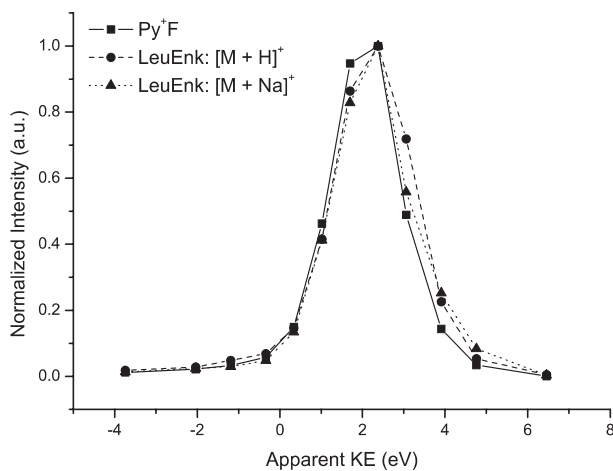


Figure 6.9 The differences in the KEDs of the *p*-F BPY variant recorded on the thin layer sample and ESD sample are limited to the energy deficit part of the distribution.



**Figure 6.10** KEDs of the precursor ion of the *p*-OCH<sub>3</sub> BPY and two pseudo-molecular ions of the peptide Leucine Enkephalin from an ESD sample. The addition reactions needed to form the pseudo-molecular peptide ions do not occur over an extended area. The higher kinetic side shows increased intensity for the peptide ions due to the increased degrees of freedom (see text).

recent molecular dynamics study<sup>35</sup> showed that entrainment of analytes in clusters of matrix molecules is likely at early times ( $\leq 100$  ps) in the desorption process. For the velocities of sputtered clusters which are predicted to lie in the range of 400 – 500 m/s<sup>35</sup> the energy deficit we observe here would require the analyte and matrix molecules to remain associated for times on the order of several nanoseconds. Comparison of the mass spectra / time traces recorded for the thin layer and ESD sample revealed a  $\sim 2$  ns broadening to longer flight times for the latter one. This is in line with the entrainment hypothesis.

Figure 6.10 shows KEDs that were recorded for an ESD sample containing both the *p*-OCH<sub>3</sub> - BPY and the small peptide Leucine Enkephalin. In order to detect the peptide a protonation or cationization reaction has to take place. Comparison of the energy deficit tails of the KEDs of the preformed BPY precursor ions and the quasi-molecular peptide ions should give insight in the localization of this addition reaction. The negative tails of the KEDs of the quasi-molecular peptide ions and the benzylpyridinium ion overlap. Therefore there is no reason to assume that the protonation or cationization occurs over an extended area above the sample surface. The broadening at the positive KE side of the peptide ion KED compared to the *m/z* 200 BPY precursor ion is a size effect. The Leucine Enkephalin fragmentation threshold energy is higher due to its many degrees of freedom; more internal energy can be stored in the molecule. As was seen before a large amount of vibrational excitation present in the molecule is an indication of high kinetic energy as well.

#### 6.4.3.3 Goldcoated sample

In general the KEDs obtained for the 1 nm goldcoated benzylpyridinium sample display similar characteristics as the ones obtained for the ESD matrix sample. The features that result from the unimolecular decay of the precursor ion are apparent. The main difference with the

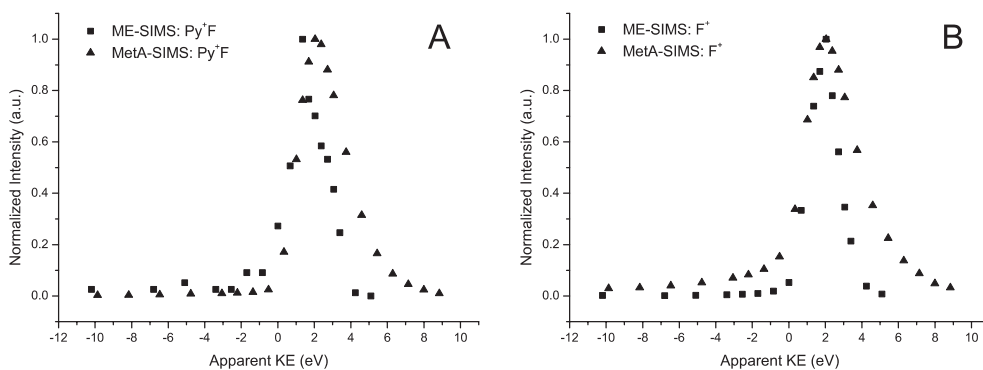


**Figure 6.11** Comparison of the MetA-SIMS and ME-SIMS KEDs for the *p*-OCH<sub>3</sub> BPY, (A) the precursor ions, (B) the daughter ions.

ESD sample case is in the width of the distributions. The KEDs obtained for the goldcoated sample are much wider, 2.5 - 3 eV versus 4 eV for the precursor ion in the ME-SIMS and gold-SIMS case respectively. This observation is illustrated in Figures 6.11A and B where the *p*-OCH<sub>3</sub> precursor and daughter ion KEDs for the two sample preparation techniques are compared. The broadening of the precursor ion KED predominantly takes place at the high kinetic energy side. It has been observed before that KEDs for gold covered organic samples can extend up to 10 eV KE.<sup>50</sup> In fact this behavior has been used to substantiate the similarities with thin layer organic samples on gold substrates. In molecular dynamics studies it has been shown that the correlated upward motion of multiple surface atoms can result in uplifting of an organic molecule from the surface, which is characterized by relatively low internal energy and high kinetic energy.<sup>52</sup> The daughter ion KED shows also significant broadening on the energy deficit side in the case of MetA-SIMS. This may point to lowering of the rate constant for the BPY decay in MetA-SIMS as compared to ME-SIMS. However, this still needs further investigation. It was not possible to efficiently sputter peptide ions from a goldcoated sample. Recently, it has been shown that the sputtering of peptide ions of metallic surfaces (gold or silver) is more successful.<sup>35, 145</sup>

#### 6.4.4 Decay rate constants, daughter ion formation and internal energies

##### 6.4.4.1 Daughter ion formation in the acceleration region

The rate constants for the fast decay of the BPY precursor ions in the source region of the instrument was deduced from the energy deficit part of the KED as detailed in the experimental section. With the substitution of 6.III, the mono-exponential growth function of equation 6.VIII is transferred to the time-domain. Figure 6.12 shows the result of the



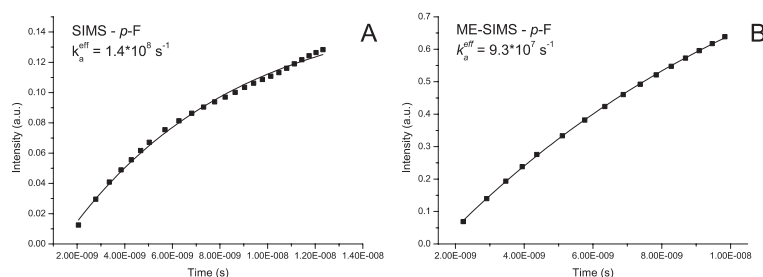


**Figure 6.12** The integrated energy deficit part of the KED of the daughter ions of the *p*-F BPY recorded in (A) SIMS and (B) ME-SIMS fit to a mono-exponential function.

integration, substitution and the subsequent fitting procedure. All the decay rate constants, obtained in this way are included in Table 6.3. As was seen in the previous section the precursor KEDs obtained for the ESD samples displayed some intensity at negative apparent energies, this was explained to arise from association of molecules / ions above the sample surface or from collisions. Most likely, daughter ions formed in the sample region will be involved in these processes as well. To evaluate this effect on  $k_a$  we subtracted the KED of the  $m/z$  154 molecular ion of 2,5-DHB from the daughter ion KED (normalized on total area) and subsequently determined the effective rate constant. Since no large effects were observed, the numbers in Table 6.3 are obtained directly from the daughter ion KED. The uncertainties in the values of  $k_a$  obtained from the fitting procedure are all within 10 % of numbers quoted. Therefore all rate constants except the ones for the *p*-F and *p*-Cl variants in the ME-SIMS case can be readily distinguished. The ME-SIMS rate constants display a clear relation with the activation energies (Table 6.1), the higher the activation energy the lower the rate constant. From the SIMS results such a relation is not clear. Although below the peculiar nature of the *p*-Cl substituted BPY ion will be discussed, the result obtained for the *p*-CN substituted one is clearly an outlier. The rate constants determined on the ESD samples are without exception lower than the ones obtained for the thin layer sample. The average internal energy values of the ions in the 'hot' tail of the precursor ion distribution was derived from rate constant versus internal energy curves as in Figure 6.3. The resulting energies are included in Table 6.3. We estimated the uncertainty in the internal energy values to be below 0.1 eV in all cases by projecting the uncertainty window around  $k_a$  onto the RRKM curve. Two observations can be made. First, the internal energy increases with higher activation energy and second the internal energies derived for ME-SIMS are without exception lower than for SIMS. The dependence of the internal energy values on the activation energy must result from an increased fragmentation in the sample region, at very early times ( $< 10^{-9}$  s). As a result the lower activation energy BPY-ion populations have cooled down more. This should also be reflected in the ratio between in-sample ( $I_i^{\text{in}}$ ) and above the sample fragmentation ( $I_i^{\text{out}}$ ). The ratios are derived from the daughter ion KEDs as explained in the experimental section and included in Table 6.3.

SIMS			
R	$k_a$ ( $s^{-1}$ )	$E_{int}$ (eV)	$I_f^a : I_f^s$
<i>p</i> -OCH <sub>3</sub>	$3 \cdot 10^8$	6.3	1 : 5.8
<i>p</i> -Cl	$1.3 \cdot 10^8$	7.2	1 : 4.5
<i>p</i> -F	$1.6 \cdot 10^8$	7.3	1 : 3.4
<i>p</i> -CN	$2.7 \cdot 10^8$	9.5	1 : 2.6
ME-SIMS			
R	$k_a$ ( $s^{-1}$ )	$E_{int}$ (eV)	$I_f^a : I_f^s$
<i>p</i> -OCH <sub>3</sub>	$1.4 \cdot 10^8$	5.8	1 : 5.0
<i>p</i> -Cl	$9.4 \cdot 10^7$	7.0	1 : 3.8
<i>p</i> -F	$9.3 \cdot 10^7$	7.0	1 : 2.8
<i>p</i> -CN	$6.6 \cdot 10^7$	8.4	1 : 4.6

**Table 6.3** The rate constants for the decay of the BPY precursor ions in the first part of the acceleration region. The  $E_{int}$  values indicate the average internal energy of the decaying precursor ions. The last column displays the ratio between the number of daughter ions produced in the sample surface and in the acceleration region above the surface.

All the  $I_f^a : I_f^s$  ratios except the *p*-CN results advocate an increase of the ratio with lower threshold energy. On average the ratios found are higher for SIMS than for ME-SIMS. This implies that besides the nature of the sample also the activation energy is an important factor for in-sample fragmentation.

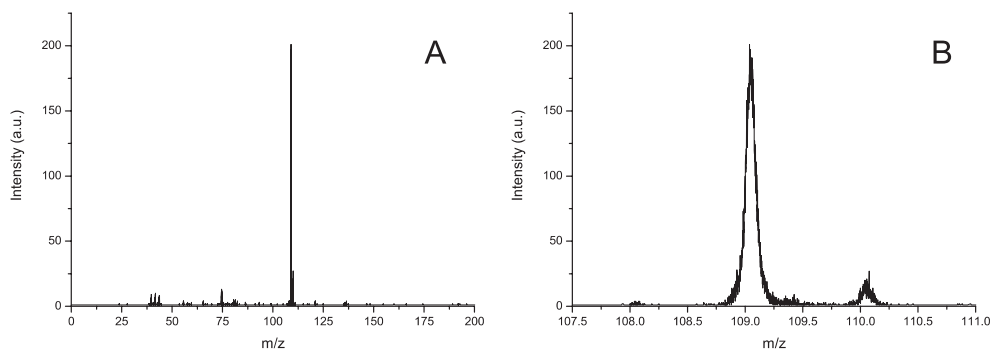


**Figure 6.13** (A) ME-SIMS metastable mass spectra of the *p*-F BPY daughter ion, (B) contains a close-up of the daughter ion region.

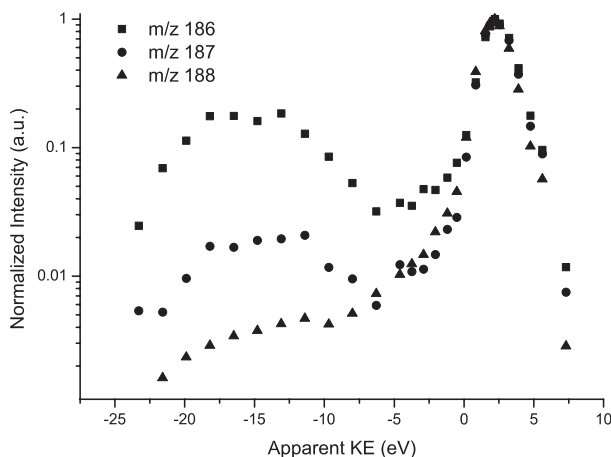


**Figure 6.14** KEDs for the *p*-F BPY precursor ions and two ions formed by the loss of one and two hydrogen atoms. From the location of the satellite peak the mass of the precursor ion can be determined according to equation 6.1 (see text).

#### 6.4.4.2 Daughter ion formation in the field free drift region

In Figure 6.13A a mass spectrum is shown that was obtained according to the protocol for the detection of metastable BPY ions decaying on  $\mu$ s-timescale, described in the section 6.3. The spectrum was recorded on an ESD sample containing the *p*-F BPY salt. It is clear that the spectrum is dominated by the daughter ion, the precursor ion ( $m/z$  188.09) is completely absent. Besides, some low signal intensity peaks are recorded at low  $m/z$  values. These most likely result from metastable decay of (hot) fragments formed in the sample region. They cannot be formed directly from the BPY precursor since the large mass difference would cause their kinetic energy to lie outside the acceptance window. Figure 6.13B contains a zoom of the daughter ion region. Although the mass peaks are broader than in a normal SIMS acquisition, the fact that the mass resolution is around 1500 ( $m/\Delta m$ ) indicates that the instrument's ESAs are still capable of time focusing the ions. Besides the outlined C - N scission another metastable decay mechanism was observed. In Figure 6.14 the KEDs of the *p*-F substituted BPY precursor ion and the ions produced by the loss of one and two hydrogen atoms respectively are shown. The satellite peaks in the KEDs indicate metastable decay in the drift region with relatively small neutral loss (equation 6.1). The energy deficits found for the  $m/z$  187 and the  $m/z$  186 ions match the loss of one hydrogen atom ( $\sim 15$  eV). For the loss of  $H_2$  an energy deficit of twice this value is required, which was not observed (not shown). Therefore it was concluded that the  $m/z$  186 ion is formed from two subsequent single hydrogen losses. To get an estimate of the fraction of the precursor ions, which decays according to this separate decay channel, the fragmentation, taking place in the source region and field free drift region was determined separately from the fragmentation taking place in the sample according to the method explained in the previous section. It was found that the

<b>SIMS – daughter ion formation</b>			
R	$I_f^s : I_P$	$I_f^a : I_P$	$I_{FF} : I_P$
<i>p</i> -OCH3	9	1.5	1.5 ± 0.1
<i>p</i> -Cl	2.2	0.48	0.38 ± 0.06
<i>p</i> -F	2.2	0.64	0.43 ± 0.04
<i>p</i> -CN	1.4	0.55	0.33 ± 0.05
<b>ME-SIMS – daughter ion formation</b>			
R	$I_f^s : I_P$	$I_f^a : I_P$	$I_{FF} : I_P$
<i>p</i> -OCH3	2.2	0.44	0.56 ± 0.03
<i>p</i> -Cl	0.30	0.08	0.21 ± 0.05
<i>p</i> -F	0.35	0.13	0.30 ± 0.06
<i>p</i> -CN	0.30	0.07	0.25 ± 0.02

**Table 6.4** The intensities of daughter ions formed at different instances in the mass spectrometer relative to the precursor ion intensity.  $I_f^s$  is the intensity of daughter ions formed in the surface region,  $I_f^a$  of those formed in the first 20 ns of the flight and  $I_{FF}$  those formed between 300 ns and approximately 11  $\mu$ s. An uncertainty of approximately 10 % was estimated in the values for  $I_f^s : I_P$  and  $I_f^a : I_P$ . To get to this estimate we assumed a 20 % uncertainty in the values of  $I_f^s$  and  $I_f^a$ .

C - N bond scission is by far the dominating pathway, approximately 5 % of total fragmentation involves hydrogen loss. The ratios of the intensities of the daughter ions formed in the field free drift region relative to the precursor ion intensity recorded under normal conditions are shown in the third and fourth column of Table 6.4. Only the result for *p*-Cl is not in line with the expected trend of lower ratio for lower activation energy. In a recent study that used benzylpyridinium ions to determine internal energy distributions in electrospray ionization the *para*-chloro substituted benzylpyridinium ion gave rise to a distribution that was clearly lower in energy than determined for other variants.<sup>141</sup> An explanation for this behavior might be that its actual threshold energy is higher than determined from quantum chemical calculations.

## 6.5 Discussion and conclusions

The daughter ions formed at different instances during the ion's flight through the mass spectrometer (Figure 6.2) have been determined. All daughter ion intensities obtained are

shown relative to the precursor ion intensity in Table 6.4. The fragmentation increases with decreasing activation energy as expected, except for *p*-Cl. At every instance in the mass spectrometer the fragmentation in ME-SIMS is relatively lower than in SIMS, which is indicative of a cooler population of precursor ions. From the fast decay in the acceleration region we were able to determine an average internal energy value for the hottest ions that have escaped the sample surface. It is clear that the internal energy of the ions produced in SIMS extends to higher values. Although we have not recorded all the daughter ions formed, from the values in Table 6.4 it can readily be seen that in ME-SIMS the number of daughter ions formed per detected precursor is approximately 4 times lower than in SIMS. The difference between the relative amounts of fragments is the largest for the decay taking place in the sample region and in the acceleration region. According to Benninghoven's precursor model the energy profile  $E(r)$  around the primary ion's impact point is described by a bell-shaped curve ( $\sim 1/r^2$ ). The nature of the species ejected at different distances from the impact point mirrors the local energy density.<sup>36</sup> From this respect the precursor and daughter ions that were created at different instances in the mass spectrometer (sample, source region and field free drift region) can be thought to result from rims located at different distances from the point-of-impact. The changes in relative ratios between the intact precursor ions and the daughter ions formed at different flight times indicate that the outer rim area, where intact ions are produced from should be relatively larger in the case of ME-SIMS. This is achieved when the decrease in energy density is less rapid for an ESD sample, resulting in the collision cascade extending over a wider area. The disappearance cross section, which is defined as the mono-exponential decay of the sputtered ion signal intensity with ion dose, is considered to be a good measure of the ejection radius of the sputtered ion.<sup>36</sup> Unpublished results on the disappearance cross-section of BPY ions with SIMS and ME-SIMS indicate a higher cross section for the latter methodology, which is in line with the above. Results from molecular simulations show that energy can indeed diffuse better through a matrix containing bulk sample.<sup>35</sup> The energy deficits observed in the KEDs of the BPY precursor and Leucine Enkephalin ions can be explained in terms of a MALDI like internal energy reduction mechanism: desolvation of matrix-analyte clusters in the gas-phase, as suggested by several authors.

Clearly, the reduced fragmentation observed in ME-SIMS cannot fully explain the increase in ionization yields, presented in this study (Table 6.2) as well as in other studies<sup>89, 112</sup>. Especially not since the analyte is present in 1:2000 ratio. The choice of BPY ions as analyte species excludes yield enhancing effects, like proton donation and analyte isolation to play an important role. Production of molecular ions from greater depths in the sample (as compared to the thin layer sample) will contribute to the higher molecular yield. Furthermore, segregation might concentrate the analyte ions in the near surface area<sup>114</sup>. Since SIMS analysis is limited to the first few monolayers of the sample, this would result in a lower matrix-to-analyte ratio for the part of the sample probed. An expanded area influenced by the collision cascade in ME-SIMS, as suggested here, does not only lead to a reduction of fragmentation but also to a larger amount of material being sputtered, which will increase the molecular ion yield further.

**Acknowledgement.** We would like to acknowledge Jean-François Greisch from the University of Liège (Mass Spectrometry Lab) for the preparation of the BPY samples, Hideo Iwai of ULVAC-PHI Inc. for the SIMION ion trajectory simulations and Laszlo Drahos from the Hungarian Academy of Sciences (Mass Spectrometry Department) for his help with the calculation of the RRKM curves.

# The molecular scanner in microscope mode

Here, we explore the combination of microscope mode imaging mass spectrometry with a protein identification methodology: the molecular scanner. It is found that in order to obtain high quality mass spectra and stigmatic ion images the application of a 5 nm gold layer is required. The molecular scanner approach facilitates the identification of high mass proteins on the our low extraction potential mass microscope. The sensitivity of the combined method is estimated to be better than 80 fmol. Awe3D and Spatial Image Composer software tools are used to analyze the spectral data and produce broad mass range microscope mode, single  $m/z$  microprobe mode and single compound microscope mode ion images.

## 7.1 Introduction

The strength of MALDI imaging mass spectrometry lies in its ability to record the location and  $m/z$ -value of biomolecules present in a sample simultaneously. For complex biological samples the acquired mass information does not automatically yield compound identification. Especially for the identification of high mass proteins imaging MS has to be complemented with top-down or bottom-up compound identification strategies (Figure 7.1).<sup>135</sup> Using a ToF-ToF- or FTICR-mass spectrometer a top-down approach can be applied directly to the intact biomolecules desorbed and ionized from tissue in a microprobe imaging experiment. However, this approach can only be successful for low molecular weight proteins and the amount of sample (consumption) will limit the number of proteins that can be imaged and identified from the sample in this way. In a more efficient approach the compound identification strategies indicated in Figure 7.1 are applied to homogenates of the system under study and the derived knowledge is combined in sample specific atlases, which can be used to identify compounds in imaging MS experiments. The strength of this imaging / identification strategy has been shown for different samples.

One particular bottom-up compound identification strategy that has potential for application with imaging MS is the so-called molecular scanner methodology<sup>146, 147</sup>. This approach is not only of interest for protein identification from homogenates but can also be applied directly on tissue (see below). The molecular scanner methodology was introduced by Hochstrasser and co-workers to reduce the time needed for the peptide mass fingerprinting (PMF) analysis of complex mixtures of proteins. Proteins that have been separated on a SDS-PAGE gel by one- (1-DE) or two-dimensional electrophoresis (2-DE) are digested and electro-transferred in parallel. This so-called one-step digestion-transfer (OSDT) is achieved by electroblotting the entire protein content of the gel through a trypsin containing membrane onto a poly(vinylidene difluoride) (PVDF) capture membrane. During this blotting procedure there is little migration of the peptides in the direction perpendicular to the driving electric field. The spatial distribution of the peptides on the gel is transferred to the membrane. Subsequently, the peptide bands on the capture membrane can be analyzed directly using MALDI<sup>3, 4</sup>. In conventional in-gel digestion / PMF experiments all individual protein containing spots have to be excised and treated with an enzymatic digest separately before mass spectrometric analysis is possible.

In recent work of Stoeckli and co-workers part of the protein content of a mouse brain tissue section was electroblotted through a trypsin membrane onto a PVDF capture membrane without a gel-separation step.<sup>83</sup> In the subsequent scanning microprobe MALDI imaging experiments no significant distortion of the spatial organization was observed. In combination with a (traditional) molecular scanner analysis of the protein content of the sample separated on a gel or another trypsin based compound identification strategy, this approach offers means of identification of the proteins present in the sample. In addition to the identification capabilities the combination of imaging MS and the molecular scanner methodology has other advantages. The tryptic digestion of proteins present in the sample will increase the sensitivity



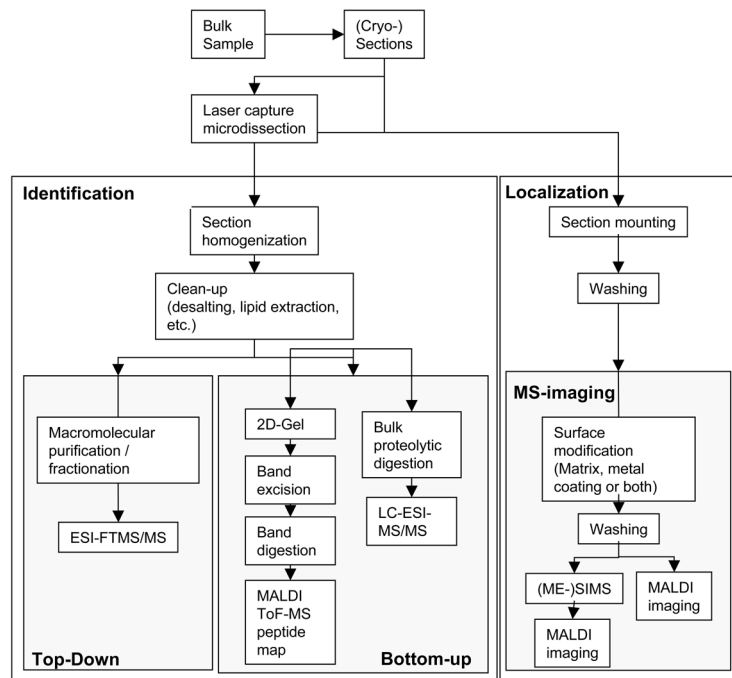


**Figure 7.1** Different strategies for the identification and localization of proteins present in a (tissue) sample. This figure was taken from ref. 135.

since instead of single high mass protein ions; multiple peptide ions of lower molecular masses (typically < 3000 Da) are imaged. Furthermore, the transblotting process separates the proteins from the other components present in the tissue, which reduces the complexity of sample. On the other hand indications were found that some of the proteins are more easily extracted from the tissue than others. Therefore, only a part of the whole protein content of the tissue can be analyzed in this way.<sup>148, 149</sup>

Recently, a novel approach to macromolecular imaging mass spectrometry was demonstrated: microscope mode MALDI imaging MS. This high speed, high resolution imaging MS technique uses position correlated ion detection instead of position correlated ion generation to record mass resolved ion images (Chapter 3 of this thesis).<sup>100, 150</sup> It utilizes stigmatic ion optics to record selected mass (window) ion images at 4  $\mu\text{m}$  spatial resolution from within the area of the laser spot (200  $\mu\text{m}$  in diameter). Larger areas are imaged by continuous movement of the sample through the laser spot and subsequent concatenation of the resulting ion images, using dedicated in-house developed software (scanning microscope mode imaging). The mass

microscope can also be operated in microprobe mode. In this way ion images for every mass within the selected mass window can be obtained at the cost of lower lateral resolution.<sup>67</sup> Here, we explore the combination of microscope mode MALDI imaging and the molecular scanner PMF methodology. The extension of this MS imaging methodology with improved identification possibilities will help develop it into a valuable tool for the spatially resolved biochemical analysis of biological samples. The increased sensitivity for high mass protein detection/identification is particularly beneficial for the microscope mode imaging methodology, since our MALDI ion microscopy set-up uses low extraction and post-acceleration potentials. Furthermore, the high lateral resolution of the microscope mode approach can be used to gain more insight in the distribution of the peptides on the PVDF membrane after OSDT. This first study is limited to the imaging MS analysis of electroblots of proteins isolated on 1-DE gels. The sensitivity for the identification of high mass proteins in this combined approach is tested on standards. Analogous to the recent work of Scherl *et al.*<sup>151</sup> we evaluated the value of goldcoating of the sample (PVDF membrane + matrix crystals) for imaging MS experiments on our direct extraction mass microscope. With a view towards microscope mode imaging MS of tissue samples prepared by combined blotting and tryptic digestion, molecular scanner samples of a commercial mixture of proteins and a homogenate of cancerous oesophagus cells were analyzed. Broad mass range microscope mode, single mass microprobe and single mass microscope mode images were obtained and the information was compared. The experiments described herein produce very large image and spectral datasets. Software tools have been developed to handle these datasets and visualize the different datasets obtained in this study

## 7.2 Experimental section

### 7.2.1 Sample preparation

The molecular scanner sample preparation was performed by the Biomedical Proteomics Research Group at the Geneva University Hospital. The procedure is detailed elsewhere<sup>146, 151</sup>, here only a short overview is included. The proteins present in the sample are separated using one-dimensional electrophoresis according to Laemmli<sup>152</sup> with 12% T and 2.6 % C linear polyacrylamide gels. Subsequently, all isolated proteins are blotted through a trypsin containing membrane, where they are proteolytically digested. Finally, the resulting peptides are collected on a PVDF capture membrane. A  $\alpha$ -hydrocinnamic acid matrix solution (10 mg/ml HCCA in 70% v/v MeOH/1% v/v TFA/10mM NH<sub>4</sub>H<sub>2</sub>PO<sub>4</sub>) is deposited on the membrane in small droplets using a spotting robot, which was developed by the Geneva group. Subsequently the samples are goldcoated using a SCD 040 sputter coater (Balzers Union AG, Balzers, Liechtenstein). Proteins in a broad mass range were identified from their tryptic digests from a

commonly used protein mixture obtained from Bio-Rad (Hercules, CA, USA). The protein mixture contained the following proteins: myosin from rabbit skeletal muscle (MYSS),  $\beta$ -galactosidase from *Escherichia coli* (BGAL), phosphorylase b from rabbit skeletal muscle (PHS2), bovine serum albumin (BSA), ovalbumin from chicken hen egg white (OVAL), carbonic anhydrase type 2 from bovine serum (CAH2), trypsin inhibitor from soybean (ITRA), lysozyme from chicken hen egg white (LYSC) and trypsin inhibitor from bovine pancreas (BPT1). It has been shown before that MYSS is usually not extracted in the electroblotting step due to its high mass and BPT1 is not separated from the migration front in 1-DE.<sup>153</sup> The LYSC band was not analyzed in this study. Sensitivity studies were performed using a series of different amounts (200 fmol – 100 pmol) of BSA loaded on a 1-DE gel. The effect of the thickness of the gold layer was investigated on a 100 pmol transblotted BSA sample. For this purpose the gold layer thickness was varied from 1 to 10 nm.

### 7.2.2 (Imaging) Mass spectrometry

All mass spectrometric (imaging) experiments were performed on a TRIFT-II equipped with a UV-MALDI source for macromolecular stigmatic ion imaging, for details see Chapters 2 and 3 of this thesis. Our current set-up is capable of high lateral resolution microscope mode imaging of one selected mass window per cycle of the experiment. Simultaneously to the recording of the ion image, the mass spectrum of the ions that form the image is recorded using a 8-bit PCI-digitizer card (DP 240, Acqiris, Geneva, Switzerland). The mass window can be set using a pair of blanker plates, which prevent transmission of ions when a 200 Volts potential difference is applied to them. The transmitted  $m/z$  mass window is controlled using a Stanford delay generator (model DG535). The transmitted mass window can range from a single mass (at low  $m/z$ ) to the whole mass spectrum. In the experiments shown here the width of the transmitted mass windows was always at least 1 microsecond to prevent distortion of the ion images. This corresponds to a mass window of approximately 20 Da in the peptide mass range. The size of the laser spot ( $\sim 200 \mu\text{m}$  diameter) determines the area that is imaged in a single shot. Larger areas can be imaged by continuously scanning the sample stage during image acquisition. A macroscopic stigmatic ion image of the sample is constructed from multiple line scans with sufficient overlap. Home-built software is used to stitch the individual microscope mode images together. Besides, high lateral resolution microscope mode ion images of the selected mass windows, microprobe mode ion images can be obtained for each individual mass within this selected window. In microprobe mode image construction the maximum lateral resolution is defined by the pixel size, which equals the laser spot size. In scanning experiment the overlap between areas of the sample that are probed in subsequent laser shots is determined by the repetition rate of the laser (8 – 12 Hz), the sample stage scan speed (50 – 100  $\mu\text{m/s}$ ) and the laser spot size. In the experiments described here the sample was moved approximately 10 – 20  $\mu\text{m}$  between subsequent laser shots. Furthermore there is a 100  $\mu\text{m}$  shift between linescans. This makes that every 10-20 by 100  $\mu\text{m}$  area is sampled approximately 90 times. The pixels in the microprobe images are defined in this way.

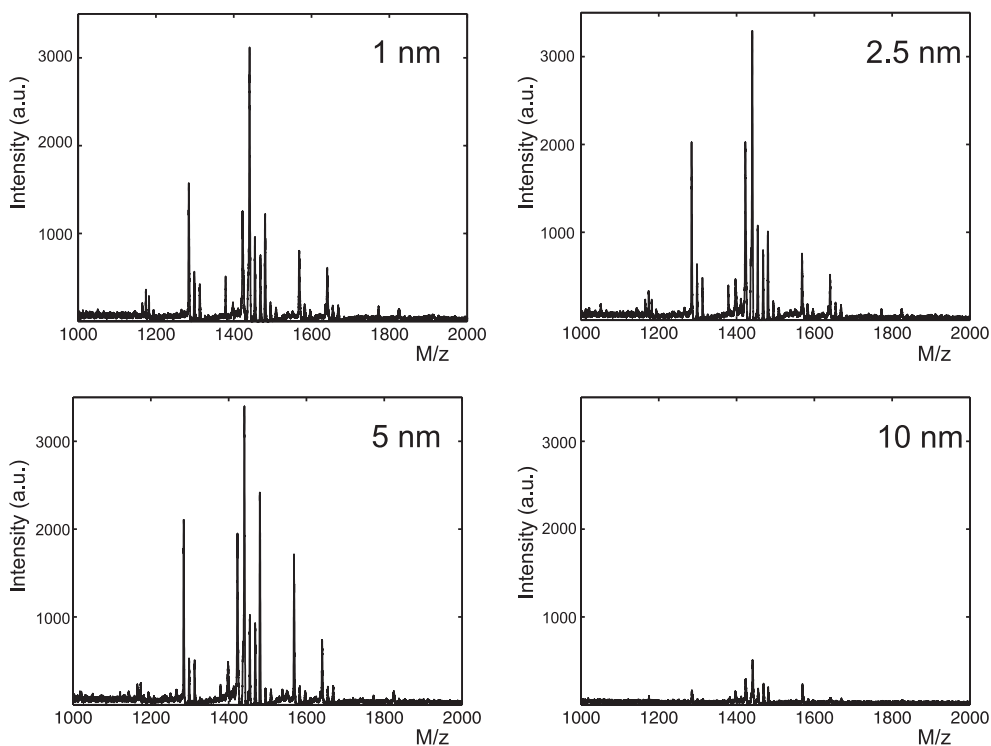


**Figure 7.2** MALDI mass spectra of BSA digests covered with different amounts of gold. The thickness of the applied layer is indicated. The spectra results from 100 subsequent laser shots.

## 7.3 Results

### 7.3.1 Goldcoating prevents charge build-up in the sample

Recently, it was shown that the deposition of a thin gold layer on the samples prepared for analysis using the molecular scanner methodology dramatically improves the quality of spectral data obtained with MALDI MS.<sup>151</sup> It was found that gold coating of the non-conductive PVDF membranes prevents charging effects which results in mass shifts and strongly reduced mass resolution. For low (8 kV) acceleration potentials the mass shift effects were found to be the largest. The mass microscope is operated at 3 kV extraction potential and has an energy acceptance window of 160 eV. Therefore charging effects are expected to affect the spectral

Q(pmol)	Tf1	Tf2	Tf3	Tf4	Tf5	Tf6	Tf7	Tf8	Tf9	Tf10	Tf11	Tf12
100	+	+	+	+	+		+	+	+	+	+	+
50	+	+	+	+	+	+	+	+	+	+		
25	+			+	+		+	+	+	+	+	+
12.5	+				+		+	+	+	+	+	+
6.25	+	+			+		+	+	+	+	+	
5	+				+		+	+	+	+		
2	+				+		+	+	+	+		
0.5	+							+	+	+		

**Table 7.1** The tryptic fragments that were detected for the different quantities of BSA loaded on the 1-DE gel. The mass and the sequence of the fragments Tf1 to Tf12 are included in Table 7.2. Five pmol was determined to be the lower limit for unambiguous identification. For an estimate of the sensitivity see text.

quality to an even larger extent than reported in the previous study. Moreover, since the mass microscope uses electrostatic lenses for stigmatic ion imaging residual charges on the sample will also affect the ion image quality. We compared the spectral and image quality obtained using the mass microscope on PVDF membranes with transblotted BSA peptides without goldcoating to similar samples that were coated with different thicknesses of gold. It was found that without gold coating charging resulted in large spot-to-spot variations in signal intensity. The charging effect was large enough to completely move the kinetic energy of the ions generated out of the energy acceptance window, which prevented any ions from being detected. To compensate for this the sample potential had to be raised by 500 – 800 V, which is indicative of a significant accumulation of negative charges on the sample. The application of a gold layer on the sample removed the need for sample potential compensation. In Figure 7.2 spectra that were obtained on samples covered with 1, 2.5, 5 and 10 nm thick layers of gold are shown. Already, the application of a 1 nm gold layer removes sample charging to the extent that mass spectra can be obtained. The mass resolution obtained in these experiments did not allow a detailed study on the effect of the thickness of the gold layers on the spectral quality. A 5 nm gold layer was needed to remove drifting of the ion images. In Section 7.3.4 the high quality of the ion images obtained with a 5 nm gold layer will be demonstrated. The application of a 10 nm thick gold layer significantly reduced the sensitivity.

### 7.3.2 Sensitivity

For an analysis of the sensitivity of the molecular scanner / microscope mode approach different amounts of BSA were loaded on a gel. After OSDT, matrix and gold deposition peptide spectra of the BSA digests were obtained. For this purpose the sample was scanned through the laser spot. One linescan consisted of 500 to 1250 laser shots. In Table 7.1 the

	Mass (Da)	Sequence
Tf1	927	YLYEIAR
Tf2	1050	EACFAVEGPK
Tf3	1194	DTHKSEIAHR
Tf4	1250	FKDLGEEHFK
Tf5	1284	HPEYAVSVLLR
Tf6	1306	HLVDEPQNLIK
Tf7	1440	RHPEYAVSVLLR
Tf8	1480	LGEYGFQNALIVR
Tf9	1568	DAFLGSFLYEYSR
Tf10	1640	KVPQVSTPTLVEVSR
Tf11	1824	RPCFSALTPDETYVPK
Tf12	1900	LGEYGFQNALIVRYTR

**Table 7.2.** The masses and amino acid sequences of the tryptic fragments of BSA, which were detected in the sensitivity tests.

peptides observed for the different amounts of BSA loaded are listed. In Table 7.2 the masses and the amino acid sequences of the detected tryptic fragments are included. The number of species found in the spectra varied from 4 to 11. When 200 fmol of BSA was loaded no peptides were detected. For all samples the strongest signal was obtained for the  $m/z$  1480 peptide. For the larger amounts of BSA ( $\geq 5$  pmol) a mass accuracy of 50 – 100 ppm and mass resolution of 2000 was achieved. For lower amounts of sample the laser intensity had to be increased to record sufficient peptide signal. At these elevated laser intensities the kinetic energy distributions of the analytes broadened (see also Chapter 3) which resulted in deterioration of the mass accuracy and mass resolution. For the different amounts of BSA loaded it was evaluated if the peptide ion signals detected were sufficient for a positive identification in a Mascot PMF Search (<http://www.matrixscience.com>) using the SwissProt database. At 5 pmol BSA could still be identified unambiguously, for lower amounts the number of different peptides detected was insufficient for positive identification. The spectra were obtained by scanning the sample through the 200  $\mu\text{m}$  diameter laser spot. The band on the PVDF membrane containing the BSA peptides extended over approximately 4 mm in vertical direction. Most intense signals were obtained from the middle 1.5 mm. In horizontal direction the band extended approximately 8 mm. In one linescan between 0.5 and 0.8  $\text{mm}^2$  of the sample was analyzed. Depending on the total amount of protein material that was loaded the analyzed area contained 3 fmol to 2 pmol of the digested protein. In this estimate it is assumed that all the protein material is transferred from the gel to the membrane. For the lower limit for BSA identification, 5 pmol, the analyzed area contained an amount of peptide

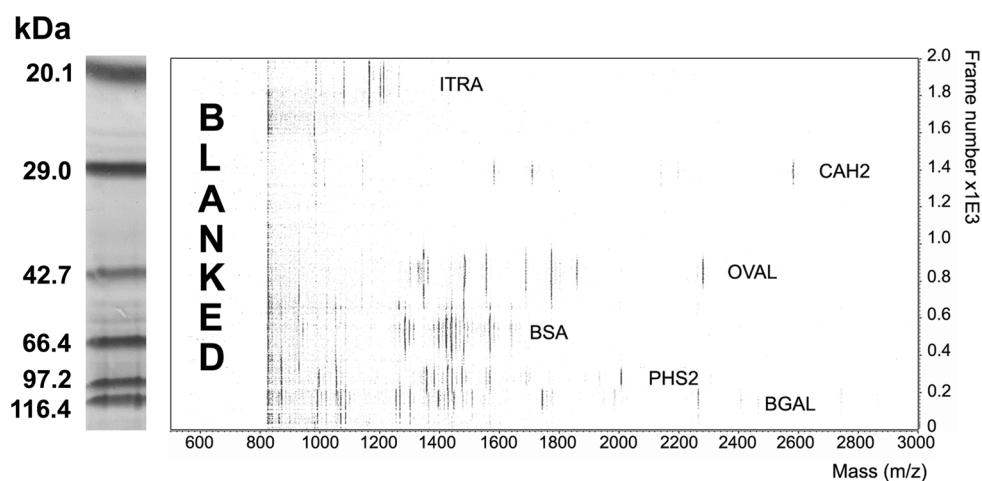


**Figure 7.3** The proteins present in a commercial mixture were separated on a 1-DE gel and subsequently analyzed using the molecular scanner methodology. On the left side an image of the gel stained with Coomassie Blue is shown. The positions of the peptide bands detected on the mass microscope and visualized using Awe3D software agree with the positions on the gel. The peptides localized in bands facilitated the identification of the proteins indicated.

material corresponding to 80 fmol of BSA on the original gel. Since in the scanning methodology employed not all of the sample material was consumed the 80 fmol is a conservative estimate of the sensitivity for large protein identification. Moreover, analysis of the 5 pmol dataset, revealed that selected single shot mass spectra demonstrated sufficient signal-to-noise ratio to detect all 6 peptides on single shot basis. From our estimate the amount of material used in a single shot experiment is 150 attomol. Recently, it was found that during the transfer a significant part of the peptides travel through the capture membrane and therefore are lost for analysis.<sup>154</sup> It also indicates that the peptides are not concentrated in the top most part of the capture membrane but will be distributed across its 100  $\mu\text{m}$  thickness. Efforts to further improve the sensitivity of the methodology are therefore directed towards quality improvement of the capture membrane.

### 7.3.3 Protein identification from a mixture

A capture membrane with peptide containing bands was prepared from a mixture of proteins as described in the Section 7.2.1. For each of the proteins approximately 100 pmol was loaded on the gel in a pre-mixed solution, six bands were analyzed using our MALDI / stigmatic ion imaging set-up. The left side of Figure 7.3 displays the result of the 1-DE gel separation stained with Coomassie Blue, in which the six targeted bands are visible. The sample was continuously

scanned through the laser spot at a speed of 100  $\mu\text{m/s}$ , which yielded 2000 mass spectra for a single scan. Only the ions with an  $m/z$ -value above  $m/z$  800 were recorded in this experiment. For the spectral analysis and representation of the acquired data we used in-house developed software: Awe3D. This software has been developed in our lab for the analysis of FT-ICR datasets and has been adapted for visualization of the data acquired in a molecular scanner experiment. More details on the software will be described in a forthcoming publication. In Figure 7.3 (right side) a screenshot of the data representation in Awe3D is shown. Along the horizontal axis  $m/z$  values are displayed while on the vertical axis there is the frame number or laser shot number. The six peptide-containing bands are clearly visible, and their localizations correspond to their positions on the gel. The software can be used to zoom in on individual peptide bands and inspect single shot mass spectra, which can be used to accurately determine the mass of the peptides recorded. The peptides detected yielded sufficient sequence coverage for a positive identification of the proteins in the first five bands starting from the bottom of Figure 7.3 (BGAL to CAH2). In the sixth band 4 peptides corresponding to trypsin inhibitor were detected, which was just enough for identification. However, the presence of several other unidentified signals made unambiguous identification troublesome.

#### 7.3.4 Microprobe and microscope mode imaging MS of molecular scanner samples

The mass microscope is capable of different imaging MS modes. As detailed in Chapters 2 and 3 it uses a phosphor screen – CCD camera configuration to capture stigmatic / microscope mode ion images. Blanker plates are used to restrict the detection of ions in a certain  $m/z$  - window: ranging from single mass to full mass range ( $<100,000$   $m/z$ ). Since the (single shot) mass spectra are recorded simultaneously with the images, microprobe images can be constructed from the original dataset for all different masses that lie within the selected mass window. This concept is demonstrated in the first two lanes of Figure 7.4A. A 35 mm long molecular scanner sample loaded with proteins extracted from human oesophagus cancer cells was continuously moved through the 200  $\mu\text{m}$  diameter laser spot in one direction at 100  $\mu\text{m/s}$ , while simultaneously images and mass spectra ( $m/z > 800$ ) were recorded at a rate of 9 Hz. In this way a linescan consisting of 3300 individual images and spectra is obtained. The distance over which the sample is moved in between subsequent laser shots is determined by the sample stage scan speed and the repetition rate of the laser. In this particular experiment this step size was equal to 11.1  $\mu\text{m}$ . At the end of each linescan a new starting position for the next linescan was defined by returning the sample to the starting position of the previous linescan and shifting it 100  $\mu\text{m}$  in a direction perpendicular to the scan direction. In this way 10 linescans consisting of 3300 individual images and spectra were recorded, this resulted in a total of 20 Gb image data and 3 Gb spectral data. For the handling and representation of these large datasets new software tools were developed. The Spatial Image Composer (SIC) software can be used to produce macroscopic stigmatic ion images for the hardware selected mass



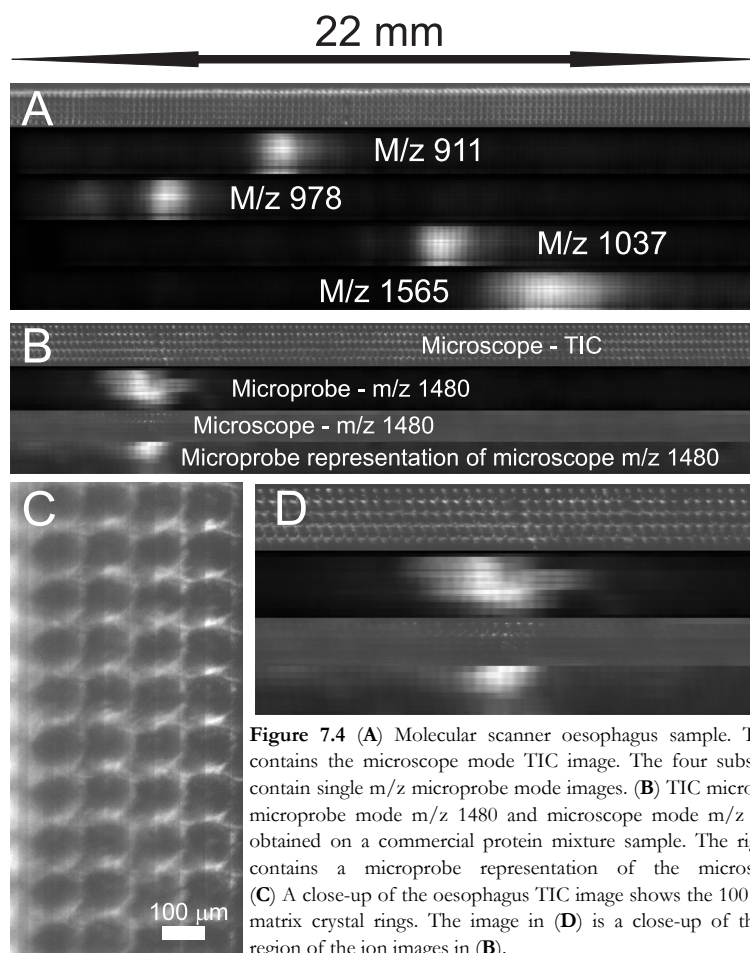


**Figure 7.4** (A) Molecular scanner oesophagus sample. The top lane contains the microscope mode TIC image. The four subsequent lanes contain single  $m/z$  microprobe mode images. (B) TIC microscope mode, microprobe mode  $m/z$  1480 and microscope mode  $m/z$  1480 images obtained on a commercial protein mixture sample. The rightmost lane contains a microprobe representation of the microscope mode (C) A close-up of the oesophagus TIC image shows the 100  $\mu\text{m}$  diameter matrix crystal rings. The image in (D) is a close-up of the  $m/z$  1480 region of the ion images in (B).

window as well as microprobe mode images for all  $m/z$  values within this window. Technical details on the SIC software will be provided in a forthcoming publication; here we demonstrate its image generation capabilities. The neighboring microscope mode ion images from a single linescan are partly overlapped according to the step size and the magnification factor of the experiment. The (fluorescence) intensity of overlapping pixels is averaged. Subsequently, the separate linescan images are concatenated in a similar way. The result for the oesophagus sample is shown in Figure 7.4A (first lane), in Figure 7.4C a zoom of a 0.5 x 1 mm area of the sample is included. The high spatial resolution of the individual ion images is maintained and reveals a ring-like structure, which results from the matrix deposition. It is immediately clear that re-solvation and redistribution of the analytes within these structures will limit the spatial resolution that can be obtained in this way. The SIC software can also be used to build

microprobe mode images from the mass spectra, which are recorded with every image/laser shot. The step size of the experiment defines  $11.1 \mu\text{m} \times 100 \mu\text{m}$  areas on the sample, which are probed approximately 60 times. The intensity of the selected mass is averaged for each of these individual microprobe pixels. Lanes 2 to 5 of Figure 7.4A contain microprobe mode images of the sample for the masses indicated. Although many different peptides were detected for the oesophagus sample this did not result in identification of their protein precursors. High salt concentrations in the sample prevented the formation of distinguishable bands during the 1-DE gel separation step

Besides the broad mass range microscope mode and single mass microprobe images, very small mass range microscope mode images can be obtained as well. For this purpose the ion blankers are unblanked only for a very short period in time:  $1 \mu\text{s}$ . In this way detailed spatial maps of a particular ion species can be recorded. Figure 7.4B contains images that result from 9 linescans of 3500 individual images and spectra obtained on the broad range protein standards sample used before in this study. The first lane contains the TIC (total ion count) image ( $m/z > 800$ ), the second image is a microprobe image for  $m/z$  1480 that was obtained using the SIC software. The  $m/z$  1480 peptide is a product from the tryptic digestion of BSA. The image in the third lane is a microscope mode image of the distribution of the peptide found at  $m/z$  1480. This image was recorded in a separate measurement of 6 linescans at a fresh position on the sample. Therefore it cannot be compared directly to the first two images. The last lane contains the microprobe mode representation of the microscope mode  $m/z$  1480 dataset. From this image and the close-up of the  $m/z$  1480 band region in Figure 7.4D it is apparent that the location of the band is similar in the two different imaging modes. The areas of high intensity correspond exactly. In the microscope mode representation the areas of high signal intensity are localized; the microscopic details of the sample preparation are visible. In microprobe mode the whole  $\sim 200 \mu\text{m}$  diameter area, that is illuminated by one laser pulse is given the same intensity, corresponding to the total signal for a specific  $m/z$ -value coming from this area. This intensity is distributed over many individual pixels in microscope mode, which causes the higher contrast in the microprobe mode images.

## 7.4 Discussion and conclusions

The molecular scanner approach makes it possible that high molecular mass proteins like  $\beta$ -galactosidase (116 kDa) can be identified on a TRIFT-II mass spectrometer, which is operated at low extraction field and limited post-acceleration possibilities. The reduction in mass of the individual analyte species that have to be analyzed as well as multiple peptide digestion products per protein facilitate this. The sensitivity for the unambiguous identification BSA is estimated to be better than 80 fmol. At the moment the factor limiting this number is quality of the capture membrane. Molecular scanner sample preparation combined with 5 nm goldcoating is compatible with high lateral resolution microscope mode imaging MS. With the

newly developed SIC software we are capable of constructing microscope mode ion images of macroscopic samples within a mass range that is set in the instrument's hardware. For this purpose the individual captured phosphor screen images are concatenated. Furthermore, microprobe mode images for all single  $m/z$ -values within the selected mass range can be constructed from the spectral data that is recorded simultaneously. In the TIC and single species microscope mode images rings of matrix crystals with a diameter of approximately 100  $\mu\text{m}$  were visualized. These results demonstrate that the current matrix deposition method is not suited for high lateral resolution imaging MS.

The molecular scanner approach to tissue imaging as described in the Section 7.1 can be used to increase sensitivity and identification of high mass proteins. To take advantage of the high lateral resolution that can be achieved in microscope mode imaging, the sample preparation will have to be optimized. Electrospray and sonic spray matrix deposition methods produce micron size matrix crystals from a spray of very small droplets. These sample preparation methods are compatible with high lateral resolution imaging<sup>66</sup>, though the limited sample wetting can result in a loss of sensitivity due to reduced incorporation of the proteins/peptides present in the sample.<sup>60</sup> The sensitivity that can be obtained in electrospray and sonic spray matrix deposition will have to be evaluated. In this respect the optimization of the capture membrane is of great importance. Developments should be aimed at preventing the transferred peptides to pass through the membrane and concentration near the membrane surface.

**Acknowledgement.** We would like to acknowledge Ali R. Vaezzadeh for the preparation of the molecular scanner samples used in this study and for his greatly appreciated input. Furthermore, we would like to thank Catherine Zimmerman and Denis Hochstrasser for the fruitful discussions on the combined microscope mode / molecular scanner approach.



# Bibliography

1. R. Castaing and G. Slodzian, *Microanalyse par émission ionique secondaire*, J. Microsc. **1**, 395-410 (1962)
2. J. C. Vickerman and D. Briggs, *ToF-SIMS Surface Analysis by Mass Spectrometry*, 1<sup>st</sup> ed.; IM Publications and SurfaceSpectra Limited: Huddersfield, (2001)
3. M. Karas, D. Bachmann and F. Hillenkamp, *Influence of the wavelength in high-irradiance ultraviolet laser desorption mass spectrometry of organic molecules*, Anal. Chem. **57**, 2935-2939 (1985)
4. M. Karas, D. Bachmann, U. Bahr and F. Hillenkamp, *Matrix-assisted ultraviolet laser desorption of non-volatile compounds*, Int. J. Mass Spectrom. Ion Proc. **78**, 53-68 (1987)
5. P. A. v. Veelen, C. R. Jimenez, K. W. Li, W. C. Wildering, W. P. M. Geraerts, U. R. Tjaden and J. v. d. Greef, *Direct peptide profiling of single neurons by matrix-assisted laser desorption ionization mass spectrometry*, Org. Mass Spectrom. **28**, 1542-1546 (1993)
6. C. R. Jimenez, P. A. v. Veelen, K. W. Li, W. C. Wildering, W. P. M. Geraerts, U. R. Tjaden and J. v. d. Greef, *Neuropeptide expression and processing as revealed by direct matrix-assisted laser-desorption ionization mass spectrometry of single neurons*, J. Neurochem. **62**, 404-407 (1994)
7. R. B. Caprioli, T. B. Farmer and J. Gile, *Molecular Imaging of Biological Samples: Localization of Peptides and Proteins Using MALDI-TOF MS*, Anal. Chem. **69**, 4751-4760 (1997)
8. D. M. Hercules, R. J. Day, K. Balasanmugam, T. A. Dang and C. P. Li, *Laser Microprobe Mass Spectrometry 2. Applications to structural Analysis*, Anal. Chem. **54**, 280A - 305A (1982)
9. K. Tanaka, H. Waki, Y. Ido, S. Akita, Y. Yoshida and T. Yoshida, *Protein and Polymer Analyses up to  $m/z$  100 000 by Laser Ionization Time-of-Flight Mass Spectrometry*, Rapid Commun. Mass Spectrom. **8**, 151-153 (1988)
10. K. Dreisewerd, *The Desorption Process in MALDI*, Chem. Rev. **103**, 395-425 (2003)
11. L. V. Zhigilei and B. J. Garrison, *Microscopic mechanisms of laser ablation of organic solids in the thermal and stress confinement regimes*, J. Appl. Phys. **88**, 1281-1298 (2000)
12. M. Handschuh, S. Nettesheim and R. Zenobi, *Laser-induced molecular desorption and particle ejection from organic films*, Appl. Surf. Sci. **137**, 125-135 (1999)
13. A. Vertes, R. Gijbels and R. D. Levine, *Homogeneous Bottleneck Model of Matrix-assisted Ultraviolet Laser Desorption of Large Molecules*, Rapid Comm. Mass Spectrom. **4228**, 228-233 (1990)
14. L. V. Zhigilei, E. Leveugle, B. J. Garrison, Y. G. Yingling and M. I. Zeifman, *Computer Simulations of Laser Ablation of Molecular Substrates*, Chem. Rev. **103**, 321-347 (2003)
15. R. Knochenmuss and R. Zenobi, *MALDI Ionization: The Role of In-Plume Processes*, Chem. Rev. **103**, 441-452 (2003)
16. R. Knochenmuss, *A Quantitative Model of Ultraviolet Matrix-Assisted Laser Desorption / Ionization Including Analyte Ion Generation*, Anal. Chem. **75**, 2199-2207 (2003)
17. M. Karas, M. Glückmann and J. Schäfer, *Ionization in matrix-assisted laser desorption / ionization: singly charged molecular ions are the lucky survivors*, J. Mass Spectrom. **35**, 1-12 (2000)
18. M. Karas and R. Krüger, *Ion Formation in MALDI: The Cluster Ionization Mechanism*, Chem. Rev. **103**, 427-439 (2003)

## Bibliography

19. R. Krüger, A. Pfenninger, I. Fournier, M. Glückmann and M. Karas, *Analyte Incorporation and Ionization in Matrix-Assisted Laser Desorption/Ionization Visualized by pH Indicator Molecular Probes*, *Anal. Chem.* **73**, 5812-5821 (2001)
20. R. Knochenmuss, A. Stortelder, K. Beuker and R. Zenobi, *Secondary ion-molecule reactions in matrix-assisted laser desorption/ionization*, *J. Mass. Spectrom.* **35**, 1237-1245 (2000)
21. R. Zenobi and R. Knochenmuss, *Ion Formation in MALDI Mass Spectrometry*, *Mass Spec. Rev.* **17**, 337-366 (1998)
22. R. Knochenmuss, *A quantitative model of ultraviolet matrix-assisted laser desorption/ionization*, *J. Mass Spectrom.* **37**, 867-877 (2002)
23. R. Knochenmuss and A. Vertes, *Time-delayed 2-Pulse Studies of MALDI Matrix Ionization Mechanisms*, *J. Phys. Chem. B* **104**, 5406-5410 (2000)
24. G. R. Kinsel, R. Knochenmuss, P. Setz, C. M. Land, S.-K. Goh, E. F. Archibong, J. H. Hardesty and D. C. Marynick, *Ionization energy reductions in small 2,5-dihydroxybenzoic acid-proline clusters*, *J. Mass. Spectrom.* **37**, 1131-1140 (2002)
25. S. Berkenkamp, C. Menzel, M. Karas and F. Hillenkamp, *Performance of Infrared Matrix-assisted Laser Desorption/Ionization Mass Spectrometry with Lasers Emitting in the 3  $\mu\text{m}$  Wavelength Range*, *Rapid Commun. Mass Spectrom.* **11**, 1399 - 1406 (1997)
26. S. Berkenkamp, M. Karas and F. Hillenkamp, *Ice as a matrix for IR-matrix-assisted laser desorption/ionization: Mass spectra from a protein single crystal*, *Proc. Natl. Acad. Sci. USA* **93**, 7003-7007 (1996)
27. I. Fournier, C. Marinach, J. C. Tabet and G. Bolbach, *Irradiation Effects in MALDI, Ablation, Ion Production, and Surface Modifications. Part II: 2,5-Dihydroxybenzoic Acid Monocrystals*, *J. Am. Soc. Mass Spectrom.* **14**, 893-899 (2003)
28. J. Kampmeier, K. Dreisewerd, M. Schrenberg and K. Strupat, *Investigations of 2,5-DHB and succinic acid as matrices for IR and UV MALDI. Part: I UV and IR laser ablation in the MALDI process*, *Int. J. Mass. Spectrom.* **169/170**, 31-41 (1997)
29. K. Dreisewerd, S. Berkenkamp, A. Leisner, A. Rohlfing and C. Menzel, *Fundamentals of matrix-assisted laser desorption/ionization mass spectrometry with pulsed infrared lasers*, *Int. J. Mass Spectrom.* **226**, 189-209 (2003)
30. A. Rohlfing, C. Menzel, L. M. Kukreja, F. Hillenkamp and K. Dreisewerd, *Photoacoustic Analysis of Matrix-Assisted Laser Desorption/Ionization Processes with Pulsed Infrared Lasers*, *J. Phys. Chem. B* **107**, 12275 - 12286 (2003)
31. P. Sigmund, *Theory of Sputtering. I. Sputtering Yield of Amorphous and Polycrystalline Targets*, *Phys. Rev.* **184**, 383-416 (1969)
32. H. M. Urbassek, *Molecular-dynamics simulations of sputtering*, *Nucl. Instr. and Meth. B* **122**, 427-441 (1997)
33. A. Delcorte, P. Bertrand and B. J. Garrison, *A microscopic view of organic sample sputtering*, *Appl. Surf. Sci.* **203-204**, 166-169 (2003)
34. A. Delcorte *ToF-SIMS Surface Analysis by Mass Spectrometry*; IM Publications and SurfaceSpectra Limited, Huddersfield, p. 161-194 (2001)
35. A. Delcorte and B. J. Garrison, *Particle-Induced Desorption of Kilodalton Molecules Embedded in a Matrix: A Molecular Dynamics Study*, *J. Phys. Chem. B* **107**, 2297-2310 (2003)
36. A. Delcorte, B. G. Segda, B. J. Garrison and P. Bertrand, *Inferring ejection distances and a surface energy profile in keV particle bombardment experiments*, *Nucl. Instr. and Meth. B* **171**, 277-190 (2000)
37. P. Sigmund *Sputtering by Particle Bombardment I*; Springer-Verlag, Berlin, p. 9-71 (1981)
38. A. Delcorte and B. J. Garrison, *High Yield Events of Molecular Emission Induced by Kilolectron Particle Bombardment*, *J. Phys. Chem. B* **104**, 6785-6800 (2000)
39. N. Winograd, *The Magic of Cluster SIMS*, *Anal. Chem.* **77**, 143A-149A (2005)

40. D. Weibel, S. Wong, N. Lockyer, P. Blenkinsopp, R. Hill and J. C. Vickerman, *A C<sub>60</sub> Primary Ion Beam System for Time of Flight Secondary Ion Mass Spectrometry: Its Development and Secondary Ion Yield Characteristics*, *Anal. Chem.* **75**, 1754-1764 (2003)
41. D. E. Weibel, N. Lockyer and J. C. Vickerman, *C<sub>60</sub> cluster ion bombardment of organic surfaces*, *Appl. Surf. Sci.* **231-232**, 146-152 (2004)
42. S. C. C. Wong, R. Hill, P. Blenkinsopp, N. P. Lockyer, D. E. Weibel and J. C. Vickerman, *Development of a C-60(+) ion gun for static SIMS and chemical imaging*, *Appl. Surf. Sci.* **203**, 219-222 (2003)
43. E. R. Fuoco, G. Gillen, M. B. J. Wijesundara, W. E. Wallace and L. Hanley, *Surface Analysis Studies of Yield Enhancements in Secondary Ion Mass Spectrometry by Polyatomic Projectiles*, *J. Phys. Chem. B* **105**, 3950-3956 (2001)
44. N. Davies, D. E. Weibel, P. Blenkinsopp, N. Lockyer, R. Hill and J. C. Vickerman, *Development and experimental application of a gold liquid metal ion source*, *Appl. Surf. Sci.* **203-204**, 223-227 (2003)
45. R. Žarić, B. Pearson, K. D. Krantzman and B. J. Garrison, *Molecular dynamics simulations to explore the effect of projectile size on the ejection of organic targets from metal surfaces*, *Int. J. Mass Spectrom. Ion Proc.* **174**, 155-166 (1998)
46. R. R. Rickman, S. V. Verkhoturov and E. A. Schweikert, *Cluster secondary ion mass spectrometry: an insight into "super-efficient" collision cascades*, *Appl. Surf. Sci.* **231-232**, 54-58 (2004)
47. R. D. Rickman, S. V. Verkhoturov, E. S. Parilis and E. A. Schweikert, *Simultaneous Ejection of Two Molecular Ions from keV Gold Atomic and Polyatomic Projectile Impacts*, *Phys. Rev. Lett.* **92**, 047601 (2004)
48. Z. Postawa, B. Czerwinski, M. Szewczyk, E. J. Smiley, N. Winograd and B. J. Garrison, *Microscopic Insights into the Sputtering of Ag{111} Induced by C<sub>60</sub> and Ga Bombardment*, *J. Phys. Chem. B* **108**, 7831-7838 (2004)
49. A. Delcorte, N. Médard and P. Bertrand, *Organic Secondary Ion Mass Spectrometry: Sensitivity Enhancement by Gold Deposition*, *Anal. Chem.* **74**, 4955-4968 (2002)
50. A. Delcorte, J. Bour, F. Aubriet, J.-F. Muller and P. Bertrand, *Sample Metallization for Performance Improvement in Desorption/Ionization of Kildalton Molecules: Quantitative Evaluation, Imaging Secondary Ion MS and Laser Ablation*, *Anal. Chem.* **75**, 6875-6885 (2003)
51. L. Adriaensen, F. Vangaever and R. Gijbels, *Metal-Assisted Secondary Ion Mass Spectrometry: Influence of Ag and Au Deposition on Molecular Ion Yields*, *Anal. Chem.* **76**, 6777-6785 (2004)
52. A. Delcorte, X. V. Eynde, P. Bertrand, J. C. Vickerman and B. J. Garrison, *Kiloelectronvolt Particle-Induced Emission and Fragmentation of Polystyrene Molecules Adsorbed on Silver: Insights from Molecular Dynamics*, *J. Phys. Chem. B* **104**, 2673-2691 (2000)
53. K. L. Busch, B. H. Hsu, Y.-X. Xie and R. G. Cooks, *Matrix Effects in Secondary Ion Mass Spectrometry*, *Anal. Chem.* **55**, 1157-1160 (1983)
54. K. J. Wu and R. W. Odom, *Matrix-Enhanced Secondary Ion Mass Spectrometry: A Method for Molecular Analysis of Solid Surfaces*, *Anal. Chem.* **68**, 873-882 (1996)
55. S. D. Hanton, P. A. Cornelio Clark and K. G. Owens, *Investigations of Matrix-Assisted Laser Desorption/Ionization Sample Preparation by Time-of-Flight Secondary Ion Mass Spectrometry*, *J. Am. Soc. Mass Spectrom.* **10**, 104-111 (1999)
56. M. Stoeckli, T. B. Farmer and R. B. Caprioli, *Automated Mass Spectrometry Imaging with a Matrix-Assisted Laser Desorption Ionization Time-of-Flight Instrument*, *J. Am. Soc. Mass Spectrom.* **10**, 67-71 (1999)
57. M. Stoeckli, P. Chaurand, D. E. Hallahan and R. M. Caprioli, *Imaging mass spectrometry: a new technology for the analysis of protein expression in mammalian tissues*, *Nature Med.* **7**, 493-496 (2001)
58. B. Spengler and M. Hubert, *Scanning Microprobe Matrix-Assisted Laser Desorption Ionization (SMALDI) Mass Spectrometry - Instrumentation for Sub-Micrometer Resolved LDI and MALDI Surface Analysis*, *J. Am. Soc. Mass Spectrom.* **13**, 735-748 (2002)

## Bibliography

59. K. Dreisewerd, M. Schürenberg, M. Karas and F. Hillenkamp, *Influence of the laser intensity and spot size on the desorption of molecules and ions in matrix-assisted laser desorption/ionization with a uniform beam profile*, Int. J. Mass Spectrom. Ion Proc. **141**, 127-148 (1995)
60. S. A. Schwartz, M. L. Reyzer and R. M. Caprioli, *Direct tissue analysis using matrix-assisted laser desorption/ionization mass spectrometry: practical aspects of sample preparation*, J. Mass Spectrom. **38**, 699 - 708 (2003)
61. M. Stoeckli, D. Staab, M. Staufenbiel, K. H. Wiederhold and L. Signor, *Molecular imaging of amyloid beta peptides in mouse brain sections using mass spectrometry*, Anal. Biochem. **311**, 33-39 (2002)
62. J. Xu, C. W. Szakal, S. E. Martin, B. R. Peterson, A. Wucher and N. Winograd, *Molecule-Specific Imaging with Mass Spectrometry and a Buckminsterfullerene Probe: Application to Characterizing Solid-Phase Synthesized Combinatorial Libraries*, J. Am. Chem. Soc. **126**, 3902-3909 (2004)
63. T. P. Roddy, D. M. Cannon Jr., S. G. Ostrowski, N. Winograd and A. G. Ewing, *Identification of Cellular Sections with Imaging Mass Spectrometry Following Freeze Fracture*, Anal. Chem. **74**, 4020-4026 (2002)
64. D. M. Cannon Jr, M. L. Pacholski, T. P. Roddy, N. Winograd and A. G. Ewing, *Lipid-Specific Imaging of Membrane Dynamics using Mass Spectrometry*, SIMS XII, 931-934 (1999)
65. D. M. Cannon Jr, M. L. Pacholski, N. Winograd and A. G. Ewing, *Molecule Specific Imaging of Freeze-Fractured, Frozen-Hydrated Model Membrane Systems Using Mass Spectrometry*, J. Am. Chem. Soc. **122**, 603-610 (2000)
66. A. F. M. Altaelaar, J. van Minnen, C. R. Jimenez, R. M. A. Heeren and S. R. Piersma, *Direct molecular imaging of *Lymnaea stagnalis* nervous tissue at subcellular spatial resolution by mass spectrometry*, Anal. Chem. **77**, 735-741 (2005)
67. A. F. M. Altaelaar, I. Klinkert, K. Jalink, R. P. J. d. Lange, R. A. H. Adan, R. M. A. Heeren and S. R. Piersma, *Gold enhanced biomolecular surface imaging of cells and tissue by SIMS and MALDI mass spectrometry*, Anal. Chem., submitted (2005)
68. L. A. McDonnell, S. R. Piersma, A. F. M. Altaelaar, T. H. Mize, S. L. Luxembourg, P. D. E. M. Verhaert, J. v. Minnen and R. M. A. Heeren, *Subcellular imaging mass spectrometry of brain tissue*, J. Mass Spectrom. **40**, 160-168 (2005)
69. M. T. Bernius, Y.-C. Ling and G. H. Morrison, *High-resolution imaging with stigmatic ion optics*, J. Appl. Phys. **60**, 1904-1912 (1986)
70. B. W. Schueler, *Microscope imaging by time-of-flight secondary ion mass spectrometry*, Microsc. Microanal. Microstruct. **3**, 119-139 (1992)
71. B. Schueler, P. Sander and D. A. Reed, *A time-of-flight secondary ion microscope*, Vacuum **41**, 1661-1664 (1990)
72. J. F. Mahoney, J. Perel, S. A. Ruatta, P. A. Martino, S. Husain and T. D. Lee, *Massive Cluster Impact Mass Spectrometry - a New Desorption Method for the Analysis of Large Biomolecules*, Rapid Comm. Mass Spectrom. **5**, 441-445 (1991)
73. A. Oelsner, O. Schmidt, M. Schicketanz, M. Klais, G. Schönhense, V. Mergel, O. Jagutzki and H. Schmidt-Böcking, *Microspectroscopy and imaging using a delay line detector in time-of-flight photoemission microscopy*, Rev. Sci. Instrum. **72**, 3968-3974 (2001)
74. M. W. Thomson, *The energy spectrum of atoms during the high energy sputtering of gold*, Philos. Mag. **18**, 377-414 (1968)
75. F. S. Wouters, P. J. Verveer and P. I. H. Bastiaens, *Imaging biochemistry inside cells*, Trends Cell Biol. **11**, 203-211 (2001)
76. P. I. H. Bastiaens and R. Pepperkok, *Observing proteins in their natural habitat: the living cell*, TIBS **25**, 631-637 (2000)
77. J. Zhang, R. E. Campell, A. Y. Ting and R. Y. Tsien, *Creating new fluorescent probes for cell biology*, Nature Rev. **3**, 906-918 (2002)



78. S. Chandra, C. S. Fullmer, C. A. Smith, R. H. Wasserman and G. H. Morrison, *Ion microscopic imaging of calcium transport in the intestinal tissue of vitamin D-deficient and vitamin D-replete chickens: A <sup>44</sup>Ca stable isotope study*, Proc. Natl. Acad. Sci. **87**, 5715-5719 (1990)
79. N. E. Lewis and I. W. Levin, *Real-time, mid-infrared spectroscopic imaging microscopy using indium antimonide focal-plane array detection*, Appl. Spec. **49**, 672-678 (1995)
80. J. C. Simpson, R. Wellenreuther, A. Poustka, R. Pepperkok and S. Wiemann, *Systematic subcellular localization of novel proteins identified by large-scale cDNA sequencing*, EMBO reports **1**, 287-292 (2000)
81. A. Kumar, S. Agarwal, J. A. Heyman, S. Matson, M. Heidtman, S. Piccirillo, L. Umansky, A. Drawid, R. Jansen, Y. Liu, K.-H. Cheung, P. Miller, M. Gerstein, G. S. Roeder and M. Snyder, *Subcellular localization of the yeast proteome*, Genes & Dev. **16**, 707-719 (2002)
82. S. Hanash, *Disease proteomics*, Nature **422**, 226-232 (2003)
83. A. E. Roher, N. Weiss, T. A. Kokjohn, Y. M. Kuo, W. Kalback, J. Anthony, D. Watson, D. C. Luehrs, L. Sue, D. Walker, M. Emmerling, W. Goux and T. Beach, *Increased A beta peptides and reduced cholesterol and myelin proteins characterize white matter degeneration in Alzheimer's disease*, Biochem. **41**, 11080-11090 (2002)
84. M. Soderberg, C. Edlund, I. Alafuzoff, K. Kristensson and G. Dallner, *Lipid-composition in different regions of the brain in Alzheimers-disease senile dementia of Alzheimers type*, J. Neurochem. **59**, 1646-1653 (1992)
85. E. Phizicky, P. I. H. Bastiaens, H. Zhu, M. Snyder and S. Fields, *Protein analysis on a proteomic scale*, Nature **422**, 208-215 (2003)
86. D. Figeys, *Proteomics in 2002. A Year of Technical Development and Wide-Ranging Applications*, Anal. Chem. **75**, 2891-2905 (2003)
87. R. W. Garden and J. Sweedler, *Heterogeneity within MALDI Samples As Revealed by Mass Spectrometric Imaging*, Anal. Chem. **72**, 30-36 (2000)
88. R. Kruse and J. V. Sweedler, *Spatial Profiling Invertebrate Ganglia Using MALDI MS*, J. Am. Soc. Mass Spectrom. **14**, 752-759 (2003)
89. S. L. Luxembourg, L. A. McDonnell, M. Duursma, X. Guo and R. M. A. Heeren, *Effect of Local Matrix Crystal Variations in Matrix-Assisted Ionization Techniques for Mass Spectrometry (Chapter 5 of this thesis)*, Anal. Chem. **75**, 2333-2341 (2003)
90. P. J. Todd, T. G. Schaaff, P. Chaurand and R. M. Caprioli, *Organic ion imaging of biological tissue with secondary ion mass spectrometry and matrix-assisted laser desorption/ionization*, J. Mass Spectrom. **36**, 355-369 (2001)
91. T. L. Colliver, C. L. Brummel, M. L. Pacholski, F. D. Swanek, A. G. Ewing and N. Winograd, *Atomic and Molecular Imaging at the Single-Cell Level with TOF-SIMS*, Anal. Chem. **69**, 2225-2231 (1997)
92. L. A. McDonnell, T. H. Mize, S. L. Luxembourg, S. Koster, G. B. Eijkel, E. Verpoorte, N. F. de Rooij and R. M. A. Heeren, *Using Matrix Peaks to Map Topography: Increased Mass Resolution and Enhanced Sensitivity in Chemical Imaging*, Anal. Chem. **75**, 4373-4381 (2003)
93. R. C. Beavis and G. T. Chait, *Velocity distributions of intact high mass polypeptide molecule ions produced by matrix assisted laser desorption*, Chem. Phys. Lett. **181**, 479-484 (1991)
94. J. Zhou, W. Ens, K. G. Standing and A. Verentchikov, *Kinetic Energy Measurements of Molecular Ions Ejected into an Electric Field by Matrix-assisted Laser Desorption*, Rapid Commun. Mass Spectrom. **6**, 671-678 (1992)
95. G. R. Kinsel, M. E. Gimon-Kinsel, K. J. Gillig and D. H. Russell, *Investigation of the Dynamics of Matrix-assisted Laser Desorption/Ionization Ion Formation Using an Electrostatic Analyzer/Time-of-flight Mass Spectrometer*, J. Mass Spectrom. **34**, 684-690 (1999)

## Bibliography

96. W. Zhang and B. T. Chait, *Radial velocity distributions of molecular ions produced by matrix-assisted laser desorption/ionization*, Int. J. Mass Spectrom. Ion Proc. **160**, 259-267 (1997)
97. A. A. Puzosky, D. B. Geohegan, G. B. Hurst, M. V. Buchanan and B. S. Luk'yanchuk, *Imaging of Vapor Plumes Produced by Matrix-Assisted Laser Desorption: A Plume Sharpening Effect*, Phys. Rev. Lett. **83**, 444-447 (1999)
98. W. Ens, Y. Mao, F. Mayer and K. G. Standing, *Properties of Matrix-assisted Laser Desorption. Measurements with a Time-to-Digital Converter*, Rapid Commun. Mass Spectrom. **5**, 117-123 (1991)
99. F. Aksouh, P. Chaurand, C. Deprun, S. Della-Negra, J. Hoyes, Y. L. Beyec and R. R. Pinho, *Influence of the Laser Beam Direction on the Molecular Ion Ejection Angle in Matrix-assisted Laser Desorption/Ionization*, Rapid Commun. Mass Spectrom. **9**, 515-518 (1995)
100. S. L. Luxembourg, T. H. Mize, L. A. McDonnell and R. M. A. Heeren, *Rapid, high-spatial resolution mass spectrometric imaging of peptide and protein distributions on a surface (Chapter 3 of this thesis)*, Anal. Chem. **76**, 5339 - 5344 (2004)
101. A. Overberg, M. Karas, U. Bahr, R. Kaufmann and F. Hillenkamp, *Matrix-Assisted Infrared-Laser (2.94  $\mu\text{m}$ ) Desorption Ionization Mass-Spectrometry of Large Biomolecules*, Rapid Commun Mass Spectrom **4**, 293-296 (1990)
102. E. Hecht *Optics*, 2<sup>nd</sup> ed.; Addison-Wesley Publishing Company, p. 422-423 (1987)
103. A. M. Belu, M. C. Davies, J. M. Newton and N. Patel, *TOF-SIMS Characterization and Imaging of Controlled-Release Drug Delivery Systems*, Anal. Chem. **72**, 5625-5638 (2000)
104. C. M. John, R. W. Odom, L. Salvati, A. Annapragada and M. Y. Fu Lu, *XPS and TOF-SIMS Microanalysis of a Peptide/Polymer Drug Delivery Device*, Anal. Chem. **67**, 3871-3878 (1995)
105. A. Benninghoven, *Surface Analysis by secondary ion mass spectrometry (SIMS)*, Surface Science **299/300**, 246-260 (1994)
106. S. Chandra and G. H. Morrison, *Imaging ion and molecular transport at subcellular resolution by secondary ion mass spectrometry*, Int. J. Mass Spectrom. Ion Proc. **143**, 161-176 (1995)
107. S. Chandra, D. R. Smith and G. H. Morrison, *Subcellular Imaging by Dynamic SIMS Ion Microscopy*, Anal. Chem. **72**, 104A-114A (2000)
108. L. v. Vaecck, A. Adriaens and R. Gijbels, *Static Secondary Ion Mass Spectrometry: (S-SIMS) Part 1. Methodology and Structural Interpretation*, Mass Spec. Rev. **18**, 1-47 (1999)
109. M. L. Pacholski and N. Winograd, *Imaging with Mass Spectrometry*, Chem. Rev. **99**, 2977-3005 (1999)
110. T. P. Roddy, D. M. Cannon Jr, C. A. Meserole, N. Winograd and A. G. Ewing, *Imaging of Freeze-Fractured Cells with in Situ Fluorescence and Time-of-Flight Secondary Ion Mass Spectrometry*, Anal. Chem. **74**, 4011-4019 (2002)
111. M. R. Papantonakis, J. Kim, W. P. Hess and R. F. Haglund Jr., *What do matrix-assisted laser desorption/ionization mass spectra reveal about ionization mechanisms?*, J. Mass Spectrom. **37**, 639-647 (2002)
112. L. Adriaensen, F. Vangaever, J. Lenaerts and R. Gijbels, *Matrix-enhanced secondary ion mass spectrometry: the influence of MALDI matrices on molecular ion yields of thin organic films*, Rapid Commun. Mass Spectrom. **19**, 1017-1024 (2005)
113. A. J. Nicola, D. C. Muddiman and D. M. Hercules, *Enhancement of Ion Intensity in Time-of-Flight Secondary-Ionization Mass Spectrometry*, J. Am. Soc. Mass Spectrom. **7**, 467-472 (1996)
114. W. Szymczak and K. Wittmaack, *Effect of water treatment on analyte and matrix ion yields in matrix-assisted time-of-flight secondary ion mass spectrometry: the case of insulin in and on hydroxycinnamic acid*, Rapid Commun. Mass Spectrom. **16**, 2025-2033 (2002)
115. K. Wittmaack, W. Szymczak, G. Hoheisel and W. Tuszynski, *Time-of-flight Secondary Ion Mass Spectrometry of Matrix-Diluted Oligo- and Polypeptides Bombarded With Slow and Fast Projectiles: Positive and Negative Matrix and Analyte Ion Yields, Background Signals, and Sample Aging*, J. Am. Soc. Mass Spectrom. **11**, 553-563 (2000)

116. D. J. Harvey, *Matrix-assisted Laser Desorption/Ionization Mass Spectrometry of Phospholipids*, *J. Mass Spectrom.* **30**, 1333-1346 (1995)
117. B. Alberts *Molecular Biology of the Cell*; Garland Publishing Inc., New York(1994)
118. T. Takenawa and T. Itoh, *Phosphoinositides, key molecules for regulation of actin cytoskeletal organization and membrane traffic from the plasma membrane*, *Biochim. Biophys. Acta* **153**, 190-206 (2001)
119. S. F. Wong, C. K. Meng and J. B. Fenn, *Multiple Charging In Electrospray Ionization of Poly(ethylene glycols)*, *J. Phys. Chem.* **92**, 546-550 (1988)
120. M. B. Comisarow and A. G. Marshall, *Fourier transform ion cyclotron resonance spectroscopy*, *Chem. Phys. Lett.* **25**, 282-283 (1974)
121. R. M. A. Heeren, C. G. de Koster and J. J. Boon, *Direct Temperature Resolved HRMS of Fire-Retarded Polymers by In-Source PyMS on an External Ion Source Fourier Transform Ion Cyclotron Resonance Mass Spectrometer*, *Anal. Chem.* **67**, 3965-3970 (1995)
122. S. Koster, M. C. Duursma, J. J. Boon and R. M. A. Heeren, *Endgroup Determination of Synthetic Polymers by Electrospray Ionization Fourier Transform Ion Cyclotron Resonance Mass Spectrometry*, *J. Am. Soc. Mass Spectrom.* **11**, 536-543 (2000)
123. N. J. Jensen, K. B. Tomer and M. L. Gross, *Fast Atom Bombardment and Tandem Mass Spectrometry of Phosphatidylserine and Phosphatidylcholine*, *Lipids* **21**, 580-588 (1986)
124. R. C. Murphy and K. A. Harrison, *Fast Atom Bombardment Mass Spectrometry of Phospholipids*, *Mass Spectrom. Rev.* **13**, 57-75 (1994)
125. X. Han and R. W. Gross, *Structural Determination of Picomole Amounts of Phospholipids Via Electrospray Ionization Tandem Mass Spectrometry*, *J. Am. Soc. Mass Spectrom.* **6**, 1202-1210 (1995)
126. P. Domingues, M. R. M. Domingues, F. M. L. Amado and A. J. Ferrer-Correia, *Characterization of sodiated glycerol phosphatidylcholine by mass spectrometry*, *Rapid Commun. Mass Spectrom.* **15**, 799-804 (2001)
127. N. J. Jensen, K. B. Tomer and M. L. Gross, *FAB MS/MS for Phosphatidylinositol, -glycerol, -ethanolamine and Other Complex Phospholipids*, *Lipids* **22**, 480-489 (1987)
128. M. J. Cole and C. G. Enke, *Direct Determination of Phospholipid Structures in Microorganisms by Fast Atom Bombardment Triple Quadrupole Mass Spectrometry*, *Anal. Chem.* **63**, 1032-1038 (1991)
129. D. N. Heller, C. M. Murphy, R. J. Cotter, C. Fenselau and O. M. Uy, *Constant Neutral Loss Scanning for the Characterization of Bacterial Phospholipids Desorbed by Fast Atom Bombardment*, *Anal. Chem.* **60**, 2787-2791 (1988)
130. A. G. Marshall, T.-C. L. Wang and T. L. Ricca, *Tailored Excitation for Fourier Transform Ion Cyclotron Resonance Mass Spectrometry*, *J. Am. Chem. Soc.* **107**, 7893-7897 (1985)
131. J. A. Marto, F. M. White, S. Seldomridge and A. G. Marshall, *Structural Characterization of Phospholipids by Matrix-Assisted Laser Desorption/Ionization Fourier Transform Ion Cyclotron Resonance Mass Spectrometry*, *Anal. Chem.* **67**, 3979-3984 (1995)
132. V. H. Wysocky, H. I. Kenttamaa and R. G. Cooks, *Internal energy distributions of isolated ions after activation by various methods*, *Int. J. Mass Spectrom. Ion Proc.* **75**, 181-208 (1987)
133. S. Chandra, *SIMS ion microscopy as a novel, practical tool for subcellular chemical imaging in cancer research*, *Appl. Surf. Sci.* **203**, 679-683 (2003)
134. S. G. Ostrowski, C. T. v. Bell, N. Winograd and A. G. Ewing, *Mass Spectrometric Imaging of Highly Curved Membranes During Tetrahymena Mating*, *Science* **305**, 71-73 (2004)
135. R. M. A. Heeren, L. A. McDonnell, E. Amstalden, S. L. Luxembourg, A. F. M. Altelaar and S. R. Piersma, *Why don't biologists use SIMS?*, *Appl. Surf. Sci.*, accepted for publication (2006)

## Bibliography

136. F. Kollmer, *Cluster primary ion bombardment of organic materials*, Appl Surf Sci **231-232**, 153-158 (2004)
137. D. Touboul, F. Hagland, A. Brunelle, R. Kersting, E. Tallarek, B. Hagenhoff and O. Laprevote, *Tissue Molecular Ion Imaging by Gold Cluster Ion Bombardment*, Anal. Chem. **76**, 1550-1559 (2004)
138. R. W. Linton, M. P. Mawn, A. M. Belu, J. M. DeSimone, M. O. Hunt, Y. Z. Menceloglu, H. G. Cramer and A. Benninghoven, *Time-of-Flight Secondary-Ion Mass-Spectrometric Analysis of Polymer Surfaces and Additives*, Surf. Interface Anal. **20**, 991-999 (1993)
139. H. Nygren, P. Malmberg, C. Kriegeskotte and H. F. Arlinghaus, *Bioimaging TOF-SIMS: localization of cholesterol in rat kidney sections*, FEBS Lett. **566**, 291-293 (2004)
140. L. K. Liu, K. L. Busch and R. G. Cooks, *Matrix-Assisted Secondary Ion Mass Spectra of Biological Compounds*, Anal. Chem. **53**, 109-113 (1981)
141. J. Naban-Maïllet, D. Lesage, A. Bossée, Y. Gimbert, J. Sztáray, K. Vékey and J.-C. Tabet, *Internal energy distribution in electrospray ionization*, J. Mass. Spectrom. **40**, 1-8 (2005)
142. A. Benninghoven *Ion formation from organic solids*; Springer Verlag, Berlin, Germany, p. 78 (1983)
143. A. Delcorte and P. Bertrand, *Kinetic energy distributions of secondary molecular ions from thin organic films under ion bombardment*, Nucl. Instr. and Meth. B **115**, 246-250 (1996)
144. L. Dráhos and K. Vékey, *MassKinetics: a theoretical model of mass spectra incorporating physical processes, reaction kinetics and mathematical descriptions*, J. Mass. Spectrom. **36**, 237 (2001)
145. S. L. McArthur, M. C. Vendettuoli, B. D. Ratner and D. G. Castner, *Methods for Generating Protein Molecular Ions in ToF-SIMS*, Langmuir **20**, 3704-3709 (2004)
146. P.-A. Binz, M. Müller, D. Walther, W. V. Bienvenut, R. Gras, C. Hoogland, G. Bouchet, E. Gasteiger, R. Fabbretti, S. Gay, P. Palagi, M. R. Wilkins, V. Rouge, L. Tonella, S. Paesano, G. Rossellat, A. Karmime, A. Bairoch, J.-C. Sanchez, R. D. Appel and D. F. Hochstrasser, *A molecular scanner to automate proteomic research and to display proteome images*, Anal. Chem. **71**, 4981-4988 (1999)
147. W. V. Bienvenut, J.-C. Sanchez, A. Karmime, V. Rouge, K. Rose, P.-A. Binz and D. F. Hochstrasser, *Towards a Clinical Molecular Scanner for Proteome Research: Parallel Protein Chemical Processing before and during Western Bolt*, Anal. Chem. **71**, 4800-4807 (1999)
148. P. Chaurand, S. Fouchecourt, B. B. DaGue, B. J. Xu, M. J. Reyzer, M.-C. Orgebin-Crist and R. M. Caprioli, *Profiling and imaging proteins in the mouse epididymis by imaging mass spectrometry*, Proteomics **3**, 2221-2239 (2003)
149. P. Chaurand, B. B. DaGue, R. S. Pearsall, D. W. Treadgill and R. M. Caprioli, *Profiling proteins from azoxymethane-induced colon tumors at the molecular level by matrix-assisted laser desorption/ionization mass spectrometry*, Proteomics **1**, 1320-1326 (2001)
150. S. L. Luxembourg, L. A. McDonnell, T. H. Mize and R. M. A. Heeren, *Infrared Mass Spectrometric Imaging below the Diffraction Limit (Chapter 4 of this thesis)*, J. Prot. Res. **4**, 671-673 (2005)
151. A. Scherl, C. G. Zimmermann-Ivol, J. D. Dio, A. R. Vaezzadeh, P.-A. Binz, M. Amez-Droz, R. Cochard, J.-C. Sanchez, M. Glückmann and D. F. Hochstrasser, *Gold coating of non-conductive membranes before matrix-assisted laser desorption/ionization tandem mass spectrometric analysis prevents charging effect*, Rapid. Comm. Mass Spectrom. **19**, 605-610 (2005)
152. U. K. Laëmmli, *Cleavage of structural proteins during the assembly of the head of bacteriophage T4*, Nature **277**, 680-685 (1970)
153. W. V. Bienvenut, C. Déon, J.-C. Sanchez and D. F. Hochstrasser, *Enhanced protein recovery after electrotransfer using square wave alternating voltage*, Anal. Biochem. **307**, 297-303 (2002)
154. A. R. Vaezzadeh and C. G. Zimmermann, Personal communication (2005)

## Summary

We have used the term dynamic molecular landscape as a metaphor to describe the complex molecular organization at cellular level. This landscape is formed by an extensive collection of different biomolecules, like DNA, RNA, phospholipids, carbohydrates and proteins. It is subject to changes, continuously, as different tasks are being performed. Proteins form an important subset of these functional biomolecules; they are considered to be the workhorses in cells. In order to understand the functioning or malfunctioning of the many different biological processes it is very important to obtain knowledge on the identity, quantity, structure, function, spatial organization and possible modification of proteins. Now, that mass spectrometry has been established as *the* tool for the analysis of proteins a new challenge awaits: the development of spatially resolved mass spectrometry directly on biological tissue and cells at single cell level or beyond (**Chapter 1**).

The challenges that high lateral resolution macromolecular ion imaging is currently facing include realization of:

- sufficient lateral resolution for imaging at cellular level
- rapid imaging methodologies
- identification of the detected species
- optimized sample preparation.

The work described in this thesis contributes to the development of imaging mass spectrometry into a valuable research tool for life sciences. We have implemented a stigmatic or microscope mode ion imaging methodology for MALDI MS. The results presented in this thesis demonstrate that this new approach to macromolecular imaging MS results in a significant gain in attainable lateral resolution, reduction of experiment time and increased versatility in choice of ionization techniques. In order to extend its mass range and to increase protein identification possibilities we have performed an explorative study on the application of stigmatic imaging in combination with the molecular scanner methodology. Sample preparation for matrix-assisted imaging MS has been studied on microscopic scale using (ME-) SIMS.

In **Chapter 2** we give an overview of the current status of the imaging MS research field, with a strong focus on SIMS and MALDI. We discuss some of the fundamental and practical aspects of both techniques as well as their strengths and weaknesses with respect to imaging MS.

## *Summary*

MALDI is considered to be a very gently ionization technique, capable of producing intact ions of very high-mass molecules (up to hundreds of kiloDaltons). The lateral resolving power that is routinely achieved in a scanning microprobe MALDI MS imaging experiment leaves room for improvement ( $\sim 25 - 100 \mu\text{m}$ ). The origin of this limited resolution is partly in the imaging methodology that is employed: scanning microprobe imaging. The theoretical maximum to the attainable lateral resolution in a microprobe experiment is limited to the microprobe spot size. A practical aspect to this is that the sensitivity is dramatically decreased for small laser spot sizes ( $< 10 \mu\text{m}$ ). Moreover, the scanning nature of a microprobe MALDI imaging experiment makes high resolution imaging MS experiments time-consuming. The sample preparation, the incorporation of the analyte molecules in the matrix crystals, is a crucial element of a MALDI MS imaging experiment, in which the attainable sensitivity and spatial resolution are competing factors. High sensitivity requires wetting of the sample and large matrix crystals, at the same time this promotes diffusion of the analyte species, resulting in deterioration of the lateral resolution.

SIMS has been a powerful imaging MS technique since it was developed in the 60's of the past century. However, the applicable mass range in SIMS is limited. The energetic SIMS sputtering process induces extensive fragmentation of labile organic molecules; generally only imaging of elements and small organic fragments is possible. On the other hand SIMS can be used to obtain ion images with very high spatial resolution, in the order of 100 nanometer (using  $\text{Ga}^+$  primary ions). Lately, significant efforts are being made to increase the molecular ion yield in SIMS. One of the developed strategies uses a MALDI matrix to promote ionization and reduce fragmentation: matrix-enhanced SIMS (ME-SIMS).

The first macromolecular ion images obtained using microscope mode ion imaging are presented in **Chapter 3**. Microscope mode ion imaging uses stigmatic ion optics to project magnified ion optical images of distributions of molecules present in the sample onto a two-dimensional detector, which is positioned at the end of time-of-flight mass spectrometer. In this way a time-(or  $m/z$ -) separated series of ion images with spatial detail from within the laser spot is created. In contrast to the conventional scanning microprobe approach in which the ionizing beam is scanned across the sample surface (or vice versa). The maximum attainable spatial resolution is not determined by the size of the laser spot, but rather by the quality and tuning of the ion optics and the fundamentals of the desorption process. To evaluate the performance of the mass microscope homogeneous MALDI samples were covered with a fine mesh grid with  $25 \mu\text{m}$  pitch to provide recognizable structure. In less than 1 millisecond single shot substance P and insulin ion images were recorded from an area of  $200 \mu\text{m}$  in diameter, illuminated with an  $\text{N}_2$ -laser. The experiments were performed at a 12 Hz repetition rate, which was limited by the laser used. Currently, one mass(-window) can be imaged with high lateral resolution per cycle of the experiment. The stigmatic ion optics can be tuned for two modes of operation, resulting in  $100\times$  and  $200\times$  ion-optical magnification, respectively. For both modes the resolving power was determined to be  $4 \mu\text{m}$ .

The microscope mode approach removes the requirement of a highly focused laser beam to achieve high lateral resolution. A tight laser focus is not only difficult to achieve in the

environment of a mass spectrometer, but it also has the drawback of strongly reduced sensitivity. Moreover, the microscope mode approach is compatible with ionization techniques, which cannot be focused to a small spot, like Massive Cluster Ionization and IR-MALDI. The large area illumination makes the microscope mode methodology also inherently faster than the scanning microprobe approach, up to a factor of 2500 for a high resolution imaging experiment.

Large, macroscopic area ion imaging is demonstrated on a 2.5 mm diameter grid. For this purpose individual single shot ion images are stitched together using dedicated software. In this scanning microscope mode imaging the high lateral resolution of the individual images is maintained.

In **Chapter 4** the greater versatility in choice of ionization techniques is demonstrated. Single shot microscope mode ion images of bradykinin are obtained using a 2.94  $\mu\text{m}$  IR laser. These first ever high resolution IR-MALDI peptide ion images were recorded with a lateral resolution equal to that obtained in the UV-MALDI experiments of chapter 3 (= 4  $\mu\text{m}$ ). We show that for the set-up used diffraction limited focusing of the IR-laser would result in a smallest laser spot of 28  $\mu\text{m}$ . This equals the maximum spatial resolution that would be possible in an IR-MALDI microprobe experiment.

In **Chapter 5** we investigate sample preparation in matrix-assisted imaging MS techniques; in particular dried-droplet phospholipid samples were studied with ME-SIMS. Mass spectra of phospholipids were recorded; the pseudo-molecular ions detected were either protonated or sodiated. The spectra show great resemblance to phospholipid spectra recorded with MALDI. Similar pseudo-molecular and fragment ions are recorded using both techniques. In comparison to SIMS a clear reduction of the number of fragment ions versus intact pseudo-molecular species is observed. High spatial resolution (ME-)SIMS imaging analyses of the dried droplet samples reveal the heterogeneous nature of the samples. The experimental conditions varying on microscopic scale do not only affect the nature of the detected species (either sodiated or protonated) but also the degree of fragmentation and intact ion yield. The bias effects observed can influence the outcome of high lateral resolution matrix-assisted imaging MS studies. For this purpose the use of the much more homogeneous electrospray deposition (ESD) sample preparation is beneficial.

The enhancement of intact molecular ions observed in ME-SIMS is contributed to several factors: efficient ionization through charge transfer, disentanglement of long molecular chains through isolation and matrix cooling through internal energy reduction. In **Chapter 6** we use benzyl-substituted-benzylpyridinium (BPY) salts samples to study specifically this last effect. The preformed benzylpyridinium ions follow a simple unimolecular decay scheme when excited to an internal energy above their activation energy; this value varies with the identity of the substituted group. Precursor ion yield enhancement was observed for all different BPY ions studied in ME-SIMS with respect to SIMS. The decay of the BPY ions was studied at multiple instances, corresponding to different decay times, in the mass spectrometer. Kinetic

### *Summary*

energy distributions were determined to study differences between the SIMS and ME-SIMS sputtering process, and to derive decay rate coefficients for the unimolecular decay reaction. The decay rate constants and fragmentation ratios found are indicative of a cooler population of sputtered precursor ions in ME-SIMS. The results are explained in the framework of the precursor model: in ME-SIMS the sample volume excited by the collision cascade is increased, which results in a relatively larger portion of precursor ions with sufficiently low internal energy to allow detection. The extension of the collision cascade to larger distances from the primary ion impact point results in more material being sputtered. Further cooling of the ion population might be inferred by (MALDI like-) matrix-analyte entrainment. The observed reduction in fragmentation of the BPY precursor ions in ME-SIMS was insufficient to explain the full ion yield enhancement. Effects like surface-concentration might play a role as well.

With a view towards applications on biological tissue a first study on the combination of the molecular scanner protein identification methodology and microscope mode imaging MS is performed in **Chapter 7**. Awe3D and Spatial Image Composer software tools are used to analyze the spectral data obtained and to generate microscope and microprobe mode ion images. This first study is limited to samples of protein mixtures separated on a 1-dimensional gel. It is found that the application of a 5 nm gold layer to the sample is crucial for the recording of mass spectra and high quality ion images. The molecular scanner approach facilitates the detection and identification of high mass proteins, like  $\beta$ -galactosidase (116 kDa) on the mass microscope. The sensitivity of the combined approach is estimated to be better than 80 fmol. This value might be improved by optimization of the capture membrane.



# Samenvatting

We kunnen de term dynamisch, moleculair landschap gebruiken als metafoor voor de complexe moleculaire organisatie op het niveau van een enkele cel. Dit landschap wordt gevormd door een uitgebreide collectie van biomoleculen, zoals: DNA, RNA, fosfolipiden, koolhydraten en eiwitten. De precieze samenstelling van dit landschap is een weergave van de processen die zich er in afspelen. Eiwitten vormen een belangrijke deelgroep onder de biomoleculen, ze zijn de werkpaarden op cellulair niveau. Om meer inzicht in het functioneren van de vele biologische processen te verkrijgen is het van belang de identiteit, hoeveelheid, structuur, functie, ruimtelijke verdeling en mogelijke modificaties van deze eiwit moleculen in kaart te brengen. Nu massaspectrometrie zich heeft bewezen als zijnde *de* techniek voor de analyse van eiwitten, wacht ons een nieuwe uitdaging: de ontwikkeling van plaatsopgeloste massaspectrometrie (massamicroscopie) voor directe toepassing biologisch weefsel en cellen met een resolutie in de orde van de afmetingen van een enkele cel of beter (**Hoofdstuk 1**).

Op dit moment ziet hoge resolutie macromoleculaire massamicroscopie zich gesteld voor een aantal uitdagingen, hiertoe behoren de realisatie van:

- ruimtelijk oplossend vermogen op cellulair niveau
- snelle experimentele methodieken
- eiwit identificatie aan de hand van de gedetecteerde  $m/z$  - signalen
- geoptimaliseerde sample preparatie

Het onderzoek dat in dit proefschrift beschreven wordt, draagt bij aan de ontwikkeling van massamicroscopie tot een volwaardige experimentele techniek voor toepassing binnen de levenswetenschappen. We beschrijven de ontwikkeling en implementatie van anastigmatische ionenmicroscopie met MALDI als ionisatietechniek. Deze nieuwe benadering van macromoleculaire massamicroscopie resulteert in een significante verbetering in zowel de ruimtelijke resolutie als de duur van de experimenten. Daarnaast zorgt deze aanpak ervoor dat het spectrum aan ionisatietechnieken voor hoge resolutie plaatsopgeloste massaspectrometrie wordt uitgebreid. Om de identificatiemogelijkheden te verbeteren en de techniek geschikt te maken voor de detectie van eiwitten van hoge massa hebben we een studie verricht naar de mogelijkheden van de combinatie van anastigmatische ionenmicroscopie en de moleculaire scanner methode. Met hoge resolutie SIMS is sample preparatie voor matrix-geassisteerde massamicroscopie bestudeerd op microscopisch niveau.

In **Hoofdstuk 2** wordt een overzicht gegeven van de huidige stand van zaken in het veld van de plaatsopgeloste massaspectrometrie, met de nadruk op de veelvuldig gebruikte

## *Samenvatting*

ionisatietechnieken: SIMS en MALDI. Hier beschrijven we een aantal fundamentele en praktische aspecten van de beide technieken. Daarnaast bediscussieren we hun sterke en zwakke kanten in relatie tot massamicroscopie.

MALDI is een macromoleculaire ionisatietechniek, waarmee intacte ionen kunnen worden geproduceerd van grote, zware organische moleculen, zoals eiwitten. Het ruimtelijk oplossend vermogen dat in een standaard plaatsopgelost, microprobe MALDI massaspectrometrisch experiment wordt bereikt (25 – 100  $\mu\text{m}$ ) vraagt om verbetering. Deze beperkte resolutie kan voor een belangrijk deel worden toegeschreven aan de gebruikte methode. De maximale ruimtelijke resolutie in een microprobe experiment is gelijk aan de afmetingen van de gebruikte microprobe waarmee het oppervlak wordt bemonsterd. In geval van MALDI is dit het laser focus. Daarnaast zijn er aanwijzingen dat de gevoeligheid voor de detectie van hoge massa eiwitmoleculen sterk afneemt bij gebruik van een klein laser focus ( $< 10 \mu\text{m}$ ). Het principe van microprobe MALDI waarbij een sample serieel met een kleine microprobe wordt bemonsterd maakt deze experimenten bovendien tijdrovend. De bereiding van het sample; i.e. de inbedding van de eiwitten in de matrix kristallen, is een cruciaal onderdeel van een plaatsopgelost MALDI experiment. Hierbij zijn gevoeligheid en oplossend vermogen concurrerende factoren. Een hoge gevoeligheid wordt bereikt door voldoende extractie van eiwit moleculen uit het sample naar de matrix oplossing. De hiervoor geschikte ‘natte’ sample preparatie leidt tot diffusie van de aanwezige biomoleculen en de vorming van grote matrix kristallen, en aldus tot een beperking van de haalbare ruimtelijke resolutie.

SIMS is een andere veel gebruikte ionisatietechniek in de plaatsopgeloste massaspectrometrie. Ze werd ontwikkeld in de jaren 60 van de vorige eeuw. Het massabereik van SIMS is veel beperkter dan van MALDI. Het energetische sputterproces induceert uitgebreide fragmentatie van kwetsbare organische moleculen. Over het algemeen kunnen alleen elementen en kleine organische fragmenten met voldoende intensiteit worden gedetecteerd. Daar staat tegenover dat met SIMS een zeer hoog oplossend vermogen kan worden bereikt, tot in de orde van 100 nanometer bij gebruik van  $\text{Ga}^+$  primaire ionen. Recentelijk zijn meerdere initiatieven ontplooid gericht op de verbetering van de opbrengst van intacte moleculaire ionen in SIMS. Een voorbeeld van een succesvolle aanpak is ME-SIMS, dat gebruik maakt van een MALDI matrix om ionisatie te bevorderen en fragmentatie te verminderen.

We eindigen hoofdstuk 2 met de introductie van anastigmatische massamicroscopie of microscoop modus plaatsopgeloste massaspectrometrie en een uitgebreide beschrijving van de experimentele configuraties, die voor het beschreven onderzoek zijn gebruikt.

In **Hoofdstuk 3** worden de eerste macromoleculaire ionen beelden, verkregen d.m.v. anastigmatische ionenmicroscopie, gepresenteerd. Met behulp van anastigmatische ionenoptiek worden vergrote ionenoptische afbeeldingen van de verdelingen van moleculen in het sample gevormd op een 2-dimensionale detector aan het eind van een vluchttijd massaspectrometer en opgenomen met een CCD-camera. Zo wordt een in de tijd (of op  $m/z$  - waarde) gescheiden serie van ionen beelden verkregen waarvan de laterale resolutie vele malen beter is dan de diameter van het gebruikte laser focus. Hiermee verschilt deze methode wezenlijk van de eerdergenoemde microprobe methode, waarbij de ioniserende bundel over het oppervlak

wordt gescand (of vice versa). De best mogelijke ruimtelijke resolutie wordt hierdoor niet langer bepaald door de omvang van het focus van de laser, maar met name door de kwaliteit en afstelling van de ionenoptiek en het desorptie proces zelf. We hebben de mogelijkheden van de massamicroscopie geëvalueerd aan de hand van een MALDI test sample met een 25  $\mu\text{m}$  raster structuur. Door met een enkele puls van een  $\text{N}_2$ -laser een oppervlak van ongeveer 200  $\mu\text{m}$  in diameter te belichten werden binnen 1 milliseconde ionenbeelden van substance P en insuline opgenomen worden. De repetitie frequentie van het experiment is hoofdzakelijk begrensd door de gebruikte laser en was tijdens deze experimenten 12 Hz. De ionenoptiek kan afgesteld worden voor twee verschillende ionenoptische vergrotingen, namelijk 100- en 200-maal. In beide modi is de ruimtelijke resolutie bepaald op 4  $\mu\text{m}$ . De mogelijkheid om grotere oppervlakken gelijktijdig af te beelden maakt de microscoop modus beduidend sneller dan de microprobe modus, tot wel een factor van 2500 voor hoge resolutie experimenten.

Het principe van het afbeelden van grotere oppervlakken in microscoop modus hebben we gedemonstreerd op een raster met microscopische structuur en een diameter van 2.5 mm. Individuele, gedeeltelijk overlappende ionen beelden zijn hierbij aan elkaar geplakt d.m.v. voor dit doel ontwikkelde software, waarbij de hoge plaatsresolutie van de individuele ionen beelden behouden bleef.

In de microscoop modus is een sterk gefocuseerde ionen- of laserbundel niet langer een vereiste voor hoge ruimtelijke resolutie. Dit maakt dat ook ionisatietechnieken waarbij de mogelijkheid tot sterke focussing ontbreekt, zoals bij IR-MALDI en ionisatie d.m.v. massieve clusters, in aanmerking komen voor toepassing in plaatsopgeloste massaspectrometrie. Hiermee biedt massamicroscopie in microscoop modus een grotere flexibiliteit in de keuze van ionisatietechniek. Dit wordt gedemonstreerd in **Hoofdstuk 4**. Met een enkele puls van een 2.94  $\mu\text{m}$  infrarood laser zijn ionen beelden van een bradykinine sample verkregen. De behaalde ruimtelijke resolutie correspondeert met die van de UV-MALDI experimenten (4  $\mu\text{m}$ ). Het kleinst mogelijke, door licht diffractie begrensde laser focus, dat met de gebruikte opstelling behaald kan worden is 28  $\mu\text{m}$ . In een microprobe experiment zou dit corresponderen met de best haalbare resolutie.

In **Hoofdstuk 5** onderzoeken we het effect dat de toevoeging van matrix heeft op de informatie die verkregen wordt in plaatsopgeloste massaspectrometrie. In het bijzonder gebruiken we (ME-)SIMS voor de bestudering van zogenaamde 'dried-droplet' matrix-fosfolipiden samples. Het was mogelijk om met ME-SIMS massaspectra van de fosfolipiden monsters te bepalen, waarbij sterke signalen van intacte pseudo-moleculaire ionen werden waargenomen. Deze pseudo-moleculaire ionen worden verkregen door de additie van een proton of een natrium ion. De spectra vertonen grote gelijkens met MALDI-spectra van fosfolipiden. In vergelijking tot SIMS analyses van fosfolipiden samples, zorgt de toevoeging van 2,5-DHB als matrix voor een vermindering van het aantal waargenomen fragment ionen ten opzichte van het aantal intacte ionen. De hoge plaats resolutie van SIMS geeft inzicht in de heterogene samenstelling van het sample op microscopische schaal. De lokale variatie in de samenstelling van het sample is niet alleen van invloed op de aard van de waargenomen ionen, maar beïnvloedt bovendien de mate van fragment vorming. Deze effecten kunnen de

## *Samenvatting*

uitkomsten van een hoge resolutie, massamicroscopisch experiment beïnvloeden. Electrospray matrix depositie resulteert in veel homogenere samples, en is om die reden te prefereren voor gebruik in combinatie met hoge resolutie plaatopgeloste massaspectrometrie.

De toename van de opbrengst van intacte moleculaire ionen in ME-SIMS wordt toegeschreven aan een aantal factoren, waaronder: een efficiëntere ionisatie door proton overdracht, isolatie van lange moleculaire ketens en reductie van de interne energie van de gesputterde ionen. In **Hoofdstuk 6** gebruiken we 4 benzyl-gesubstitueerde benzylpyridinium (BPY) zouten met verschillende substituties om in het bijzonder dit laatste effect te kunnen bestuderen. Bij voldoende interne energie vervallen de benzylpyridinium ionen volgens een eenvoudige unimoleculaire reactie. De activeringsenergie voor deze reactie hangt af van de identiteit van de gesubstitueerde zijgroep. Voor alle BPY-zouten werd een toename in de opbrengst van het intacte moederion waargenomen in ME-SIMS in vergelijking tot SIMS. We hebben het verval van de BPY-moederionen op meerdere momenten gedurende de vluchttijd van ionen gemeten. We hebben kinetische energieverdelingen bepaald en vervolgens gebruikt om verschillen tussen het SIMS en ME-SIMS sputterproces te bestuderen en reactieconstanten voor de verval reactie te bepalen. De reactieconstanten en mate van fragment vorming duiden op een verlaging van de interne energie van de moeder ionen in ME-SIMS in vergelijking tot SIMS. In het kader van het 'precursor model' kunnen de resultaten als volgt worden uitgelegd: in ME-SIMS exciteert de SIMS botsingscascade een groter volume van het sample. Hierdoor zal een relatief groter gedeelte van de gevormde moederionen voldoende lage interne energie hebben om gedetecteerd te kunnen worden. Bovendien leidt het ertoe dat er meer materiaal gesputterd wordt. Verdere verlaging van de interne energie kan teweeg worden gebracht door associatie van de moederionen met matrix moleculen tijdens het sputterproces. Het totale effect van de gereduceerde fragmentatie van de BPY-moederionen in ME-SIMS kan niet de volledige toename van de opbrengst verklaren. Zeer waarschijnlijk spelen effecten als concentratie van de BPY zouten aan het oppervlak van het sample ook mee.

Met het oog op toepassing op biologisch weefsel bevat **Hoofdstuk 7** een eerste studie naar de combinatie van anastigmatische massamicroscopie met de moleculaire scanner techniek voor eiwit identificatie. Hierbij gebruiken we de Awe3D en Spatial Image Composer software voor de analyse en representatie van de spectrale en plaatsopgeloste data. Deze eerste studie beperkt zich tot samples van eiwit mengsels, die gescheiden zijn op een 1-dimensionale gel. De samples zijn zowel in microscoop als microprobe modus geanalyseerd. Om massaspectra en anastigmatische ionen beelden te kunnen opnemen blijkt het nodig om een goud laag van 5 nanometer dikte op het sample aan te brengen. Op deze manier maakt de moleculaire scanner techniek het mogelijk om hoge massa eiwit moleculen, zoals  $\beta$ -galactosidase (116 kDa), te identificeren m.b.v. de massamicroscoop. De gevoeligheid van de gecombineerde methode is bepaald op minimaal 80 fmol voor het eiwit BSA. Wellicht kan hier verbetering in worden gebracht door optimalisatie van de gebruikte invangmembranen.

# Nawoord

Dit proefschrift is tot stand gekomen met de steun en medewerking van een groot aantal mensen die het verdienen om op deze laatste -en waarschijnlijk meest gelezen- pagina's eens flink in de 'spotlights' te worden gezet.

Als eerste wil ik mijn promotor Ron Heeren bedanken. Jouw groot enthousiasme en nimmer aflatende stroom aan nieuwe ideeën hebben ertoe bijgedragen dat ik kan terugkijken op een productieve, dynamische promotieperiode. Ik heb het altijd erg gewaardeerd dat ik zo bij je binnen kon lopen en jij tijd wilde vrijmaken. Lukte dit niet dan werd je gewoon uitgenodigd aan de eettafel in Weesp. Verder wil ik je bedanken voor de vrijheid die je me hebt geboden om zelf de accenten van mijn onderzoek te bepalen.

Two guys that deserve a special mention are Liam McDonnell and Todd Mize. Your arrival in the group in my second year has been very important. Especially, in the period preceding the recording of the first microscope mode images the both of you have been of great help. Todd of the many things I could thank you for, I would like to mention your successful ideas for the MALDI test samples. Liam, you possess the ability to always ask the right questions, combined with your unfailing knowledge of literature and the fact that we have been sharing an office for almost four years, your presence has made a large impact on my research.

In mijn onderzoek zijn de technisch ondersteunende afdelingen van het AMOLF onmisbaar geweest. Dirk-Jan Spaanderman en Iliya Cerjak, jullie hebben met prachtige ontwerpen bijgedragen aan het slagen van mijn onderzoek. Ik heb er altijd veel plezier in gehad om met jullie ideeën voor nieuwe onderdelen voor de opstelling te bespreken, niet in de laatste plaats omdat jullie vaak met handige, extra functionaliteiten in het ontwerp kwamen. De mannen van de fijnmechanische werkplaats (Wim, Jan, Menno, Wim en Henk) wil ik bedanken voor het vervaardigen van menig kunststukje. Ook voor de o-zo belangrijke haastklussen kon ik bij jullie terecht. Ook bij E & I loopt een groot aantal mensen rond aan wie ik veel te danken heb. Idsart Attema en Ton Vijftigschild, aan jullie kon ik het uitzoeken van exotische hoogspanningsschema's met een gerust hart overlaten. Duncan Verheijde, bij jou kon ik terecht voor advies over data acquisitie systemen. Ivo Klinkert en Marco Konijnenburg, met de door jullie ontwikkelde software tools werden die enorme hoeveelheden data die we produceerden hanteerbaar en heb ik mijn proefschrift kunnen vullen met mooie plaatjes.

Wie hier zeker niet mag ontbreken is Frans Giskes. Frans, ik wil je bedanken voor het wegwijs maken op AMOLF, je hulp en aanwijzingen bij het sleutelen aan de TRIFT en andere

## *Nawoord*

‘opstellingen’ en de ontelbare grote en kleinere klussen waarmee je mijn onderzoek mogelijk hebt gemaakt.

The people at ULVAC-PHI I would like to thank for sharing their information on the TRIFT system with us. I especially would like to mention Jürgen Behr and Scott Bryan.

During the last stages of my project I have been involved in a collaboration with the Biomedical Proteomics Research Group Geneva. Many thanks to Ali Vaezzadeh, you have prepared many samples for me, which have resulted in the completion of chapter 7.

Wat AMOLF tot zo'n geweldige werkplek maakt zijn niet alleen de voorzieningen en aanwezige kennis en kunde. Er werken ook gewoon een heleboel erg leuke mensen! Met jullie heb ik een mooie tijd gehad zowel binnen de muren van AMOLF als erbuiten. Dus wil ik iedereen bedanken die hieraan heeft bijgedragen door inhoudelijke en inhoudsloze discussies, borrels, uitjes, het-achter-mijn-computer-vandaan-sleuren-voor-een-theepauze, etc.... Dit geldt in het bijzonder voor mijn collega's uit de massaspectrometrie groepen: Maarten, Rimco, Katrien, Yuri, Sander P., Ron, Frans, Marc, Gert, Oscar, Jorrit, Erika, Andreas, Ester, Ioana, Romulus, Liam, Anne, Lenneart, Frank, Todd, Xinghua, Sander K., Piet, Georgiana, Jaap v/d W., Beatrice, Annelies, Jaap B., Jerre, Lidwien, Bas, Nicole, Olga, Nicolas en Başak.

Mijn familie, vrienden en vooral mijn ouders wil ik heel erg bedanken voor jullie steun en interesse in de afgelopen jaren; ondanks dat de materie niet altijd tot de verbeelding moet hebben gesproken, waren jullie altijd geïnteresseerd in mijn werk.

Tot slot: Marieke, jij bent er *altijd* voor mij, je hebt me zelfs door deze lange, laatste nacht geloodst.

Stefan Luxembourg, 7 november 2005

## Curriculum Vitae

Stefan Luxembourg was born of the 5<sup>th</sup> of March in 1976 in Leidschendam, The Netherlands. He received his pre-university degree at the 'scholengemeenschap Veurs College' in this same town in 1994. He went on to study physics at the Free University (VU) of Amsterdam. In 1999 he completed his education with an undergraduate research project on the structure and functioning of photosynthetic antenna complexes in the biophysics group of Prof. R van Grondelle at the VU. In 2000 he joined the atmospheric chemistry group of Prof. J. Lelieveld at the Institute for marine and atmospheric research (IMAU) at Utrecht University. Here, under supervision of dr. J. de Gouw he worked on the development of a proton-transfer reaction ion trap mass spectrometer for on-line analysis of trace gasses in the atmosphere. In 2001 he started his PhD-research project on mass microscopy at the FOM Institute for atomic and molecular physics (AMOLF). This thesis contains the most important results from this four-and-a-half year period.

**This thesis is based on the following publications:**

S. L. Luxembourg, T. H. Mize, L. A. McDonnell and R. M. A. Heeren, *Rapid, high-spatial resolution mass spectrometric imaging of peptide and protein distributions on a surface* Analytical Chemistry, **76**, 5339 – 5344, (2004) (**Chapter 3**)

S. L. Luxembourg, L. A. McDonnell, T. H. Mize and R. M. A. Heeren, *Infrared mass spectrometric imaging below the diffraction limit*, Journal of Proteome Research, **4**, 671 – 673, (2005) (**Chapter 4**)

S. L. Luxembourg, L. A. McDonnell, M. Duursma, X. Guo and R. M. A. Heeren, *Effect of Local Matrix Crystal Variations in Matrix-Assisted Ionization Techniques for Mass Spectrometry*, Analytical Chemistry, **75**, 2333 – 2341, (2003) (**Chapter 5**)

S. L. Luxembourg and R. M. A. Heeren, *Fragmentation at and above surfaces in SIMS: effects of biomolecular yield enhancing surface modifications*, International Journal of Mass Spectrometry, submitted (**Chapter 6**)

**Other publications:**

R. M. A. Heeren, L. A. McDonnell, E. Amstalden, S. L. Luxembourg, A. F. M. Altelaar and S. R. Piersma, *Why don't biologists use SIMS?*, Applied Surface Science, accepted for publication

L. A. McDonnell, S. R. Piersma, A. F. M. Altelaar, T. H. Mize, S. L. Luxembourg, P. D. E. M. Verhaert, J. van Minnen and R. M. A. Heeren, *Subcellular imaging mass spectrometry of brain tissue* Journal of Mass Spectrometry, **40**, 160 – 168, (2005)

L. A. McDonnell, T. H. Mize, S. L. Luxembourg, S. Koster, G. B. Eijkel, E. Verpoorte, N. F. de Rooij, R. M. A. Heeren, *Using matrix peaks to map topography: Increased mass resolution and enhanced sensitivity in chemical imaging*, Analytical Chemistry, **75**, 4373-4381, (2003)

C. Warneke, S. L. Luxembourg, J. A. de Gouw, H. J. I. Rinne, A. B. Guenther and R. Fall, *Disjunct eddy covariance measurements of oxygenated volatile organic compounds fluxes from an alfalfa field before and after cutting*, Journal of Geophysical Research-Atmospheres, **107**, 4067, (2002)

H. J. I. Rinne, A. B. Guenther, C. Warneke, J. A. de Gouw and S. L. Luxembourg, *Disjunct eddy covariance technique for trace gas flux measurements*, Geophysical Research Letters, **28**, 3139-3142, (2001)

C. Warneke, C. van der Veen, S. L. Luxembourg, J. A. de Gouw and A. Kok, *Measurements of benzene and toluene in ambient air using proton-transfer-reaction mass spectrometry: calibration, humidity dependence, and field intercomparison*, International Journal of Mass Spectrometry, **207**, 167-182, (2001)